



DISSERTATION

Titel der Dissertation

Hyperfine Structure Measurements of Antiprotonic ${}^3\text{He}$
using Microwave Spectroscopy

Verfasserin

Mag. rer. nat. Susanne Friedreich

angestrebter akademischer Grad

Doktorin der Naturwissenschaften (Dr. rer. nat.)

Wien, 2012

Studienkennzahl lt. Studienblatt: A 091 411
Dissertationsgebiet lt. Studienblatt: Physik
Betreuerin / Betreuer: Hon.-Prof. Dipl.-Phys. Dr. Eberhard Widmann

”Never, never, never, never give up!” – Winston Churchill

Abstract

The goal of this project was to measure the hyperfine structure of $\bar{p}^3\text{He}^+$ using the technique of laser-microwave-laser spectroscopy. Antiprotonic helium ($\bar{p}\text{He}^+$) is a neutral exotic atom, consisting of a helium nucleus, an electron and an antiproton. The interactions of the angular momenta of its constituents cause a hyperfine splitting (HFS) within the energy states of this new atom. The 3% of formed antiprotonic helium atoms which remain in a metastable, radiative decay-dominated state have a lifetime of about 1-3 μs . This time window is used to do spectroscopic studies. The hyperfine structure of $\bar{p}^4\text{He}^+$ was already extensively investigated before. From these measurements the spin magnetic moment of the antiproton can be determined. A comparison of the result to the proton magnetic moment provides a test of CPT invariance. Due to its higher complexity the new exotic three-body system of $\bar{p}^3\text{He}^+$ is a cross-check for the measurements with $\bar{p}^4\text{He}^+$ and a more stringent test of theoretical calculations and methods. The measurement principle is based on inducing a population asymmetry by laser-depopulation of one of two HF states. Subsequently, a microwave pulse stimulates population transfer between these substates, followed by a second laser pulse to measure the transferred population. For the microwave spectroscopy several cryogenic cavities were designed, built and tested. One major part of my work consisted of calculations and finite-element simulations as well as detailed preparation studies, diagnostics and calibration of these high frequency structures and the complete microwave apparatus. The main focus of my thesis was on the execution of the measurements at CERN (as well as the organization or the supervision of project students) and the related data analysis, including numerical simulations of the hyperfine transition processes. Two out of four measurable transition lines of the $(n, L) = (36, 34)$ state of $\bar{p}^3\text{He}^+$ were observed for the first time and in good agreement with theoretical QED calculations. The final results for

the two measured transition frequencies are $\nu_{\text{HF}}^{--} = 11.12548(08)$ GHz and $\nu_{\text{HF}}^{-+} = 11.15793(13)$ GHz.

Zusammenfassung

Zielsetzung dieses Projekts war die Messung der Hyperfeinstruktur von $\bar{p}^3\text{He}^+$ mittels Laser-Mikrowellen-Laser Spektroskopie. Antiprotonisches Helium ($\bar{p}\text{He}^+$) ist ein neutrales, exotisches Atom, bestehend aus einem Heliumkern, einem Elektron und einem Antiproton. Die Wechselwirkungen der einzelnen Drehmomente erzeugen eine Hyperfeinaufspaltung (HFS) innerhalb der Energiezustände. Die 3% der gebildeten Atome antiprotonischen Heliums, die in einem metastabilen, durch Strahlung zerfallenden Zustand verbleiben, haben eine Lebensdauer von 1-3 μs . Das dadurch definierte Zeitfenster wird genutzt, um mikrowellen-spektroskopische Messungen durchzuführen. Die Hyperfeinstruktur von $\bar{p}^4\text{He}^+$ wurde bereits vollständig untersucht. Mit diesen Messungen kann man das magnetische Moment des Antiprotons bestimmen. Der Vergleich des magnetischen Moments für Proton und Antiproton gibt Aufschluss über eine mögliche CPT-Verletzung. Die komplexere Struktur von $\bar{p}^3\text{He}^+$ ermöglicht eine Gegenprüfung der Ergebnisse mit $\bar{p}^4\text{He}^+$ sowie einen restriktiveren Test der theoretischen Berechnungen und Methoden. Das Prinzip der Messung basiert darauf eine Laser-induzierte Asymmetrie zwischen den der HF Zustände zu erzeugen. Danach wird mit Hilfe von Mikrowellenstrahlung ein Besetzungsübergang zwischen diesen Zuständen stimuliert und darauffolgend ein weiterer gesendet, um die erfolgte Besetzungsänderung zu messen. Für die wurden mehrere kryogenische Kavitäten simuliert, gebaut und getestet. Ein wesentlicher Teil meiner Arbeit bestand darin Berechnungen und finite-element Simulationen dazu durchzuführen ebenso wie umfangreiche Tests, Diagnostik und Kalibrierung dieser Hochfrequenzstrukturen und des gesamten Mikrowellen-Aufbaus. Der Fokus meines Projekts war die Umsetzung der spektroskopischen Messungen am CERN (ebenso wie die Organisation oder auch die Betreuung von Projektstudenten) und die anschliessende Datenanalyse sowie numerische Simulationen der Übergänge zwischen den Hyperfeinzuständen. Zwei der

vier messbaren Linien des $(n, L) = (36, 34)$ Zustands in $\bar{p}^3\text{He}^+$ konnten zum ersten Mal beobachtet werden und stimmen gut mit den QED Berechnungen überein. Die gemessenen Werte für diese beiden Übergangsfrequenzen sind $\nu_{\text{HF}}^{--} = 11.12548(08)$ GHz und $\nu_{\text{HF}}^{-+} = 11.15793(13)$ GHz.

Contents

Abstract	iii
Zusammenfassung	v
1 Antimatter – A Motivation	1
2 Antiprotonic Helium & Hyperfine Structure	5
2.1 Exotic Atoms - Where It All Started	5
2.2 Antiprotonic Helium – A Metastable Three-Body System	6
2.3 Hyperfine Structure	8
3 The Experiment	15
3.1 Laser-Microwave-Laser Spectroscopy	15
3.2 Other Systematic Investigations	20
4 Experimental Setup	25
4.1 Antiproton Decelerator (AD)	25
4.2 Cryogenic System	26
4.3 Gas System	31
4.4 Laser Spectroscopy Setup	31
4.5 Detector Setup & Experiment Control	33
5 The Microwave Spectroscopy Apparatus	37
5.1 Microwave Cavities	37
5.1.1 How to Design a Microwave Cavity	37
5.2 Simulations of the Microwave Cavities	41
5.2.1 Simulation Studies	44
5.3 Building the Cavity	46

5.3.1	Pin Antenna, Iris & Waveguides – Coupling to and from the Cavity	51
5.4	Testing the Cavity Characteristics	52
5.4.1	Perturbation Measurements	52
5.5	Starting Point - The Old Measurement Setup	63
5.5.1	Diagnostic Mode	63
5.5.2	Operational Mode	66
5.6	The New Measurement Setup	67
5.7	Calibration	70
5.7.1	Power Calibration of the Cavities	70
6	Numerical Simulations of Transition Processes	75
6.1	Two-Level Optical Bloch Equations	75
6.2	The Laser Pulse	76
6.3	Electric Dipole Moment & Rabi Oscillations	77
6.4	Laser Transitions	78
6.4.1	Doppler Broadening	79
6.4.2	Refilling from Higher Lying States	80
6.5	Magnetic Dipole Moment & Rabi Oscillations	83
6.6	Microwave Transitions	84
6.7	Collisional Effects	91
7	Data Analysis	93
7.1	Pre-Analysis (Online)	93
7.2	Extensive Analysis (Offline)	96
7.2.1	Laser Scans	97
7.2.2	Laser Depletion Efficiency & Laser Delay Timing . . .	98
7.2.3	Microwave Scans	99
8	Experimental Results	101
8.1	Laser Resonance Scans	101
8.2	Laser Delay Study	106
8.3	Microwave Power Study	107
8.4	Microwave Resonance Scans	108
9	Conclusion	117

A The Smith Chart	123
A.0.1 Stub-Tuner	125
A.0.2 Multiple-Stub-Tuner	125
A.0.3 Quality Factor	126
B Technical Drawings	129
C HFSS Simulations	131
D Results of Numerical Calculations	139
E Microwave Resonance Profiles	143

Chapter 1

Antimatter – A Motivation

In 1928 the physicist P. Dirac found a way to combine quantum physics with the theory of special relativity [1]. This fundamental relativistic wave equation – in this case for the electron – which integrated both theories, appeared to work not only for electrons with negative charge. It was equally valid for an electron with positive charge, the *positron*, that was later proved to be the *antiparticle* of the electron. The experimental proof of the positron and thus of the existence of antimatter was given by C.D. Anderson in 1932 [2]. Only more than twenty years later the antiproton was discovered by O. Chamberlain et al. [3] in Berkeley in 1955. The antiproton is the antimatter counterpart of the proton with a mass $m_{\bar{p}} = m_p$ and a charge $q_{\bar{p}} = -q_p$, i.e. with negative charge. O. Chamberlain and E. Segrè received the Nobel Prize for their achievement in 1959. The antineutron was identified soon after by studying the charge exchange reaction where a neutron and an antineutron result from the interaction of proton and antiproton [4].

So far the most complete theory to explain fundamental interactions and particles is the *Standard Model of Particle Physics*. It was developed in the early 1970s and comprises three of the four fundamental forces, the weak force, the strong force and the electromagnetic interaction. The gravitational force could not yet be successfully integrated in this framework. The electromagnetic and the weak force were combined to one single gauge theory and their coupling constants correlated within this theory. *Quantum chromodynamics* (QCD) – i.e. the strong force – and the *electroweak* theory were then unified to form the Standard Model with their coupling constants being independent from each other.

One fundamental principle of the Standard Model and other mainstream

quantum field theories is the CPT theorem. It predicts that the laws of physics are symmetric under the combined conjugation transformations of charge C, parity P and time T. A charge transformation C changes a particle to its antiparticle, while space coordinates, time and spin remain unchanged. The sign for all (additive) quantum numbers, the electric charge, lepton flavor and baryon number is inverted. The parity operator P inverts all three spatial coordinate axes and consequently also the momenta while time, angular momenta and spins as well as charge are not affected. The time reversal operator T corresponds to a process exactly reversed in time while the spatial coordinates are left unchanged. Each one of these transitions will bring the system back to its original state by applying it twice. One of the most important implications of this theorem is the identity of the absolute values of all parameters, like mass, electric charge or magnetic moment for a particle and the respective antiparticle.

During the late 1950s an experiment on the beta decay of cobalt-60 [5] revealed the violation of the P symmetry. For ten years physicists assumed that the combined CP symmetry would be generally valid in physical phenomena. Christenson et al. discovered a CP-violation in the decay of the K^0 meson [6]. The Standard Model implies that CPT symmetry must be conserved in all physical interactions, i.e. C, P and T at the same time. It further includes that Lorentz invariance is correct and preserved. A Lorentz invariant quantum field theory with a hermitian Hamiltonian requires that CPT symmetry is conserved. The CPT theorem is a mathematical consequence of the characteristics of quantum field theories such as Lorentz invariance. Therefore, a violation of charge and parity would require a T-violation as well. The observation of a CPT violation could point to new physics beyond the current theories of the Standard Model.

The observed violations of C and CP were all related to weak interactions. However, electromagnetic and strong force are very dominant in comparison and thus hinder a highly precise measurement of weak interactions. It implies that a particle has to be identical to its antiparticle in all its properties except for the charge which has to have opposite sign. Therefore, particle-antiparticle pairs annihilate, their total mass converting to energetic photons. They can also be produced from energy which is equal to or greater than their total mass.

The initial motivation for carrying out microwave spectroscopy experi-

ments with antiprotonic helium was a highly precise measurement of the magnetic moment of the antiproton. Similar to the particle mass also these measurements of hyperfine substructure transitions of antiprotonic helium can be used to test CPT symmetry. An extensive study based on antiprotonic ${}^4\text{He}$ was carried out and completed by T. Pask in 2008 [7] leading to the currently smallest error for the magnetic moment of 0.29%.

The hyperfine structure of antiprotonic helium builds up due to the interaction of the antiproton orbital angular momentum with the electron spin – which gives the dominant splitting – and further with the antiproton spin in the case of $\bar{p}{}^4\text{He}^+$. For $\bar{p}{}^3\text{He}^+$ there is an additional splitting caused by the nuclear spin.

The present thesis project with antiprotonic ${}^3\text{He}$ aimed primarily at providing a more stringent test of the theoretical calculations due to the higher complexity of this three-body system (for details refer to Ch. 2). Based further on the available and achievable experimental conditions, a higher precision than with $\bar{p}{}^4\text{He}^+$ could not be expected. This experiment required to a large extent a completely new setup, including the gas system, the cryogenic apparatus and in particular the sensitive microwave apparatus.

The following work is structured in several major parts. The first two chapters give a general overview of the research topic. Chapters 3 and 4 provide an explanation of the measurement technique and the experimental setup. The rest of this thesis will focus on my work in this project. In chapter 5 and 6 the required preparations for the experiment in terms of simulations, construction of hardware and tests of the (microwave) setup will be explained. The remaining part will contain an overview of the data analysis methods and a detailed insight to the experimental measurements and results followed by an appropriate discussion and concluding remarks. Simulations of the experiment and the microwave apparatus as well as tests and preparations of the latter were entirely part of my own work. Further I carried out the measurements at CERN, including the organization and supervision of project students who participated mostly in the data acquisition. My contribution also included the offline analysis of the measured data. The laser system was run by members of the ASACUSA collaboration at CERN (M. Hori, A. Dax, A. Soter, K. Todoroki, T. Kobayashi). The software for the online part of the data analysis was provided by D. Barna and the cryogenic system prepared and maintained by O. Massiczek.

Some results used in this thesis as well as parts of the work regarding the development and preparation of the experimental setup have already been published [8–10]. The final achievements presented in this work are a follow-up including more measurement data.

Chapter 2

Antiprotonic Helium & Hyperfine Structure

2.1 Exotic Atoms - Where It All Started

A negatively charged particle with long enough life time that is slowed down and stopped in matter can replace an electron of the atom and get bound on an atomic orbit. The new few-body system formed this way is called *exotic atom* and usually named after the kind of particle responsible for the transformation, e.g. antiprotonic, mesonic, muonic, kaonic. Negatively charged hadrons were initially assumed to disappear by nuclear absorption processes immediately after the formation of exotic atoms. When such particle – at that time negatively charged muons or pions – enters matter it collides with atoms of the respective medium (gas or condensed matter) and loses kinetic energy through ionization. An exotic atom will be formed if the overlap between this particle and the wave functions of the electron it ejects is high enough. As a consequence this initial bound state and the state of the ejected electron are geometrically close. In addition the binding energies of the captured particle and the electron are equal and thus the newly formed atom will already be in a highly excited state with a principal quantum number $n = \sqrt{\frac{m}{m_e}}$ where m is the reduced mass of the entering particle and m_e the reduced mass of the electron. Therefore, they have to go through a long cascade process before arriving at the nucleus.

Already more than sixty years ago Fermi and Teller [11], Wightman et al. [12] and others found out that a negative particle, if captured in an atom,

at first replaces one of the valence electrons – before it gets finally captured in the atomic nucleus. In the 1960s – when the antiproton was only discovered a few years before – several experiments with helium bubble chambers were done to investigate the decays of negative pions and kaons [13–16]. It was found that Auger effect and Stark effect would destroy the exotic atoms during collisions long before the atom would deexcite radiatively [17, 18]. This was proved for pionic hydrogen [19, 20] but was expected to behave equivalently also for antiprotonic and kaonic atoms. In all materials, except for helium where a few percent of the mesons can survive several microseconds, 100% of the mesons die within a very short time. Condo [21] and Russell [22] suggested that this effect in helium could be due to the Auger/Stark effect suppression mechanism. They postulated that instead of slowly cascading most of the atoms decay within several nanoseconds and only a very small fraction follows a slow cascade – through states with lifetimes of a few microseconds – instead of annihilating immediately in the nucleus.

More than twenty years later, in 1989, an experiment with K^- mesons stopped in liquid helium [23] experimentally proved what Condo had predicted. A similar study with antiprotons at KEK¹ in Japan [24] in 1991 discovered that also antiprotons, slowed down to very low energies and stopped in helium, were able to survive for times in the order of microseconds in the surroundings of ordinary helium atoms. Since antiprotons do not decay, their trapping is not limited by their lifetime. These same effects which were discovered with kaons could also be observed with pionic helium at TRIUMF² in 1992 [25]. The discovery of the longevity of antiprotons in such *trapped states* soon turned them into a very promising object for fundamental research.

2.2 Antiprotonic Helium – A Metastable Three-Body System

What happened when the experiment at KEK could for the first time stop antiprotons in helium? If an antiproton is approaching a helium atom at its ionization energy (24.6 eV) or below, the antiproton can eject one of the two electrons from the ground state of the helium atom, replace it and thus get

¹National laboratory for high energy physics, Japan

²Canada's national laboratory for particle and nuclear physics

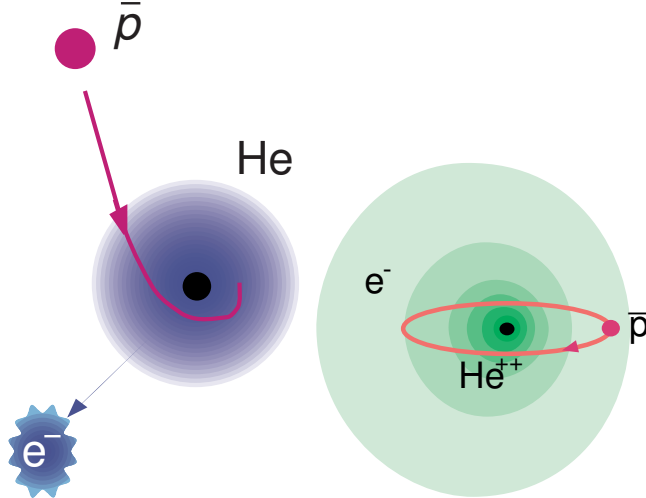


Figure 2.1: Formation of antiprotonic helium. An antiproton approaching a helium atom at its ionization energy and the resulting exotic antiprotonic helium atom [26].

captured. This exotic, metastable three-body *antiprotonic helium*, i.e. $\bar{p}\text{He}^+$, consists of one electron in the ground state, the helium nucleus and the antiproton [27–29]. Within the atom the antiproton occupies near-circular states with L close to n , where L is the angular momentum quantum number and n the principal quantum number. The electron remains in the ground state. The antiproton is, due to its high mass, most likely to be captured into states with high angular momentum, i.e. $n = n_0 \equiv \sqrt{M^*/m_e} \sim 38$, M^* being the reduced mass of the system.

In the region of principle quantum numbers $n = 32 - 40$ and vibrational quantum numbers $v = 0 - 3$ – where $v = n - L - 1$ and L is the total angular momentum – the antiproton can, to the first order, only decay radiatively – deexcite to a lower state via photon emission (v remains constant) – with lifetimes of several microseconds. For most states an Auger deexcitation, i.e. ejection of the electron, is much faster and thus more likely. About 97% of these exotic atoms find themselves in states dominated by Auger decay and ionize within a few nanoseconds. Afterwards the remaining antiprotonic helium ion undergoes Stark mixing due to the electric field of the surrounding helium atoms. The antiprotons then annihilate within picoseconds with one of the nucleons of the helium nucleus because of the overlap of their

wave functions. This is explained by the Stark mixing which brings the antiprotons into S states which have a large overlap with the nucleus.

In a narrow region around $(n, L) = (38, 37)$ the system will be in a metastable state. Only 3% of the antiprotonic helium atoms remain in this metastable, radiative decay-dominated states. In this case the change of the orbital angular momentum ΔL in the Auger transition is large and thus Auger decay is suppressed. Consequently, these states slowly deexcite radiatively to the $(n', L') = (n - 1, L - 1)$ state and are relatively long-lived, having a lifetime of about 1-3 μ s. This time window can be used to do microwave spectroscopy measurements. Figure 2.2 illustrates this cascade structure for both types of antiprotonic helium.

The Pauli exclusion principle protects this system from collisions with helium atoms since the exotic atom retains one electron. The presence of the e^- also removes the L -degeneracy of the states with the same n , therefore preventing the Stark mixing in the helium gas. The external Auger decay of the remaining electron is suppressed by the large ionization energy compared to the $n \rightarrow n - 1$ level spacing of a few eV. At the end of the cascade towards the nucleus Auger decay is no longer suppressed, the second electron is ejected in less than 10 ns. Therefore, degeneracy occurs, the Stark mixing becomes dominant due to the increased mixing amplitudes and the antiproton annihilates in the nucleus.

Since this experiment at KEK, the frequencies for transitions from long-lived to short-lived states of this exotic atom were measured with always increasing accuracy [28–33]. From these frequencies – in comparison with quantum electrodynamic (QED) calculations – the antiproton-to-electron mass ratio [34] could be assessed and its value confronted with the equivalent result for the proton which thus provided very precise tests of CPT invariance. The most accurate result to date was achieved with a laser spectroscopy technique by Hori et al. [35].

2.3 Hyperfine Structure

The interaction of the magnetic moments of the particles constituting these exotic atoms gives rise to a splitting of the energy levels. The coupling of the electron spin \vec{S}_e and the orbital angular momentum of the antiproton \vec{L} leads to the primary splitting of the state into a doublet structure, in

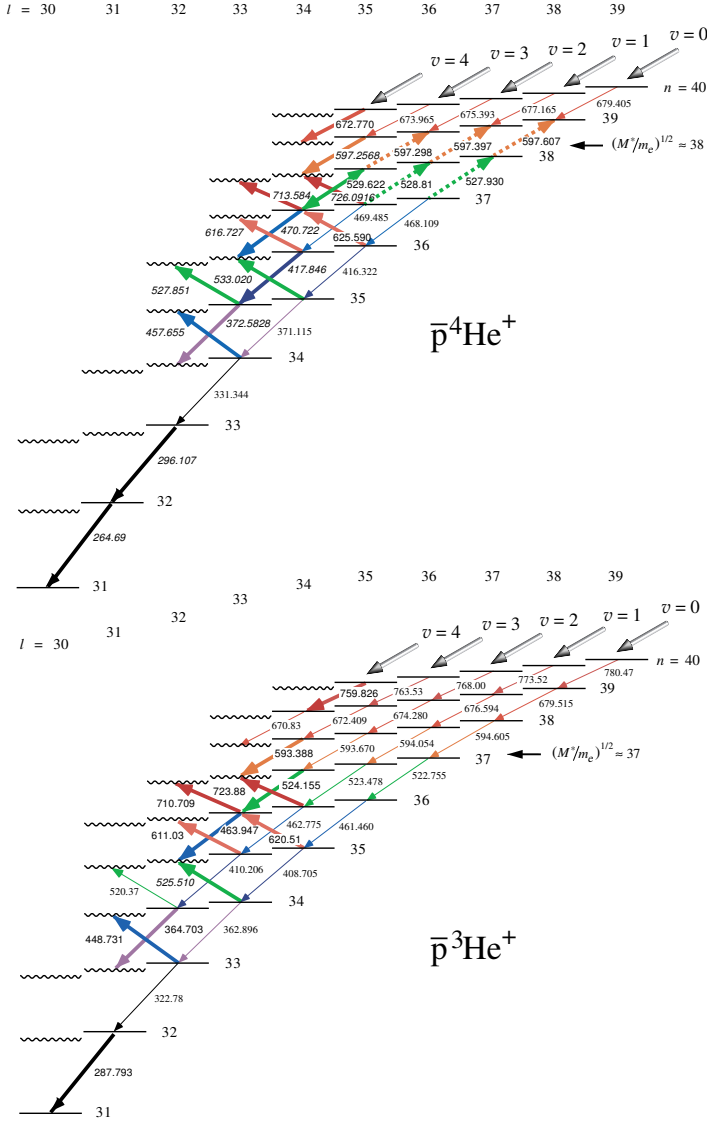


Figure 2.2: The picture displays the cascade structures of $\bar{p}^4\text{He}^+$ and $\bar{p}^3\text{He}^+$ [28]. The continuous and wavy bars stand for radiative decay dominated metastable states and Auger decay dominated short-lived states respectively. The thin arrows denote the theoretical radiative decay transitions and the bold arrows indicate the measured transitions. Arrows that point upwards indicate unfavored transitions.

the order of $\nu_{\text{HF}} = 10 - 15$ GHz. This spin-orbit splitting is referred to as *hyperfine* (HF) splitting. In atomic physics the fine structure is a spin-orbit splitting of one particle. What is here referred to as hyperfine structure is the spin-orbit splitting between two different particles. The classical fine structure of the antiproton is part of the super-hyperfine substructure in the case of antiprotonic helium (see below). The quantum number $\vec{F} = \vec{L} + \vec{S}_e$ defines the two substates as $F_+ = L + \frac{1}{2}$ and $F_- = L - \frac{1}{2}$ due to the dominant interaction of the orbital angular momentum and the electron spin. The spin-orbit interaction of the antiproton orbital angular momentum and antiproton spin $\vec{S}_{\bar{p}}$ in combination with the contact spin-spin and the tensor spin-spin interactions between the particles results in a further splitting of these HF states into quadruplets, the so-called *super-hyperfine* (SHF) splitting – with frequencies ν_{SHF} about 150-300 MHz in the case of $\bar{p}^4\text{He}^+$. This quadruplet is written as $\vec{J} = \vec{F} + \vec{S}_{\bar{p}}$. For $\bar{p}^3\text{He}^+$ the situation is slightly different. The non-zero spin of the ${}^3\text{He}$ nucleus causes at first SHF splitting which can be characterized by the quantum number $\vec{G} = \vec{F} + \vec{S}_h = \vec{L} + \vec{S}_e + \vec{S}_h$ where \vec{S}_h is the spin of the helium nucleus. This results in four SHF substates. At last, the spin-orbit interaction of the antiproton orbital angular momentum and antiproton spin $\vec{S}_{\bar{p}}$ in combination with the contact spin-spin and the tensor spin-spin interactions between the particles result in a further splitting of the SHF states into eight substates referred to as *super-super-hyperfine* (SSHF) splitting. This octuplet structure can be described by the quantum number $\vec{J} = \vec{G} + \vec{S}_{\bar{p}} = \vec{L} + \vec{S}_e + \vec{S}_h + \vec{S}_{\bar{p}}$. In antiprotonic ${}^4\text{He}$ the nucleus has no spin and thus there is only a quadruplet substructure, while for ${}^3\text{He}$ a nuclear spin exists which also couples with electron and antiproton magnetic moment. The overlap with the electron cloud is larger for the helium nucleus even though the magnetic moment is smaller than that of the antiproton. As a consequence, the helium nucleus contributes to the SHF structure while the antiproton spin causes the SSHF splitting. Figures 2.3 and 2.4 show the energy level structure for $\bar{p}^4\text{He}^+$ and $\bar{p}^3\text{He}^+$.

The hyperfine structures for $\bar{p}^3\text{He}^+$ and $\bar{p}^4\text{He}^+$ have been calculated most accurately by Korobov [36–38]. The hyperfine splittings of the energy levels in $\bar{p}^3\text{He}^+$ could be calculated to the α^3 order terms which comes due to the anomalous magnetic moment of the electron – in contrast to $\bar{p}^4\text{He}^+$ where also α^4 correction terms were taken into consideration. The finite-size electromagnetic structure and interactions are important for particles

composed of more than two constituents. If the non-relativistic QED theory is incorporated into the Breit-Pauli Hamiltonian [39] to take this into account, the spin dependent part for a system of spin- $\frac{1}{2}$ particles looks like the following:

$$\begin{aligned} H_B &= -\frac{e^2}{c^2} \sum_{j \neq i} \frac{Z_i Z_j c_S^j [\vec{r}_{ij} \times \vec{p}_j] \vec{s}_j}{2m_j^2 r_{ij}^3} \\ &- \frac{e^2}{c^2} \sum_{i,j} \frac{Z_i Z_j (c_F^i [\vec{r}_{ij} \times \vec{p}_j] \vec{s}_j)}{m_i m_j r_{ij}^3} \\ &+ \sum_{i,j} \left\{ \left[\frac{\vec{\mu}_i \vec{\mu}_j}{r_{ij}^3} - 3 \frac{(\vec{\mu}_i \vec{r}_{ij})(\vec{\mu}_j \vec{r}_{ij})}{r_{ij}^5} \right] - \frac{8\pi}{3} \vec{\mu}_i \vec{\mu}_j \delta \vec{r}_{ij} \right\}. \end{aligned}$$

Here

$$\vec{\mu}_i = \left(\frac{c_F^i Z_i}{2m_i c} \right) \vec{\sigma}_i \quad (2.1)$$

denotes an operator of the magnetic moment, the coefficients c_F and c_S are defined as

$$\begin{aligned} c_F^i &= 1 + \kappa_i \\ c_S^i &= 1 + 2\kappa_i, \end{aligned} \quad (2.2)$$

κ_i being the anomalous magnetic moment of a particle. \vec{r}_i , \vec{p}_i , \vec{s}_i , m_i , Z_i and μ_i are the position vector, momentum, spin, mass, electric charge and magnetic moment of the antiproton, helium nucleus or the electron, $\vec{r}_{ij} = \vec{r}_i - \vec{r}_j$, $\delta \vec{r}_{ij}$ is the Kronecker delta. The effective Hamiltonian can be derived from Eq. 2.1 as

$$\begin{aligned} H_{\text{eff}} &= E_1(\vec{L} \cdot \vec{s}_{e^-}) + E_2(\vec{L} \cdot \vec{s}_{\bar{p}}) + E_3(\vec{L} \cdot \vec{s}_h) + E_4(\vec{s}_{e^-} \cdot \vec{s}_{\bar{p}}) \\ &+ E_5(\vec{s}_{e^-} \cdot \vec{s}_h) + E_6(\vec{s}_{\bar{p}} \cdot \vec{s}_h) \\ &+ E_7\{2L(L+1)(\vec{s}_{e^-} \cdot \vec{s}_{\bar{p}}) - 3[(\vec{L} \cdot \vec{s}_{e^-}) + (\vec{L} \cdot \vec{s}_{\bar{p}})]\} \\ &+ E_8\{2L(L+1)(\vec{s}_{e^-} \cdot \vec{s}_h) - 3[(\vec{L} \cdot \vec{s}_{e^-}) + (\vec{L} \cdot \vec{s}_h)]\} \\ &+ E_9\{2L(L+1)(\vec{s}_{\bar{p}} \cdot \vec{s}_h) - 3[(\vec{L} \cdot \vec{s}_{\bar{p}}) + (\vec{L} \cdot \vec{s}_h)]\} \end{aligned} \quad (2.3)$$

where \vec{L} is the orbital angular momentum of the antiproton, \vec{s}_{e^-} The electron spin, \vec{s}_h the helium nucleus spin and $\vec{s}_{\bar{p}}$ the antiproton spin [37]. The coefficients E_i were obtained by numerically evaluating the operators in Eq. 2.1 and depend on the spatial degrees of freedom.

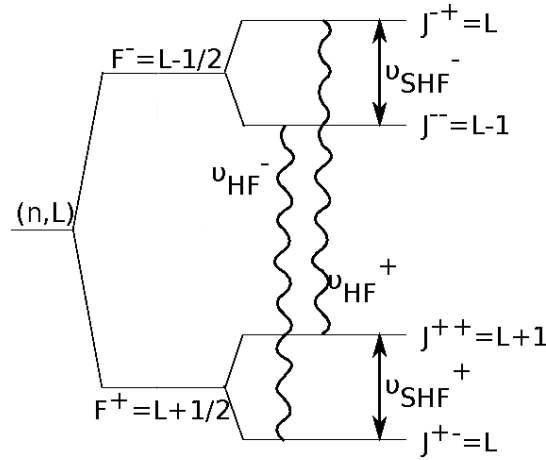


Figure 2.3: Hyperfine splitting of a state (n, L) of $\bar{p}^4\text{He}^+$. The wavy lines denote allowed M1 transitions that can be induced by microwave radiation [29].

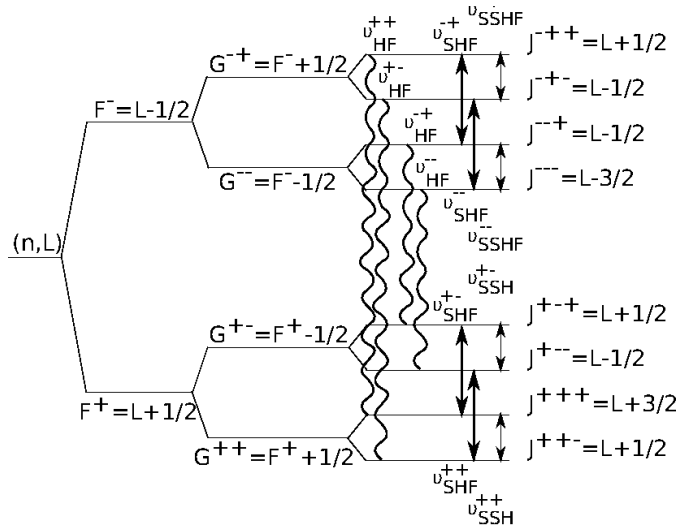


Figure 2.4: Hyperfine splitting of a state (n, L) of $\bar{p}^3\text{He}^+$. The wavy lines denote allowed M1 transitions that can be induced by microwave radiation [29].

Transitions between those SHF and SSHF states can be induced by a microwave frequency field. Only the transitions which include a single electron spin flip, referred to as *favored* transitions, can be measured due to limitations of microwave input power. The *unfavored* transitions consisting of an electron and an antiproton spin flip would require three orders of magnitude more power. The electron spin flip transitions can be induced by an oscillating magnetic field. The allowed transitions are given below. There are two for $\bar{p}^4\text{He}^+$ [37]

$$\begin{aligned}\nu_{\text{HF}}^+(37, 35) &= 12.89580 \text{ GHz} : J^{++} = F^+ + \frac{1}{2} \leftrightarrow J^{-+} = F^- + \frac{1}{2} \\ \nu_{\text{HF}}^-(37, 35) &= 12.92390 \text{ GHz} : J^{+-} = F^+ - \frac{1}{2} \leftrightarrow J^{--} = F^- - \frac{1}{2}\end{aligned}\quad (2.4)$$

and four transitions for $\bar{p}^3\text{He}^+$

$$\begin{aligned}\nu_{\text{HF}}^{++}(36, 34) &= 16.11160 \text{ GHz} : J^{+++} = L + \frac{3}{2} \leftrightarrow J^{-++} = L + \frac{1}{2} \\ \nu_{\text{HF}}^{+-}(36, 34) &= 16.14341 \text{ GHz} : J^{++-} = L + \frac{1}{2} \leftrightarrow J^{-+-} = L - \frac{1}{2} \\ \nu_{\text{HF}}^{--}(36, 34) &= 11.12500 \text{ GHz} : J^{---} = L - \frac{1}{2} \leftrightarrow J^{---} = L - \frac{3}{2} \\ \nu_{\text{HF}}^{-+}(36, 34) &= 11.15773 \text{ GHz} : J^{+-+} = L + \frac{1}{2} \leftrightarrow J^{--+} = L - \frac{1}{2}.\end{aligned}\quad (2.5)$$

The goal of this experiment is to measure the transitions between the SHF (SSHF) substates. From the measured frequency difference between two transitions it is possible to calculate the antiprotonic magnetic moment by comparison with the three-body QED calculations. The theoretical calculations have been developed by two different groups [36, 40, 41]. They used all the same Hamiltonian for their calculations but the energy eigenvalues have been obtained using different variational methods.

Chapter 3

The Experiment

3.1 Laser-Microwave-Laser Spectroscopy

The experimental technique is a three-step process, referred to as *laser-microwave-laser spectroscopy*. To accurately determine the hyperfine splitting it is necessary to induce a transition between the HF substates. Laser spectroscopy is applied to induce a transition between individual states. In principle a transition between HF states with different principal quantum number n and equal total angular momentum is also possible. To move between the HF substates a microwave resonance is required. In 2001 the first *laser-microwave-laser* (in Ch. 3) measurement was performed [42] to successfully resolve the hyperfine structure. First experiments to investigate the antiprotonic helium hyperfine structure were limited to laser resonance transitions. To measure one particular metastable state of antiprotonic helium atoms the population of the respective state needs to be transferred by a laser pulse at exactly the resonance frequency to a state which decays via the faster Auger channel. The almost immediate annihilation of this state consequently causes a peak which can be measured. Figure 3.1 illustrates the first laser spectroscopic measurement with $\bar{p}^4\text{He}^+$ and the sensitivity of the annihilation signal on the laser frequency [31].

After antiprotonic helium is formed, the atoms in the hyperfine substates are all equally populated. Therefore at first a population asymmetry between the SSHF states of the measured radiative decay state (n, L) needs to be created. This depopulation is induced by a short laser pulse, which transfers the majority of the antiprotons from one of the HF states of the radiative decay-dominated, metastable parent state to the Auger decay-dominated,

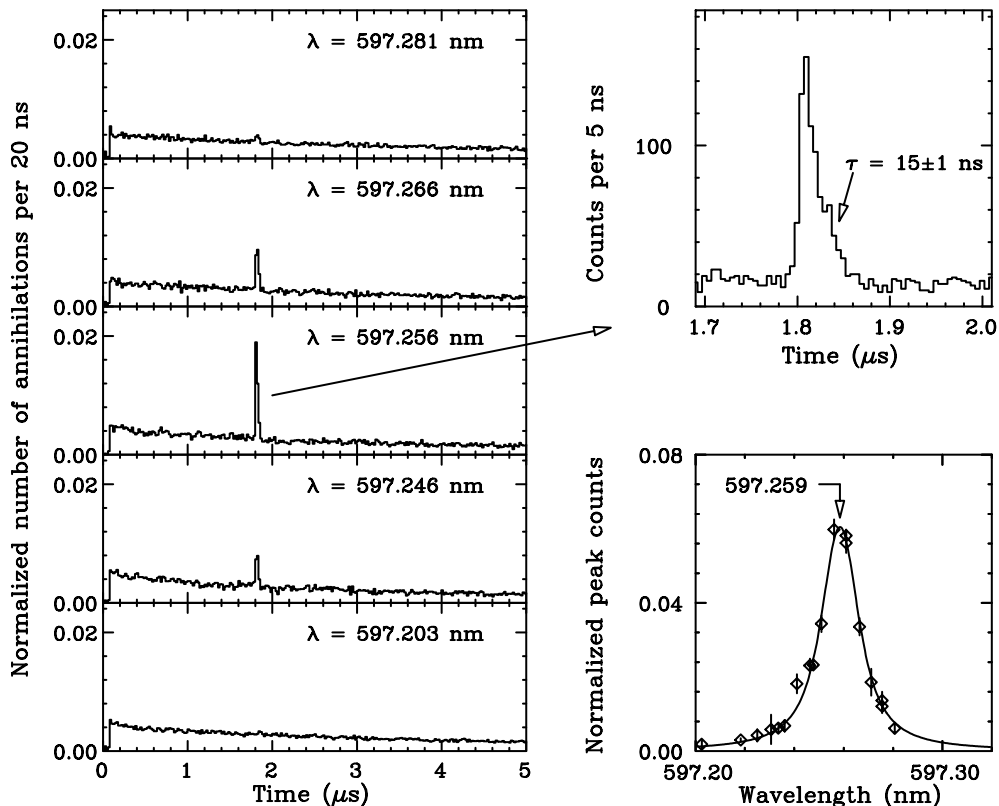


Figure 3.1: The first observation of a laser-induced annihilation signal – with $\bar{p}^4\text{He}^+$. The dependence of the intensity of the laser-induced peak on the laser wavelength (left), an enlarged view of the annihilation peak (right top) the area of the peak versus laser wavelength (right bottom) [31].

short-lived daughter state (f^+ transition in Fig. 3.2). The bandwidth of the laser is narrow enough so that the f^- transition is not excited. The antiprotons in the other HF state are not affected, which results in the desired population asymmetry. The antiprotons in the short-lived daughter state annihilate within a few nanoseconds, resulting in an annihilation peak much higher than the background and thus easy to associate to the laser-induced population. Afterwards, a microwave frequency pulse, tuned around the transition frequency between two SSHF ($\bar{p}^3\text{He}^+$) substates of the parent state, is applied to the antiprotonic helium atoms. If the microwave field is on resonance with one of the SSHF transitions, this will cause a population transfer and thus a partial refilling of one of the previously depopulated states. Then, a second laser pulse is applied to the same transition (f^+) as before which will again result in subsequent Auger decay of the transferred population and annihilation of the antiprotons. Thus, the number of annihilations after the second laser pulse will be larger if more antiprotons were transferred by the microwave pulse.

The annihilation decay products – primarily charged pions resulting from the decay of the daughter state after the two laser pulses – are detected by two Cherenkov counters (see Sec. 4). Also electrons and positrons from the further decay of the pions – in principle all annihilation products hitting the detectors during that time interval – will be detected. Prior to the first laser-induced population transfer a large annihilation peak (*prompt*) is caused by the majority of $\bar{p}\text{He}^+$ atoms which find themselves in Auger decay-dominated states and annihilate within picoseconds after formation. At later times, this peak exhibits an exponential tail due to $\bar{p}\text{He}^+$ atoms in the metastable states cascading more slowly towards the nucleus. This exponential tail, recorded as the output of the two Cherenkov counters, is called *analogue delayed annihilation time spectrum* or ADATS and constitutes the background for the laser-induced annihilation signals. As mentioned above, the daughter state has a very short lifetime of ~ 10 ns and the population transfer is indicated by a sharp annihilation peak against the background during the two laser pulses. The area under these peaks is proportional to the population transferred to the Auger decay-dominated state. Two photomultipliers (PMTs, see Ch. 4) are connected to the detectors and amplify the signal. The output voltages of the PMTs are recorded on a digital oscilloscope and produces the time spectra. The recorded voltage is proportional

Auger decaying daughter state

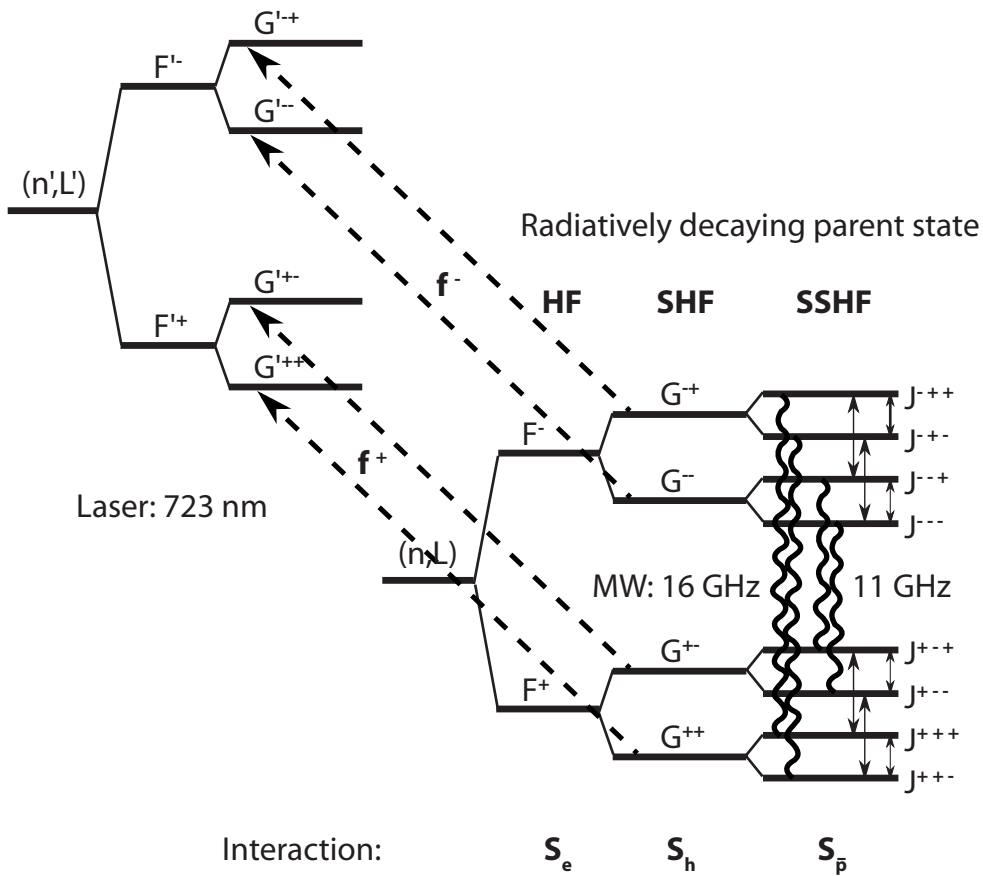


Figure 3.2: A schematic drawing of the laser-microwave-laser method. The dashed arrows indicate the laser transitions between the SHF levels of the radiative decay-dominated state $(n, L) = (36, 34)$ and the Auger decay-dominated state $(n, L) = (37, 33)$ of $\bar{p}^3\text{He}^+$. The wavy lines illustrate the microwave-induced transitions between the SSHF levels of the long-lived state.

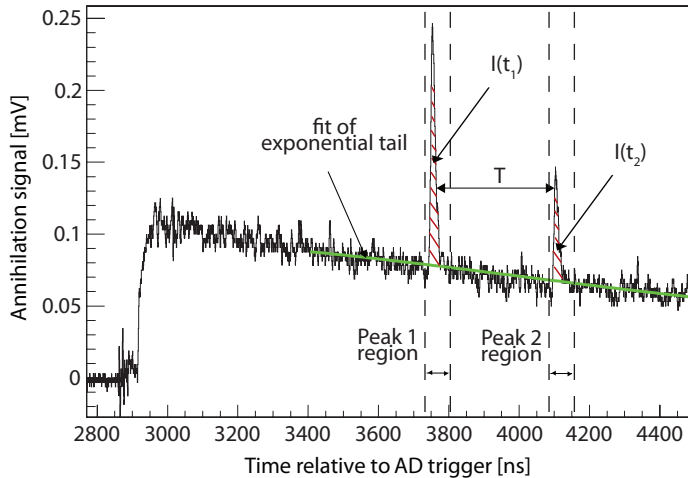


Figure 3.3: Part of the analog delayed annihilation time spectrum (ADATS) with the two laser-stimulated annihilation peaks against the exponentially decaying background of the metastable cascade. Parameter T denotes the delay time between the two laser pulses. The photomultipliers are gated off during the initial \bar{p} pulse arrival [43]. Thus, the prompt peak is cut off and only the annihilations due to the metastable state depopulation are recorded.

to the number of events, therefore it is called *analog*. The spectrum with the two laser-induced peaks super-imposed on the exponential tail is displayed in Fig. 3.3. It is essential to adjust the timing for the lasers and the microwave measurement correctly. The lasers should be delayed sufficiently with respect to the prompt peak so that the stimulated annihilation peaks appear on top of the more stable plateau of the exponentially decaying background and not too close to the strong initial rise. Since the intensity of the antiproton pulse fluctuates from shot to shot, the peaks must be normalized by the total intensity of the pulse (*total*). This ratio is referred to as *peak-to-total* (PTT) and corresponds to the ratio of the peak area – $I(t_1)$ or $I(t_2)$ – to the total area under the full spectrum (see Fig. 3.3). If the second laser annihilation peak is further normalized to the first one, the total cancels out. The frequencies of the two SSHF transitions can now be obtained as the centers of two distinct peaks by plotting $\frac{I(t_2)}{I(t_1)}$ as a function of the microwave frequency. The ratio $\frac{I(t_2)}{I(t_1)}$ is largely independent of the intensity and position of the antiproton beam. The height of the peaks in the microwave spectrum depends on the time delay between the two laser

pulses and thus also on the collisional relaxation rates which are estimated to be 1 MHz at 6 K (see Ch. 6.7) [44].

For these measurements the two pulsed lasers were fixed to a wavelength of 723.877 nm, with a pulse length of 10-12 ns – which should be longer than the Auger lifetime of 3 ns for $\bar{p}^3\text{He}^+$ to increase the laser depopulation efficiency – to induce the f^+ laser transition between the $(n, L) = (36, 34)$ and the $(n', L') = (37, 33)$ state. The laser fluence was in the range of 20-40 mJ/cm², the laser diameter \sim 5 mm. According to numerical simulations the depletion efficiency was about 90%. There are several limitations to the choice of the measured state, such as availability of a laser source in the required frequency range or the splitting of the transitions between the HF states of the daughter and the parent state. The laser transition between the $(n, L) = (36, 34)$ and the $(n', L') = (37, 33)$ state was chosen because it is easily stimulated and the primary population is large, thus leading to a large signal. The captured fraction of antiprotons for the measured metastable state $(n, L) = (36, 34)$ is $(3\text{-}4)\times 10^{-3}$ [45].

3.2 Other Systematic Investigations

Before a measurement can be carried out – in any case when a new beam-time period at CERN is started – it is essential to check, and if necessary improve, the characteristics of the antiproton beam and optimize the tuning into the helium-filled target. One way to check this is to send laser pulses, as one would do for the actual measurements, and optimize the beam based on the plotted peak-to-total ratio for the first laser pulse (for more information refer to later chapters in this work). The beam position can be changed by adjusting dipole and quadrupole magnet currents appropriately [46]. However, there are a few more studies that have to precede the actual laser-microwave-laser spectroscopy of HF substates as explained above.

Collisional Relaxation

Once the beam is ready to be used and the correct laser resonance frequency is determined from a laser scan (see Ch. 8) a few systematic checks are required in order to optimize the measurement parameters. The principal intent for all preparatory studies is to finally obtain a high signal-to-noise

ratio and a small width of the resonance lines in order to produce highly precise results. If the method explained below is repeated with sufficient statistics at several laser delay times it can provide information on the laser depletion efficiency, collisional relaxation and refilling processes and allow to determine the most appropriate delay between the two laser pulses.

In the case of the complete laser-microwave-laser technique two laser pulses and the microwave pulse in between are required. However, for this particular measurement no microwave is applied and it is carried out in two different modes. In one mode – which we refer to as AA – the first laser is shooting on resonance with the transition to be stimulated and the second laser is as well on resonance with the same transition and fired with a certain delay to the first one, with no microwave pulse in between. In the second mode – referred to as OA – only the second laser is fired, with the same delay as before, only that the first laser did not shoot (see Fig.s 3.5 and 3.6). Measurements need to be performed in both modes at an equal number of times. The transition line width is inversely proportional to the laser delay due to Fourier transform of the microwave pulse, i.e. the longer the laser delay the smaller the line width. Finding the optimal laser delay therefore means to reach a compromise between a time long enough to have a narrow microwave peak and short enough to avoid relaxation of the system through spin exchanging inelastic collisions. Refilling from higher-lying states also contributes to the equalization of the HFS substates. Two types of collisions between antiprotonic helium and regular helium atoms can be defined, elastic and inelastic collisions. The transitions which are the easiest to measure are the electron spin flip transitions – compared to antiproton spin flip transitions.

Theoretical calculations by Korenman [47] predict that for a target pressure of 250 mbar and a temperature of 6 K the collisional relaxation time for the single electron spin flip transitions in the case of the (36, 34) state in $\bar{p}^3\text{He}^+$ lies in the range of 1000 ns (for antiprotonic ^4He the most accurate theoretical results predicted a value of about 1666 ns for the same parameters [48]). The theoretical rates for $\bar{p}^3\text{He}^+$ are displayed in Fig. 3.4. These theoretical results would suggest that a short laser delay is preferable for a high peak-to-total ratio because if the delay is too long the population asymmetry created by the first laser pulse will have returned to equilibrium. However, there is another argument which leads to exactly the opposite con-

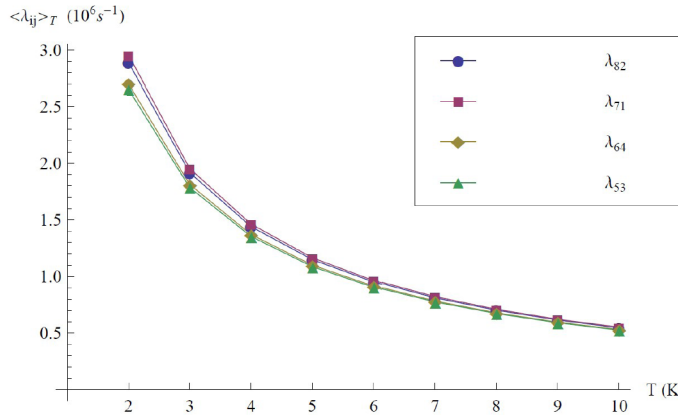


Figure 3.4: Theoretical relaxation rates for $\bar{p}^4\text{He}^+$ and $\bar{p}^3\text{He}^+$ [47, 48].

clusion, i.e. the longest "possible" laser delay to still obtain a narrow line width. The Fourier transform of the microwave pulse

$$F(\omega) = \frac{1}{\sqrt{2\pi}} \int_{-\infty}^{\infty} f(a t) e^{-i\omega t} dt = \frac{1}{\sqrt{2\pi a^2}} \text{sinc}\left(\frac{\omega}{2\pi a}\right) = \frac{b}{\sqrt{2\pi}} \text{sinc}\left(\frac{b\omega}{2\pi}\right). \quad (3.1)$$

with $\text{sinc}(x) = \frac{\sin(x)}{x}$ delimits the width of the resonance line. $f(a t)$ defines a rectangular pulse function with $a = \frac{1}{b}$ and b being the full width. In our case – in Eq. 3.1 – b equals the laser delay T since the applied microwave pulse starts before the first and ends after the second laser pulse. The resonance line width is proportional to $\frac{1}{T}$. Due to the thermal equilibrium of the state before the first laser pulse the atoms can be affected by the microwave only during the delay time T – or more precisely after the first laser depopulation.

Microwave Power Studies

The transitions between hyperfine substates which are stimulated by a radio frequency pulse are single-electron spin flip transitions. The electric dipole moments that are activated during a laser transition are several orders of magnitude larger than the magnetic moments. In the case of laser spectroscopy one can ensure high enough population transfer by saturating the respective transition. The spin flipping due to *Rabi oscillation* of the magnetic dipole moments in the microwave-induced oscillating B-field is much slower and the states are not decaying immediately in contrast to the daughter state of the laser transition.

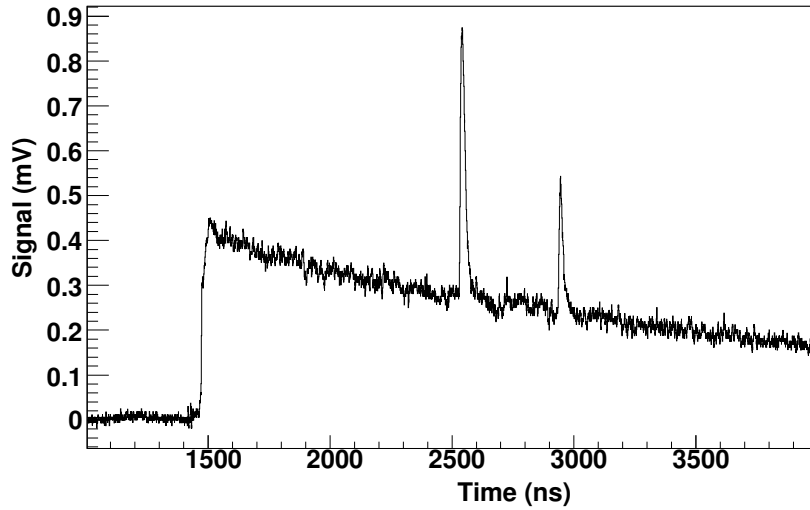


Figure 3.5: The ADATS signal for the case of both laser annihilation peaks being recorded [26].

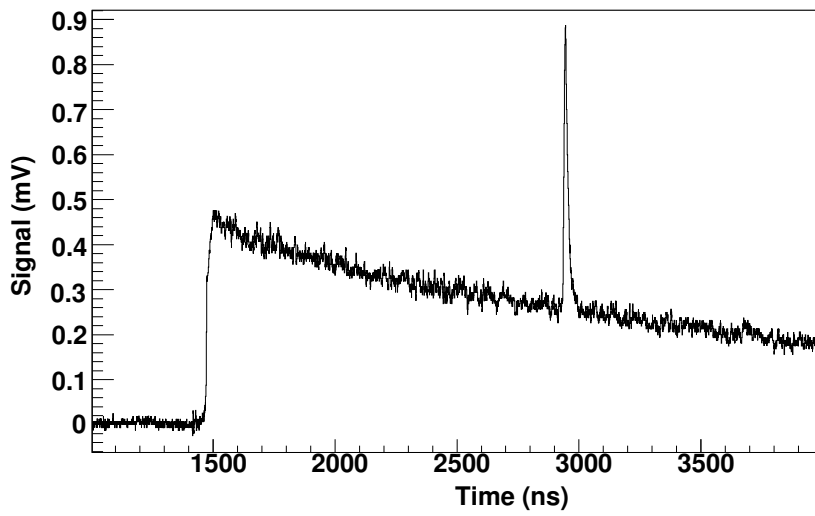


Figure 3.6: The ADATS signal for the the case where only the second annihilation peak was recorded. The height difference of the second peak reflects the depopulation of the first laser pulse in Fig. 3.5. Both graphs were produced with approximately the same number of delayed annihilation events [26].

Rabi Oscillations In a static field \vec{B}_z which lies along the z direction, a magnetic moment $\vec{\mu}$ precesses with the Larmor frequency γB_0 , where γ is the gyromagnetic ratio. If a rotating magnetic field \vec{B}_1 is introduced in the x - y plane with a frequency at the Larmor frequency then ω equals γB_z . The total magnetic field is given by

$$\vec{B}(t) = B_1(\hat{x} \cos \omega t - \hat{y} \sin \omega t) + B_z \hat{z}. \quad (3.2)$$

The moment precesses about the field at a rate called the *Rabi frequency* $\Omega = \gamma B_1$. If the moment initially lies along the z axis, then it rotates in the y - z plane. The z -component of the moment is given by $\mu_z(t) = \mu \cos \Omega t$. At time t it has precessed through an angle $\phi = \Omega t$. At $T = \pi/\Omega$, half a period, the moment points along the negative z -axis and therefore has flipped over.

After one complete Rabi oscillation the system would again be in the initial state. In order to optimize the amount of population transferred, a π -pulse has to be induced – so called because only half of a 2π Rabi oscillation should be completed during the microwave pulse which stimulates a transition between two HF substates. In addition to numerical simulations it is important to determine and verify also experimentally the correct microwave input power required to achieve – in the ideal case exactly – one π -pulse. Therefore, both lasers are fixed to the resonance frequency for the f^+ transitions and the microwave is applied over the entire interval between the two laser pulses. The frequency is not scanned as for the actual measurement but fixed to one of the (numerically simulated) SSHF transition frequencies. This is done – with sufficient statistics – for several values of the input RF power. From these data the optimum power for a certain laser delay can be determined (see Ch. 8.3 for details).

Chapter 4

Experimental Setup

4.1 Antiproton Decelerator (AD)

The measurements were all performed at the Antiproton Decelerator (AD) at CERN [49]. The initial momentum of the antiprotons is $3.5 \text{ GeV}/c$. They are produced by the collision of $26 \text{ GeV}/c$ protons from the Proton Synchrotron (PS) with an iridium production target. The antiproton bunches emerging from these collisions are separated and focused by magnetic horn-type lenses and fed into the AD ring where they go through a complex cooling process (see Fig. 4.1). The antiprotons are at first stochastically cooled [50]. During the first stochastic cooling step the momentum profile – precisely the vertical and horizontal deviation of each antiproton from the ideal beam position – is measured with pickup electrodes and at the opposite side of the decelerator ring electric fields are applied via kicker electrodes in order to steer the beam of antiprotons. The steering is proportional to the signal from the pickup electrodes for every antiproton. This process should finally reduce the emittance of the particle beam – ideally about 1 mm mrad to have a beam diameter of 1 mm in the target. A radio frequency cavity slows them down to an energy of $2 \text{ GeV}/c$. In order to compensate for the adiabatic blow-up of the beam width during the deceleration process another stochastic cooling cycle is applied. Once the antiprotons are decelerated to 300 MeV the beam size, divergence and energy spread is further reduced with electron cooling and again at 100 MeV. The final antiproton bunch that is produced in the ring before it gets ejected to the experiment beamlines, has a size of $1 - 4 \times 10^7$ particles, a pulse length of 200 ns (at FWHM) and a kinetic energy of 5.3 MeV. A bunch can be ejected on average every 90-

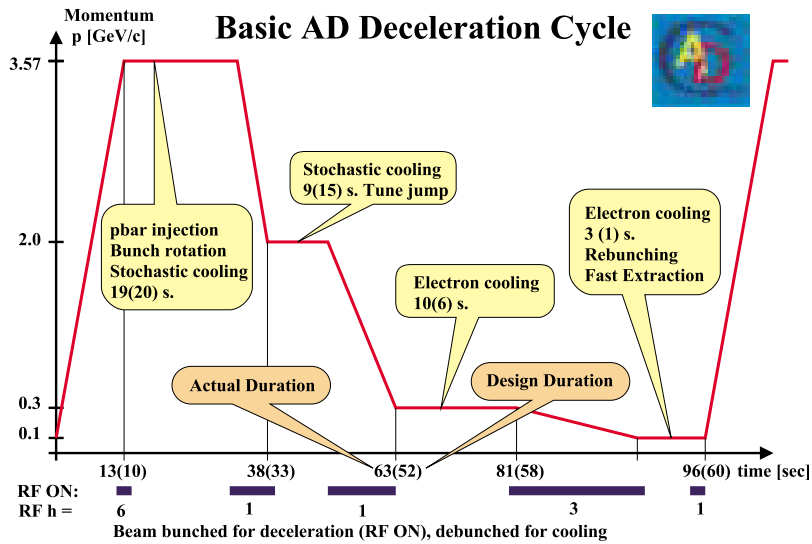


Figure 4.1: AD cooling cycle – the antiproton beam momentum as a function of time during the AD deceleration cycle [49].

110 s. On the way through the decelerator ring as well as in the individual beamlines there are several so-called *wire-chambers* (MWPC) which can be remotely inserted into the beamline to measure the profile and the intensity of the antiproton beam. They can be only used during step-wise steering of the beam since it prevents the beam from circulating once they are inserted. At the very end of the beampipe leading to our experimental area we place a non-destructive beam profile monitor (BPM) [51] to measure the profile in x and y direction again about 15 cm before it enters the measurement target.

4.2 Cryogenic System

The antiprotons are stopped in a helium gas target which has to be cooled down to a temperature of about 6 K (primarily to reduce the Doppler broadening of the measured transition lines). Therefore the microwave setup is enclosed in a cryostat. An isolation vacuum prevents a heating-up of the cryogenic liquids contained within the thermal shield. To cool the target,

liquid helium is passed through a cooling loop above the target chamber. In the target region, i.e. reaching about 30 cm above and below it, a 1 mm thick mu-metal magnetic shielding was mounted around the vacuum chamber – leaving out a window on the two sides where antiprotons and laser beam enter. If a constant magnetic field is present the linewidth of the resonance lines increases by 2.8 MHz/G. Thus the field in the target volume should be less than 0.1 G in order to ensure that the caused broadening remains less than about 10% compared to the natural line width of about 2 MHz. The present field distributions and effects of external magnetic fields with different shielding thickness were assessed in simulations (Maxwell, ANSYS [52]). Field measurements inside the shielding confirmed that the maximum magnetic field strength inside the cavity can be reduced to below 0.05 G (instead of 0.6 G before due to the earth magnetic field) with a 1 mm shielding. To perform this test we used Hall effect sensors. If the sensor is placed perpendicular to the magnetic field lines the probe allows a measurement of the magnetic flux density. A current is induced in the Hall probe – usually an indium compound semiconductor crystal – developing a voltage across the crystal which is proportional to the measured field.

The antiprotons reach the target upstream through an 50 μm thick Upilex window which separates the isolation vacuum from atmospheric pressure. The target is on this side closed by a 25 μm titanium foil glued into a brass mounting – indium-sealed (see Fig. 4.2). Outside the vacuum chamber one or more Upilex foils can be fixed to further control the slow-down of the antiprotons in order to stop them centrally within the microwave cavity. The experimental method and the general design of the setup were the same as for $\bar{p}^4\text{He}^+$ [53]. However, a new cryostat with compressor-based cooling system was built which led to improvements of the operation and more efficient use of the measurement time. Previously a liquid helium- (and nitrogen-) operated cryogenic system was used. This required a time-consuming process to refill the coolants at least once during each beamtime shift. It was decided to build the new system as a close-circuit cryocooler – with hermetically sealed targets cells to minimize the amount of required ^3He gas. The microwave cavity was now cooled directly by mounting it on a coldhead. Only the cavity was filled with the helium gas and by means of the coldhead cooled down to about 6 K. Liquid nitrogen and liquid helium were no longer needed for the cooling process. The temperature stabilization

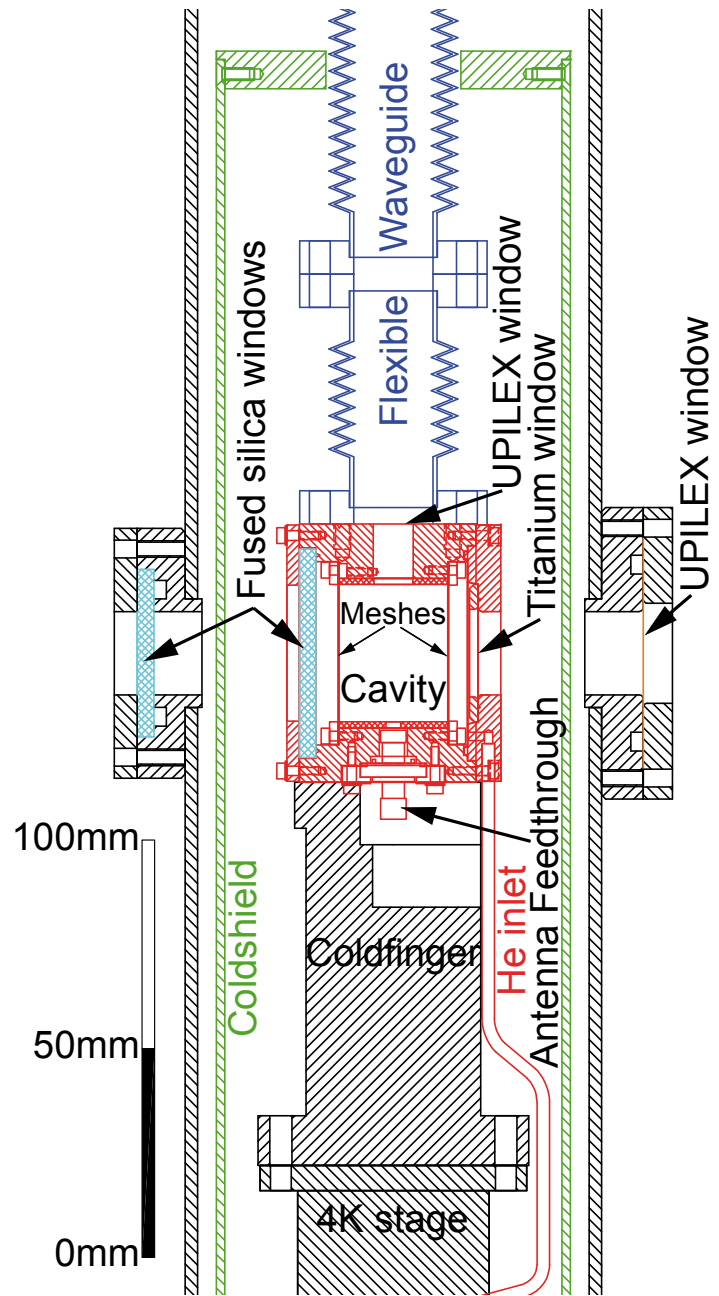


Figure 4.2: Drawing of the central part of the experimental setup [10].

was much faster compared to the old system. The cryostat could be operated continuously and thus saved $\sim 10\%$ of beamtime previously needed for refilling of the cryogenic coolants. Large scale temperature changes such as during refilling – as happened with the previous setup – were avoided and the risk of leaks and (or due to) too high pressure was minimized. A schematic view of the complete experimental setup is shown in Fig. 4.3. The cryostat (Fig. 4.2) was designed based on a two-stage coldhead (RDK-408D2, 1st stage: 50 W at 36.4 K, 2nd stage: 1 W at 4.01 K, Gifford-McMahon cooling cycle) combined with a compressor (CSW-71D), both obtained from Sumitomo Heavy Industries. A two-stage cooling configuration with an aluminium coldshield around the target cell was indispensable to avoid warming up by heat radiation.

The coldshield was made from a square shaped aluminium tube with an inner side length of 80 mm, a wall thickness of 2 mm and a height of 452 mm. The shielding was screwed to the first (50 K) stage of the compressor by a transition piece. Two circular holes of 20 mm diameter were machined into the coldshield to allow the antiprotons and the laser beam to reach the target cell. For the waveguide leading the microwaves (synthesized by a vector network analyzer, VNA, Rhode & Schwarz ZVB20, and amplified by a traveling wave tube amplifier (TWTA, TMD PTC6358) into the cavity. The gas-pipe and several clearances for the wires were cut out of the coldshield. Each of the openings was small enough to still ensure sufficient heat radiation shielding. For improving the performance of the coldshield, it was wrapped in super-insulation foil (with the circular holes mentioned above left open). During the experiment the coldshield ultimately reached a temperature between 45 K and 50 K (depending on the target cell and the experimental gas pressure used), offering sufficient heat radiation shielding. The waveguide – one of the main heat bridges – was made from (0.1 mm thin) seamless flexible brass waveguide parts (WR75, 10-15 GHz respectively WR62, 12.4-18 GHz made by Flexiguide Ltd.) wrapped in superinsulation to achieve a low heat input and to compensate for the thermal expansion of the setup. Additionally the heat gradient was minimized by maximizing the length of the waveguide (908 mm from the top feed-through into the insulation vacuum at room temperature down to the cavity at about 6 K) [10].

Three temperature sensors recorded the temperature behavior of the

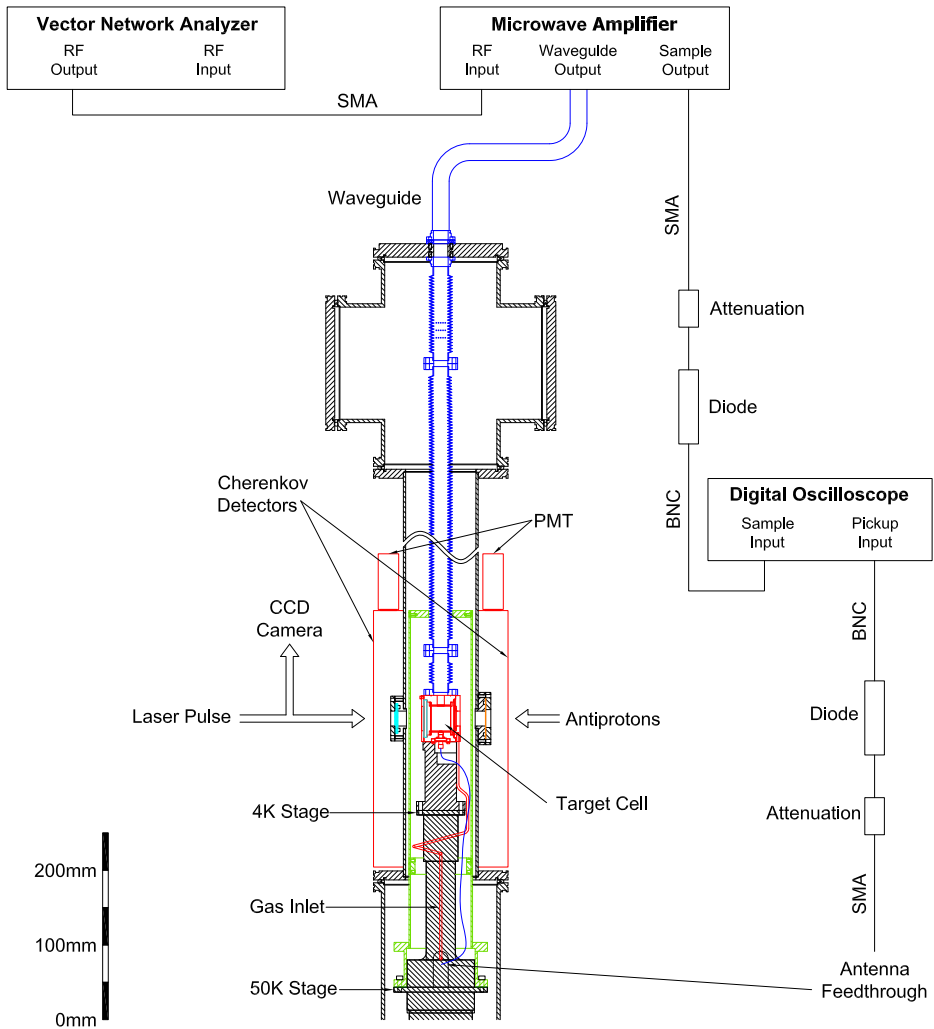


Figure 4.3: The schematic drawing provides an overview over the experimental setup including also electronic components. The vector network analyzer synthesizes the microwave signal which is then amplified and sent through the waveguide system to the target. SMA (SubMinia-
ture version A, coaxial radio frequency connectors) and BNC (Bayonet
Neill-Concelman, miniature quick connect(disconnect) radio frequency
connector) denote the cable types. For more details refer to Ch. 5.

cryostat and were read out by an auto-tuning temperature controller (Lake-shore 331S). To control the target temperature two heating resistors (10 Ohm each) were mounted on the cold finger between cold head and target cell. The silicon diode on top of the target cell was implemented as control loop for the temperature controller to stabilize the target temperature together with the two heaters.

4.3 Gas System

Outside the cryostat and vacuum chamber a gas system had to be developed for the following tasks: cleaning the experimental ^3He gas from chemical impurities before filling the target cell, recuperating the used helium in order to avoid losing this expensive gas, avoiding overpressure in the experimental setup, respectively relieving it without losing ^3He . For cleaning purpose a liquid nitrogen-operated cold trap filled with molecular sieve was installed in the system. The recuperation system consists of two pumps, leading the helium back into its original bottle and pressurizing it up to 3 bar. For safety reasons, an overpressure valve opening at 1.8 bar venting the gas into an 1 U.S. Gal. (approx. 3.8 l) expansion bottle had to be installed. With this valve installed, an uncontrolled warmup of the system puts no risk on the setup as the weakest part of the gas system (the titanium window of the target cell) can withstand > 4 bar, so the expansion of the gas into the expansion volume starting from 1.8 bar pressure inside the target cell results in a sufficiently large safety margin with regards to the relatively low overpressures used in this experimental setup. The usual gas pressure was in the range of 150-500 mbar.

4.4 Laser Spectroscopy Setup

The laser system is in principle the same as was used for the measurements with antiprotonic ^4He – except for different laser wavelengths. It is a pulse-amplified CW laser system [34] with a narrow linewidth of about 100 MHz. This enables to depopulate only one of the two HF lines, i.e. from the biggest splitting, without affecting the other line. The laser pulse length was about 12 ns for the first laser and about 8 ns for the second laser pulse, longer than the Auger lifetime, and hence leads to a high depopulation

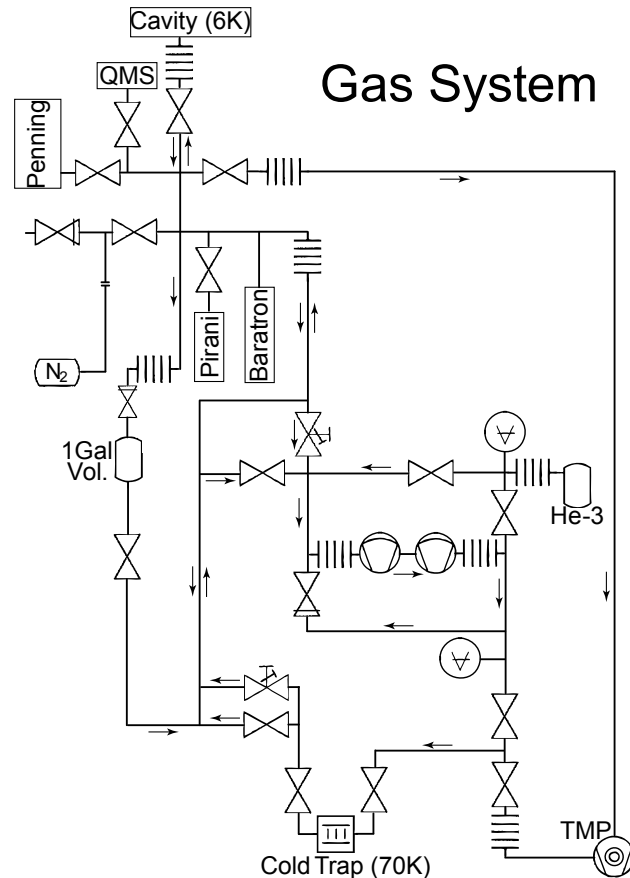


Figure 4.4: Schematic drawing of the gas system, all components at room temperature (if not marked different) [10].

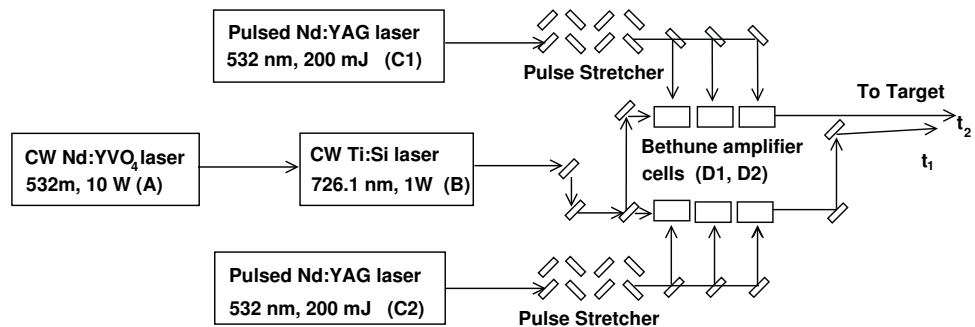


Figure 4.5: A schematic view of the setup for the laser system [26].

efficiency. One could further choose any desired time delay between the two laser pulses. The ability to select a longer delay to the second laser pulse potentially allows to reach a better resolution, i.e. narrower laser resonance lines. Figure 4.5 provides an overview of the essential part of the laser setup. A ring Ti:sapphire laser (Coherent MBR-110, (B)) – which is pumped by a Nd:YVO₄ laser (Coherent Verdi, (A)) – produces a continuous-wave (CW) laser beam at the required wavelength $\lambda = 723.877$ nm (line width $\Gamma = 1$ MHz, power $P = 1$ W). Then this beam is split up into two seed beams each of which goes through three Bethune dye cells (D) – pumped each by a pulsed Nd:YAG laser (Coherent Infinity, (C)) with $\lambda = 532$ nm, energy $E = 200$ mJ and laser pulse length 3 ns – where it is amplified. The pump beams are split into seven beams for one and five for the other laser in order to achieve the length of the final pulses. To these (incremental) delays can be added. Finally they are merged to obtain the stretched pulses that are further sent to the Bethune cells. The pulse emitted from these cells have a width of 60 MHz and an energy of 30 mJ. The emitted fluence at the experimental target is in the range of 5mJ/cm² to 20mJ/cm² and have a diameter of 6 mm for the first laser pulse and 5 mm for the second pulse. The final laser fluence as well as the diameter can be fine tuned and adjusted manually before every shift. The laser wavelength can be determined with a wavemeter (ATOS lambdameter LM-007). The lasers enter the target downstream through two fused, uncoated indium-sealed silica windows of 50 mm diameter and a thickness of 4 mm. The timing of the laser pulses is monitored with a laser diode.

4.5 Detector Setup & Experiment Control

When the Auger state decays and the antiprotons annihilate with the protons in the helium nuclei, they produce particle showers including charged pions. Cherenkov counters detect those pions – as well as some electrons and positrons. They are mounted on two opposite sides of the target just outside the vacuum chamber which enables them to cover 2π steradians around the microwave cavity, i.e. the interaction region. Another much bigger (about 1 m \times 30 cm) Cherenkov counter is placed further away from direct beam, just next to the end of the beamline, recording the prompt peak. It is therefore an important means to observe timing and intensity of the antiproton

beam. The detectors are built of UV-transparent Lucite plates, in total about 50 cm long and 2 cm thick, with a triangular transmission piece at the end where the photomultipliers are connected. To protect them from light entering the detector material the counters are completely wrapped in black plastic tape. The fine-mesh photomultipliers (PMT, Hamamatsu Photonics R5505 GXASSY2) [43] are custom-made. The two photomultipliers at the counters around the target are gated off for several 100 ns after the arrival of the antiproton pulse. This way only the signal from annihilations products of the 3% newly formed atoms which remain in a long-lived state will be amplified by the PMTs and recorded. The 97% stopped antiprotons that annihilate immediately will thus be cut off. The PMTs need to be gated appropriately and their gain and pre-amplification have to be adjusted. The current of the gated photomultipliers are then producing the time spectra on which all analysis is based. The resulting ADATS (see also Ch. 3.1) are recorded on a digital oscilloscope (DSO) and the data stored in ROOT files [60].

The entire experimental activity is controlled and processed via Labview¹ by a remote computer in the *counting house* (a container inside the AD building serving the experimenters to survey the measurements and data acquisition). In Fig. 4.6 is illustrated a schematic overview of the entire experimental setup triggering and timing control. The timing of the microwave pulse, the pump lasers and the PMTs is controlled by Stanford Research (DG535) signal generators which are triggered by the pulse from the AD.

¹Laboratory Virtual Instrumentation Engineering Workbench - a visual programming language from National Instruments (NI)

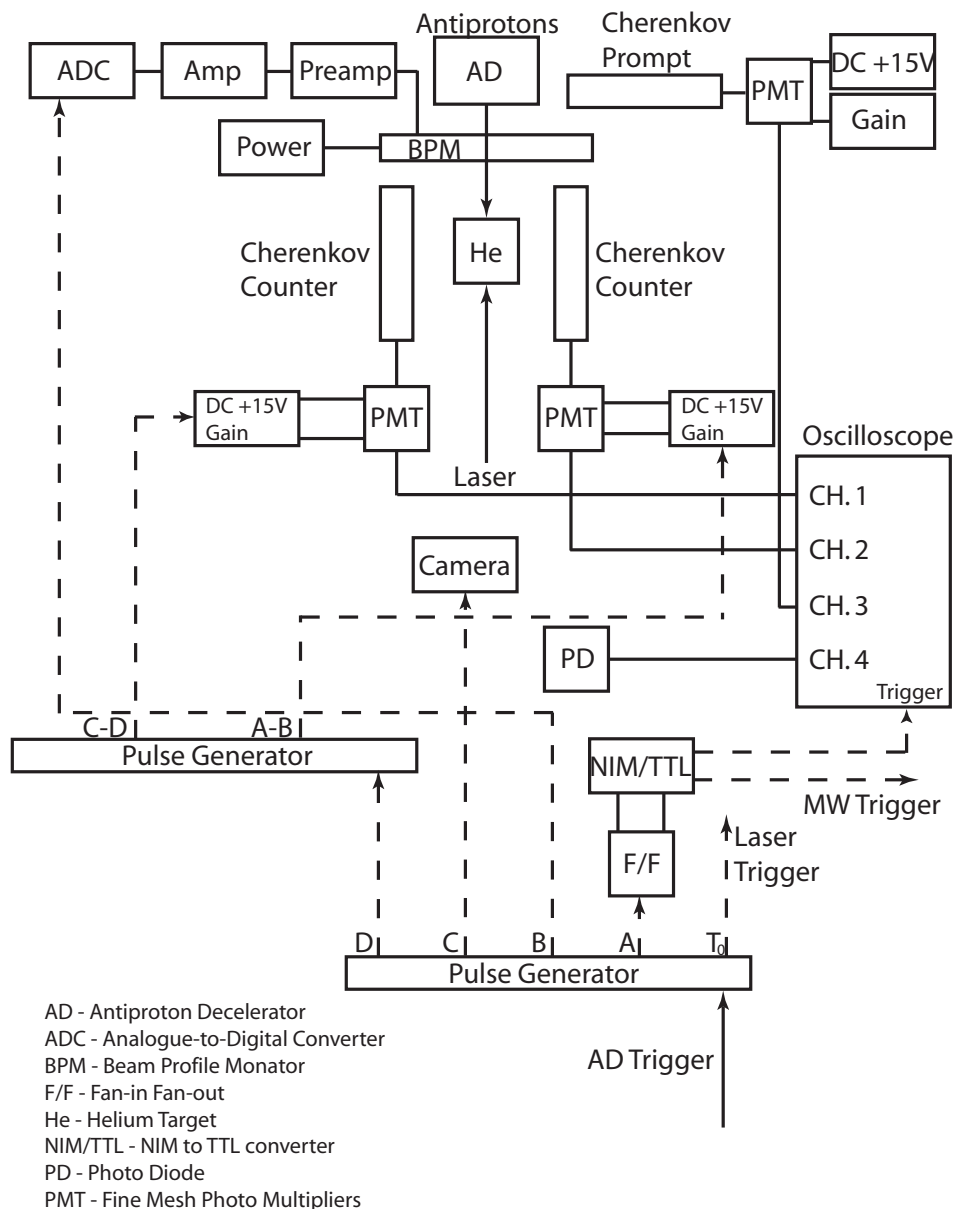


Figure 4.6: Overview of the timing and trigger system during the experiment.

Chapter 5

The Microwave Spectroscopy Apparatus

5.1 Microwave Cavities

For the measurements with antiprotonic ${}^3\text{He}$ a new cryogenic system was implemented. Furthermore the hyperfine substate transitions for this new three-body system were in an entirely different frequency range. As a consequence also the microwave apparatus had to be partially adopted and new structures for the desired frequency ranges had to be built. The heart of the experimental setup is the microwave cavity, a cylindrical resonator – the helium-filled measurement target and interaction region. The following chapters will provide detailed insight into the whole development process, preparations and tests.

5.1.1 How to Design a Microwave Cavity

There are four transitions for the $(n, L) = (36, 34)$ state of $\bar{p}{}^3\text{He}^+$ that can be induced using microwave radiation – two at about 11 GHz and two around 16 GHz. Out of these four allowed SSHF transitions two of them lie within 32 MHz from each other. Therefore, these two transitions can be measured with a single cavity of central frequency $\nu_c = 11.14$ GHz which is centered between the two transition frequencies. For the other two lines another cavity with a resonance frequency of 16.13 GHz had to be simulated and constructed.

A third new cavity was built and tested for the already measured state

$(n, L) = (37, 35)$ of $\bar{p}^4\text{He}^+$ – to conclude a study on collisional effects and to verify the new experimental setup.

In general the central frequency of a cylindrical microwave cavity is defined by its dimensions – length l and radius r . Within the present setup it is oriented in a way that the antiproton beam and the laser beam enter along the axis of the cavity. Two meshes on both faces of the cylinder confine the radio frequency field inside the cavity, still allowing laser and antiprotons to enter the target. Radius and length – and their ratio $(\frac{2r}{l})^2$ – also determine which field modes can resonate inside the cavity and at which frequency. For this experiment the transverse magnetic mode TM_{110} for a cylindrical resonator was chosen, the lowest possible mode. The field is entirely transverse, with the least number of nodes (zero) in propagation direction of the antiproton beam. The mode is parallel to the target axis and independent of the target length (i.e. of the beam direction). Thus the antiprotons entering the cavity experience the same field magnitude over the whole range. A homogeneous field in axial direction, i.e. over a large range in the direction of the antiproton beam, proved to be useful in order to be less sensitive to the stopping region of the particles in the gas. The measurement further required that the field distribution is uniform over the region where the laser is applied which is usually smaller than the diameter of the slowed-down antiproton beam to achieve sufficient laser power density. A broad resonance bandwidth of the cavity is necessary to allow scanning over a large enough frequency range in order to measure two close lying of the four *allowed*¹ SSHF transitions with the same cavity at an equal power and magnetic field strength [54]. The field is measured with a small pin antenna opposite to the waveguide input to the target. Thus the power in the cavity can be monitored and the input power adjusted for every measured frequency point.

From the representation of the recorded frequency spectrum on a *Smith chart* one can extract the *Q factor* of the resonator (appendix A). Two types have to be distinguished, the *unloaded* and the *loaded* Q value, defined as

$$Q_0 = \frac{\nu_0}{\Delta\nu} \quad (5.1)$$

¹Single electron spin-flip transition – in contrast to antiproton, electron and nuclear spin-flip transitions together which would require several times more power. Allowed transitions have a high probability to occur, for example in short-lived radioactive decay states. Forbidden transitions in contrast are unlikely to occur.

and

$$Q_L = \frac{Q_0}{1 + \beta} \quad (5.2)$$

respectively, where ν_0 denotes the resonance frequency, $\Delta\nu$ the difference of the frequencies on each side of the central frequency ν_0 at the full width half maximum (FWHM) -3 dB. The coupling factor β can be given as

$$\beta = \frac{1 + \Gamma}{1 - \Gamma} \quad (5.3)$$

with Γ being described by the impedances as

$$\Gamma = \frac{Z - Z_0}{Z + Z_0}. \quad (5.4)$$

This factor defines the ratio of the power loss in the transmission line to the loss inside the resonator $\frac{\Omega_{\text{shunt}}}{\Omega_{\text{load}}}$, with a load of 50 Ohm [55]. The parameter Z denotes the electrical impedance and Z_0 is the characteristic impedance of a uniform transmission line. A large β means that the system is over-coupled and Q_L is much smaller than Q_0 . Over-coupling results in a broader eigenresonance of the cavity.

As will be explained in Sec. 5.5, with the setup used for the studies of $\bar{p}^4\text{He}^+$ it was aimed to produce sharp eigenresonances, i.e. a high Q factor, of the cavity to achieve high power in the cavity. This requirement had to be fulfilled at every measured frequency point. Therefore the central frequency of the cavity had to be changed from point to point over the scanned frequency range which could be achieved through different choke positions of a so-called *triple-stub-tuner* (TST, for details read appendix A). In the current microwave apparatus over-coupling was produced on purpose, aiming at a broad resonance in order to allow two close-lying transition lines to be measured with the same target without the use of triple-stub-tuner. The difference between these two transitions is about 32 MHz. The defined tuning range should be wide enough to include also the tails of the two lines. To achieve a sufficiently broad resonance with an appropriate full width half maximum in the order of 100 MHz the cavity is over-coupled to the waveguide system (WG75 and WG62 for the different frequency ranges ²) through an *iris*, a rectangular aperture in the wall of the resonator. If a closed cavity with no iris is assumed, one would obtain a sharp resonance at

²Flexiguide Ltd.

its central frequency and therefore only one transition equal to the central frequency could be measured. By over-coupling the cavity to the waveguide system this can be overcome and a sufficiently broad resonance created. The loaded Q value should ideally be in the range of 100 to result in a resonance width of ~ 100 MHz. The two close-lying transitions can then be studied with the same target, at an equal power level. In the case of an ideal sharp eigenresonance of the target, i.e. perfect matching to the transmission line, all power will be transmitted to the target at the resonance frequency while at other frequencies the power will be reflected. Therefore the drawback of this method is that it requires considerably higher input power.

The unloaded Q value, referring to a completely closed cavity, is usually much higher and can be calculated through the relation

$$Q \frac{\delta_s}{\lambda_0} = \frac{P_{nm}}{2\pi(1 + \frac{a}{d})} \quad (5.5)$$

where λ_0 is the resonance wavelength, d is the axial length and a the diameter of the cavity. $P_{nm} = 3.832$ denotes the root of the Bessel function for the TM_{110} field mode. δ_s is the skin depth $(\frac{\omega\mu\sigma}{2})^{-\frac{1}{2}}$. Here $\omega = 2\pi\nu$ is defined as the eigenresonance frequency of the cavity, the electrical conductivity $\sigma = \frac{1}{\rho}$ is the inverse of the resistivity $\frac{RA}{L}$ with R being the electrical resistance of the material, L the conductor length and A the cross sectional area. The magnetic permeability is $\mu = \mu_r\mu_0$ with μ_r being the relative permeability of the material and $\mu_0 = 4\pi \times 10^{-7}$ H/m. The skin depth is the distance at which the field in a conductor decays by e^{-1} [56] and was calculated to be $\sim 2.9 \mu\text{m}$ for all cavities.

The calculated unloaded Q_0 was determined as 3513 and 2806 respectively for the 11 GHz and the 16 GHz cavity resulting in a loaded Q_L of 160 MHz for the 11 GHz and 100 MHz for the 16 GHz cavity. The loaded Q values were extracted from a measurement of the transmitted frequency spectrum (see Sec. 5.4).

When designing the target, the width of the resonance can be optimized by changing the iris dimensions – and consequently also the central frequency shifts which can be readjusted through the radius. The length may also have to be adapted in order to exclude interferences with other field modes. The iris size is particularly crucial for a successful measurement since it may not only influence resonance frequency and width, but cause polarization degeneration of the mode(s) in the cavity.

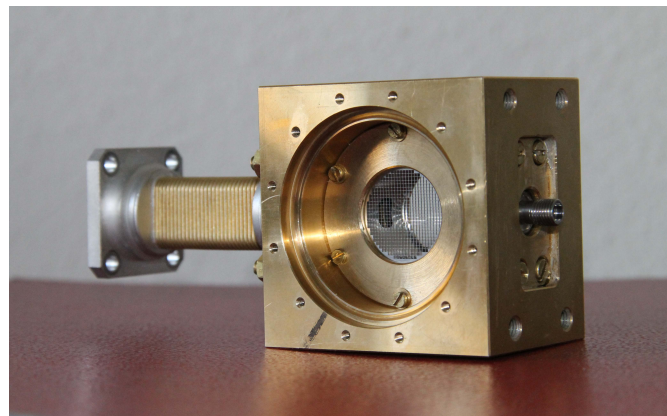


Figure 5.1: These are pictures of a microwave target as they were built to fit the experimental setup attached to a short waveguide piece where the microwave pulse is inserted during the experiment.

5.2 Simulations of the Microwave Cavities

The complete microwave part of the setup was designed using the High Frequency Structure Simulator HFSS Software [57]. It is essential to simulate the correct dimensions for the cavity in order to obtain the right central frequency, resonance width and microwave power. Other resonating modes which may interfere with the required field mode have to be excluded. Figure 5.2 shows a 3D model that was designed for the simulations. It essentially consists of the cylindrical resonator, the iris that couples the cavity to the waveguide, the antenna and the pickup output which couples to an SMA cable. For simplicity and less simulation runtime only a waveguide

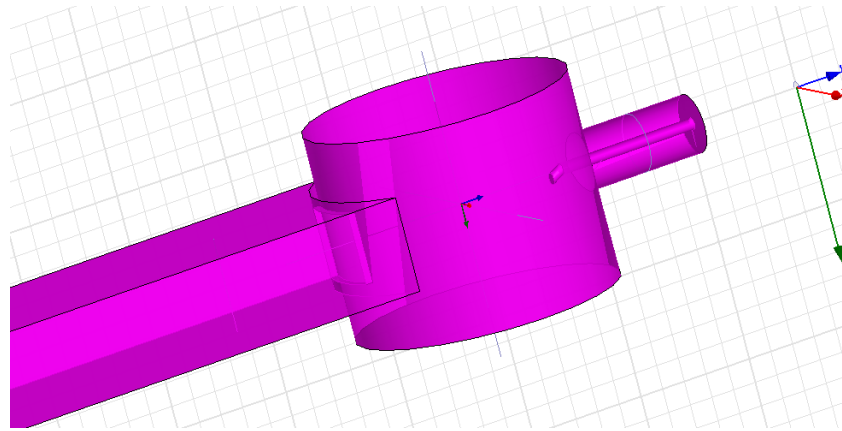


Figure 5.2: 3D simulation of the microwave system with HFSS [57].

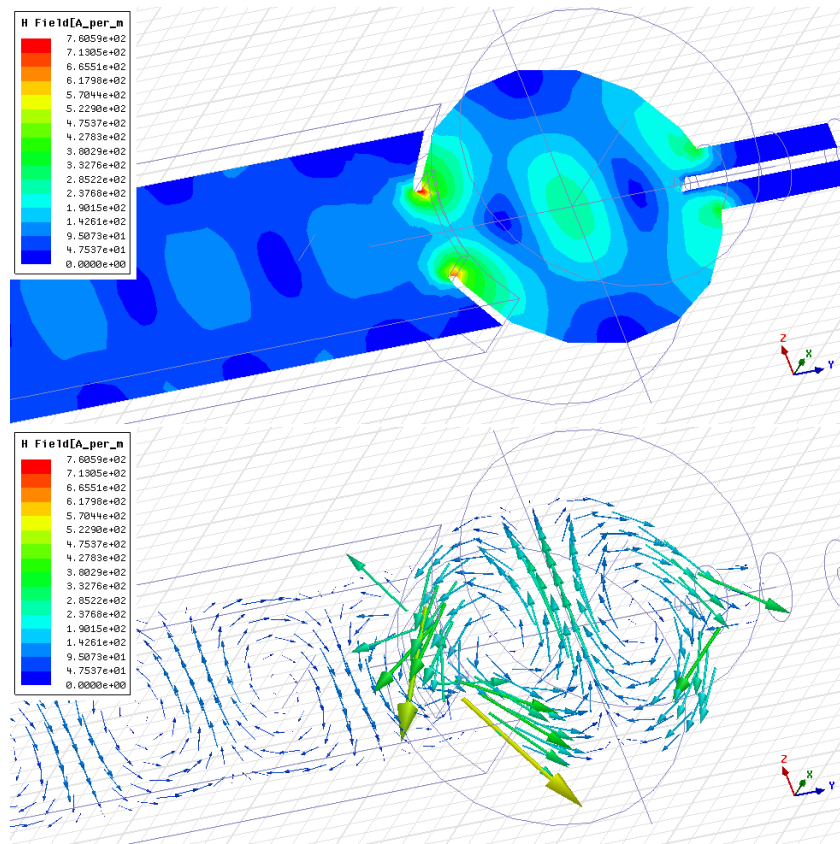


Figure 5.3: Simulations of the magnetic field distribution in the microwave system. The picture on top displays the magnitude of the magnetic field and the picture at the bottom the magnetic vector field in cavity and waveguide [57].

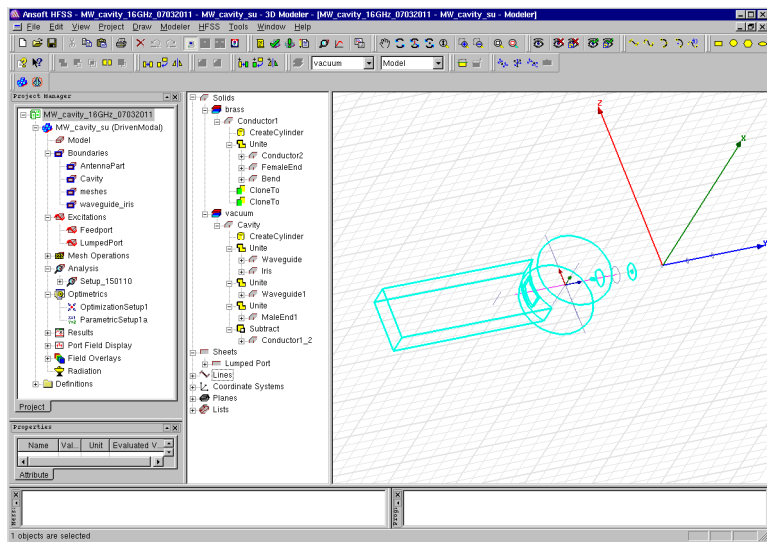


Figure 5.4: This is the graphical surface of the HFSS simulation software.

piece of 5 cm is assumed in the model and also the output line is cut off. Simulations were initially done for several very different lengths of waveguide with no noticeable influence on resonance frequency or change of resonance width. The meshes were tricky to simulate and thus simply replaced by thin plates in the model.

Once the model is created and parameters named, starting values for all variables, such as dimensions for the single parts of the design, electrical conductivity, input power (sent to the setup), input frequency, frequency steps for the analysis, surface roughness and a solution frequency can be chosen. The material is defined indirectly. All matter parts are assumed to be vacuum and designated a certain electrical conductivity. Thus also different temperatures could be simulated – by applying the according calculated conductivity value. In order to allow signal reflection and transmission parameters to be calculated during the analysis, it is necessary to define excitations for the input and output. Finally the model can be solved either for the given parameters, choosing one or several of them to be solved for a number of different designated values or optimizing one or more parameters within a range.

There is a variety of ways to display the results. The *scattering parameters* S are providing information on reflection and transmission – the easiest method to check the frequency spectrum and in particular the width, fre-

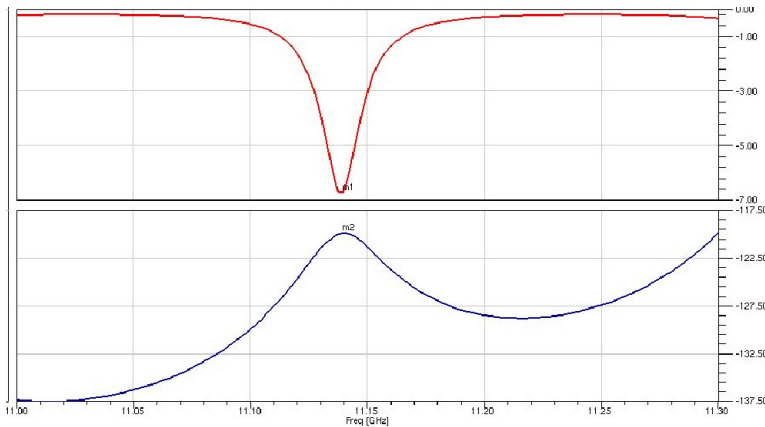


Figure 5.5: The simulated reflection and transmission signals (in dBm) for the 11 GHz cavity.

quency and amplitude of the desired resonance signal. These parameters are given through the following relations.

$$S11 = \frac{\text{Power}_{\text{reflected to port1}}}{\text{Power}_{\text{emitted from port1}}} \quad (5.6)$$

is the reflection coefficient – if no signal is emitted from port 2.

$$S21 = \frac{\text{Power}_{\text{transmitted to port2}}}{\text{Power}_{\text{emitted from port1}}} \quad (5.7)$$

denotes the transmission coefficient. Port 1 and port 2 refer to the emitting and receiving port of the signal synthesizer respectively. These parameters (usually given in dB³) can provide important information on the investigated system, losses etc. Fig. 5.5 displays S11 and S21 exactly at the frequency of one of the transition lines, i.e. on resonance, and at another frequency point off resonance. The results may as well be illustrated using a Smith chart which provides information on the impedance of the transmission line.

5.2.1 Simulation Studies

At first the parameters for the 13 GHz cavity – that was used for the $\bar{p}^4\text{He}^+$ measurements – were reproduced to confirm the reliability of the simulation

³dB is a logarithmic function for comparing powers, defined as $\text{dB} = 10 \log(\frac{P_1}{P_2})$. The unity dBm is considered a special case of dB where – both powers given in mW – P_2 is always assumed to be 1 mW. It is defined as $\text{dBm} = 10 \log(P_{\text{mW}})$

model. To calculate eigenmode solutions and check if the resulting unloaded Q values agree with calculated parameters, the resonator was modelled as a closed system without external coupling. Assuming a closed cavity, the expected dimensions for the right mode and wavelength can be calculated as a reference point for the simulations by means of a *mode chart* (see Fig. 5.11 and Sec. 5.4.1 for explanation), to have a rough idea of the model dimensions beforehand. There is one essential equation which relates the desired central wavelength to the resonator dimensions:

$$f_{nml} = \frac{c}{2\pi} \sqrt{\left(\frac{P_{nm}}{a}\right)^2 + \left(\frac{l\pi}{d}\right)^2} \quad (5.8)$$

The index n is the circumferential variation, m the radial variation and l – the third index of a mode TEM_{nml} – denotes the half-period variations in z propagation direction.

For the closed cavity the Q_0 value appears to be strongly dependent on the electrical conductivity (Table C.1 in appendix C) and in good agreement with calculations. The lower the conductivity the lower is the Q . However, parametric analyses also suggest that for electrical conductivities between 100,000 S/m and 10,000,000 S/m there is no visible difference in terms of Q_L . The electrical conductivity for the different materials used at room temperature and at 6 K is given in Table 5.1. As is also visible from Fig.s C.5 and C.6, the influence of electrical conductivity, i.e. of different materials, on the frequency spectrum is rather small – in the range of 10-30 MHz. Further, there is no considerable difference of the Q value between copper and stainless steel. With regards to the right choice of material the magnetic permeability and machinability are the most relevant parameters. The surface roughness does not significantly affect the resonator characteristics.

The frequency depends on the cavity radius in the order of 10^{-2} mm. The smaller the radius the higher the central resonance frequency. The overall wall thickness does not matter for the Q value, though there is a strong influence of the depth of the iris. The voltage standing wave ratio (VSWR, see appendix A.0.3) changes with iris depth in the mm range – the thicker the iris the lower the VSWR and consequently the higher the loaded Q . Thus the iris depth should be as low as possible. The finally chosen thickness is ~ 1 mm, the error being subject to the machining precision.

Table 5.1: The electrical resistivity and conductivity for copper and stainless steel. R denotes the resistivity, and C_{el} the electrical conductivity at 300 K and 6 K [58]. The electrical conductivity for brass is higher than for copper and lower than for stainless steel. The exact value depends on the fraction of zinc in the alloy with copper.

Material	R^{300K} [$10^{-6}\Omega\text{ m}$]	C_{el}^{300K} [S/m]	R^{6K} [$10^{-6}\Omega\text{ m}$]	C_{el}^{6K} [S/m]
Copper	0.0164	35,710,000	0.0017	584,800,000
Stainless Steel	0.79	1,282,000	0.53	18,870,000

The central frequency is inversely proportional to the total iris size, i.e. increasing with smaller iris cross section. In the same way the frequency is related to the cavity radius. Thus if the iris is required to be enlarged to obtain a broader resonance through over-coupling, the radius has to be decreased.

Polarizations of the field modes, i.e. splitting up of the mode resonances, can appear under certain conditions depending on the coupling port to the cavity and appear as two separate resonances from the same mode. To simulate possible experimental consequences a slightly elliptical cavity was assumed (about 3%), a very high electrical conductivity and small iris size to produce a high loaded Q. With these parameters potentially present polarizations of propagating field mode in the cavity should be visible on the frequency spectrum.

After every change in dimensions it is essential to check for the correct field mode. The model should be solved for a wide enough frequency range – as displayed in comparison to a measurement in Fig. 5.17. This allows to control which other resonances except the desired one are present and at which frequencies. It is a rule of thumb that other resonating modes should be at least at a distance of 500 MHz away in order not to interfere and cause any cross talk or overlay to the required field mode. More illustrations of the simulation results can be found in appendix C.

5.3 Building the Cavity

The measurements of the hyperfine structure of $\bar{p}^3\text{He}^+$ required two new microwave targets - one with an eigenresonance at about 11 GHz and one

Table 5.2: This is a summary of the central frequencies and dimensions for the 11 GHz, the 13 GHz and the 16 GHz microwave targets.

Frequency[GHz]	Radius[mm]	Length[mm]	Iris _{area} [mm]	Iris _{depth} [mm]
11.14	16.19	26.16	8 x 7	0.9-0.65
16.12	8.97	22.44	7 x 6	0.9-0.65
12.91	14.5	24.6	10 x 9.5	1.0

at about 16 GHz. It was further intended to complete a measurement series to study density effects and collisional rates with $\bar{p}^4\text{He}^+$. For this purpose another cavity at 13 GHz needed to be constructed which would also fit into the new cryogenic setup. In contrast to the previous cavity for the experiment with antiprotonic ^4He which was built by an external company, the three new cavities were completely designed, simulated, built and tested at SMI⁴. This allowed to adjust the targets to the actual requirements not only of the measurement but also of the setup. Once the microwave cavity parameters are simulated, a prototype is built and thoroughly tested. It is a stepwise process alternating between measurements to assess the correct characteristics and varying the hardware dimensions as well as optimizing the setup with regards to a fast cool-down time and hermetic sealing of the target while keeping the resonance parameters unaffected. In Fig. 5.6 the final versions of the three microwave cavities are presented. The final fixed parameters of the targets can be found in Table 5.2.

One needs to take into account the contraction of the material caused by the temperature change during cooldown. The setup has to be tested in both conditions, at room temperature and at 6 K, in order to determine the temperature dependent changes of the cavity characteristics and adopt to them. With the thermal expansion coefficient $\alpha = 13 \times 10^{-6} K^{-1}$ at 20°C the length contraction for the temperature difference of $dT = 287$ K is

$$dL_{\text{tot}} = \alpha L_0 dT. \quad (5.9)$$

This results in a shift towards higher frequencies. For the 11 GHz target the material contraction is 0.05 mm for a frequency shift of about 40 MHz

⁴Stefan Meyer Institute for Subatomic Physics, Academy of Sciences, Vienna, Austria

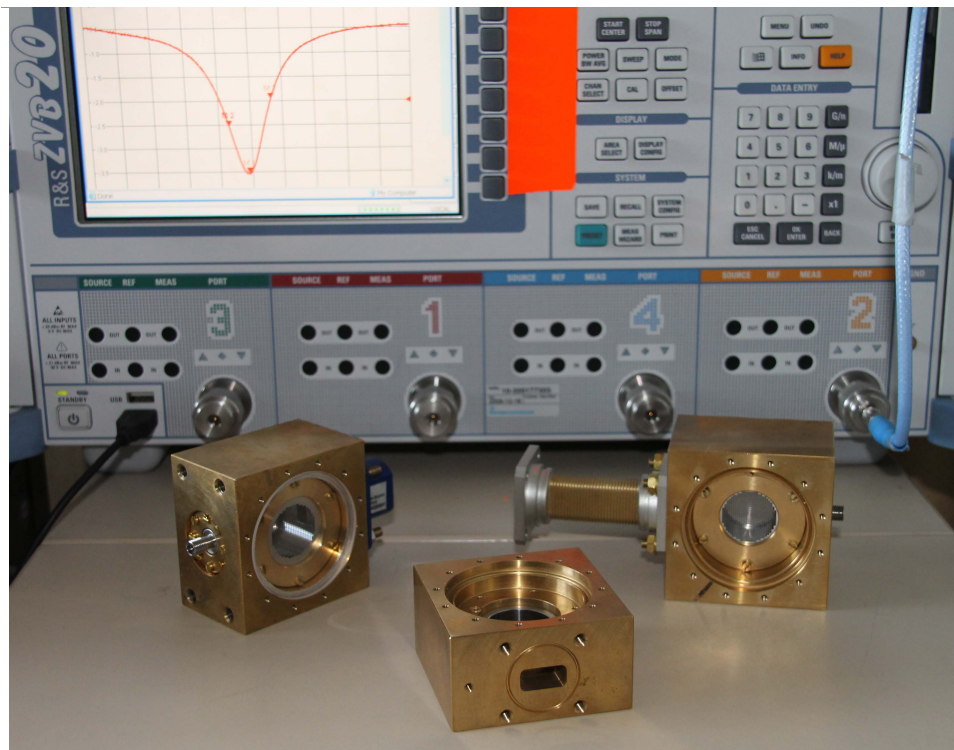


Figure 5.6: The three microwave cavities (at 11 GHz, 16 GHz and 13 GHz) in their final version. The device in the background is the vector network analyzer (VNA) which was used to test the cavities and as a signal synthesizer during the measurements.

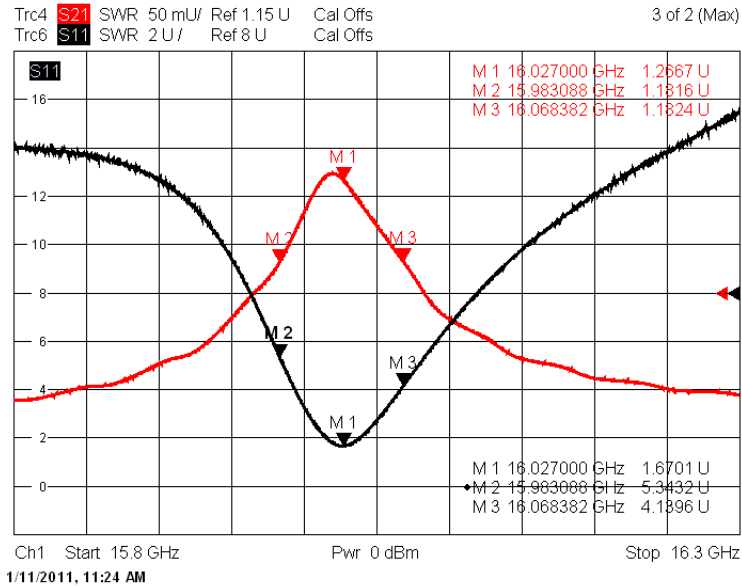


Figure 5.7: The reflected and transmitted signal for the 16 GHz cavity with vacuum pumps and compressor switched off.

between room temperature and 6 K. Calculations and tests regarding conductivity, magnetizability and machinability suggest stainless steel (316L) as the optimal choice – in comparison to copper and brass. Nonetheless, stainless steel has a too low thermal conductivity for this setup. The used cryocooler with a power of 1.5 W was not sufficient to cool the stainless steel target down to 6 K. Copper is too soft for precise machining. Therefore the compromise reached for the first version of the target was brass. The second improved type consists of a stainless steel cylindrical tube which is placed inside the target cell (see Fig. 5.1). This allows to adopt the cavity dimensions more easily and precisely without re-machining the complete target. The outer containment is built of brass which was still the best combination of machinability and thermal conductivity and further completely non-magnetic. More technical details on the cryogenic target can be found in [10].

One problem that needs to be considered with regards to the microwave setup are microphonics⁵. These vibrations due to the compressor cooling

⁵Microphonics is the phenomenon where components in electronic devices transform mechanical vibrations into an undesired electrical signal.

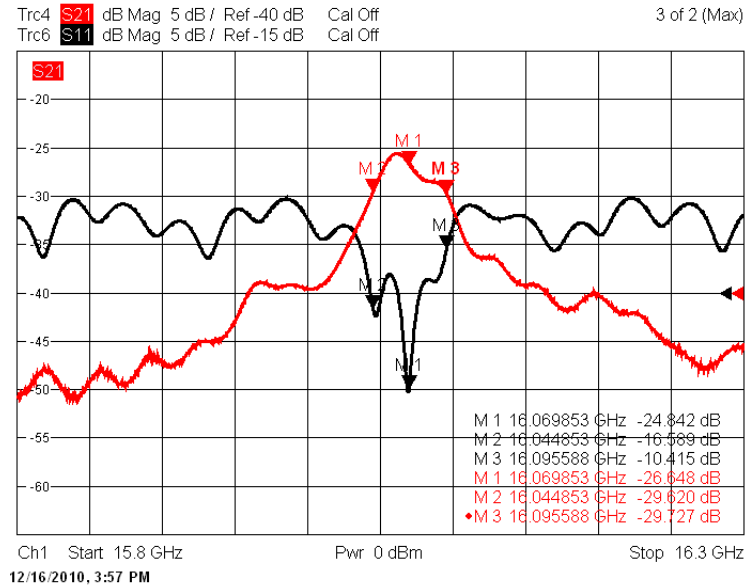


Figure 5.8: The reflected and transmitted signal for the 16 GHz cavity with vacuum pumps and compressor switched on.

or from vacuum pumps are the most likely source of standing waves which were noted to superimpose on the actual resonance signal – as illustrated in Fig.s 5.7 and 5.8. It was noticed that they are significantly stronger if the complete system is evacuated and cooled in contrast to room temperature. These vibrations were more strongly visible for the 16 GHz target than for the 11 GHz one. They can, however, be overcome relatively well by a simple power correction algorithm (read Ch. 5.5 and 5.6) – a Labview-controlled process repeated before every antiproton pulse.

However, the thin meshes screwed to the sides of the microwave target also appeared to be affected by these vibrations resulting in distortion of the resonance signal due to the change in length of the cylinder in an undefined way. For the first measurements very fine meshes with a thickness of 0.05 mm were used. They were produced by techniques of photo-etching 0.05 mm copper foils. As pointed out above, measurements proved that they were very sensitive due to the thin, soft material and thus causing unwanted influence on the frequency spectrum depending as well on the strength of screwing and the pressure exerted on them. This can be simply tested by slightly pressing a finger on the mesh and observe the shifts in frequency



Figure 5.9: A photo of the stainless steel meshes used to confine the microwaves in the cavity. The two meshes are mounted to the cavity with six non-magnetic screws (as indicated by the six holes visible).

and changes in signal height. In the second year new meshes were applied, with a thickness of 0.25 mm (stainless steel (316L), transmissibility $>90\%$, wire thickness 0.05 mm, wire clearance 0.75 mm, made by electric discharge machining) [10].

5.3.1 Pin Antenna, Iris & Waveguides – Coupling to and from the Cavity

The antenna is an important means to monitor the microwave power inside the cavity. Determining the correct shape, length and position is essential to ensure that the antenna can reach the right mode and measure its electric field. Two antenna types were finally implemented for tests – a straight pin of 2 mm length inside the cavity and a pin of 3 mm but bent at the end by about 45° . The power should be measured where the electric field inside the target is strongest. Therefore the optimum choice for the antenna type depended on the orientation of the field around its position. The signal received by the antenna is highest when the magnetic field is perpendicular to it. For the TM_{110} mode there is no radial electric field at the position of the antenna that could be picked up with a straight pin. In principle it is preferable to have under-critical (weak) coupling – about 10% – at the output. Due to the chosen field mode (see Fig.s 5.2 and 5.3) the bent

antenna version was implemented. Measurements were done for different lengths of the antenna pin (between 1 mm and 8 mm) also to investigate the distortion of the field inside the resonator.

Besides the antenna the second sensitive interaction point in the microwave setup is the coupling between the waveguide system and the cavity – the iris (see Fig.5.1). It was already explained earlier in this chapter that the central frequency strongly depends on its size and depth – in principle the resonance gets broader with increasing iris size. The transmission line connected to the iris is a system of several waveguide pieces of different length, shape and material. In particular the several necessary connections between different single pieces of waveguide may potentially lead to considerable signal loss and undesired reflections if they do not fit perfectly together. Rigid waveguides are the easiest type to handle. By reason of practical advantages within the new setup mainly flexible waveguides were used.

5.4 Testing the Cavity Characteristics

The cavities built according to the parameters assessed through simulations and calculations had then to be calibrated and tested. To check the important characteristics of the cavities we used a VNA which served primarily as a microwave signal synthesizer during the experiment. For simple studies of the cavity characteristics it is connected to the VNA via SMA cables – one which sends an RF signal from the VNA port to the input of the cavity (through an SMA-to-waveguide connector), the other one to pick up the transmitted signal and send it back to another port using an SMA feed-through. Figure 5.10 shows the reflection and transmission signal of the 11 GHz target as present during measurement.

5.4.1 Perturbation Measurements

The correct mode for the electro-magnetic field inside the cavity – in our case the TM_{110} mode (see Fig. 5.12) – is decisive for a successful measurement. The first target for the 11 GHz transitions was not systematically measured with regards to the desired field mode and we relied on the accurate calculations and simulations. Due to time limits several tests could not be finished before the first measurement run which thus led to a sequence

of serious problems during the first data taking period in 2009.

Cavity modes can be thought of as resonances between two planes in a waveguide. In the case of a pillbox cavity this is a piece of circular waveguide with a boundary condition at each end, so the solutions are standing waves of the TE and TM circular waveguide modes with an integer number of half-wavelengths between the end plates. The most obvious and straightforward approach to test the modes present in a resonator is a mode chart (Fig. 5.11). In case of a circular resonator the field mode and central wavelength – which are chosen based on the experimental requirements – are controlled by the appropriate values for radius a and length d of the cavity. To do this one can use a mode chart. The x and y axis of the chart are defined through the following relations:

$$\begin{aligned}\lambda_0 &= \frac{2a}{\sqrt{y}} \\ d &= \frac{2a}{\sqrt{x}}.\end{aligned}\quad (5.10)$$

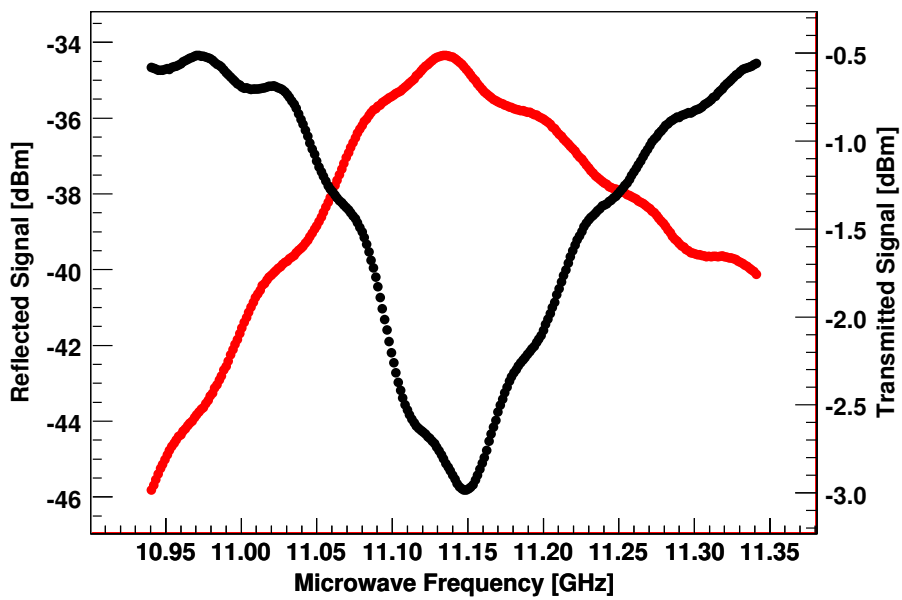


Figure 5.10: The picture on top shows the reflection (black) and the transmission (red) signal recorded with a VNA for the final version of the 11 GHz target at a temperature of 6 K, with the whole setup, including a calibration of SMA cables.

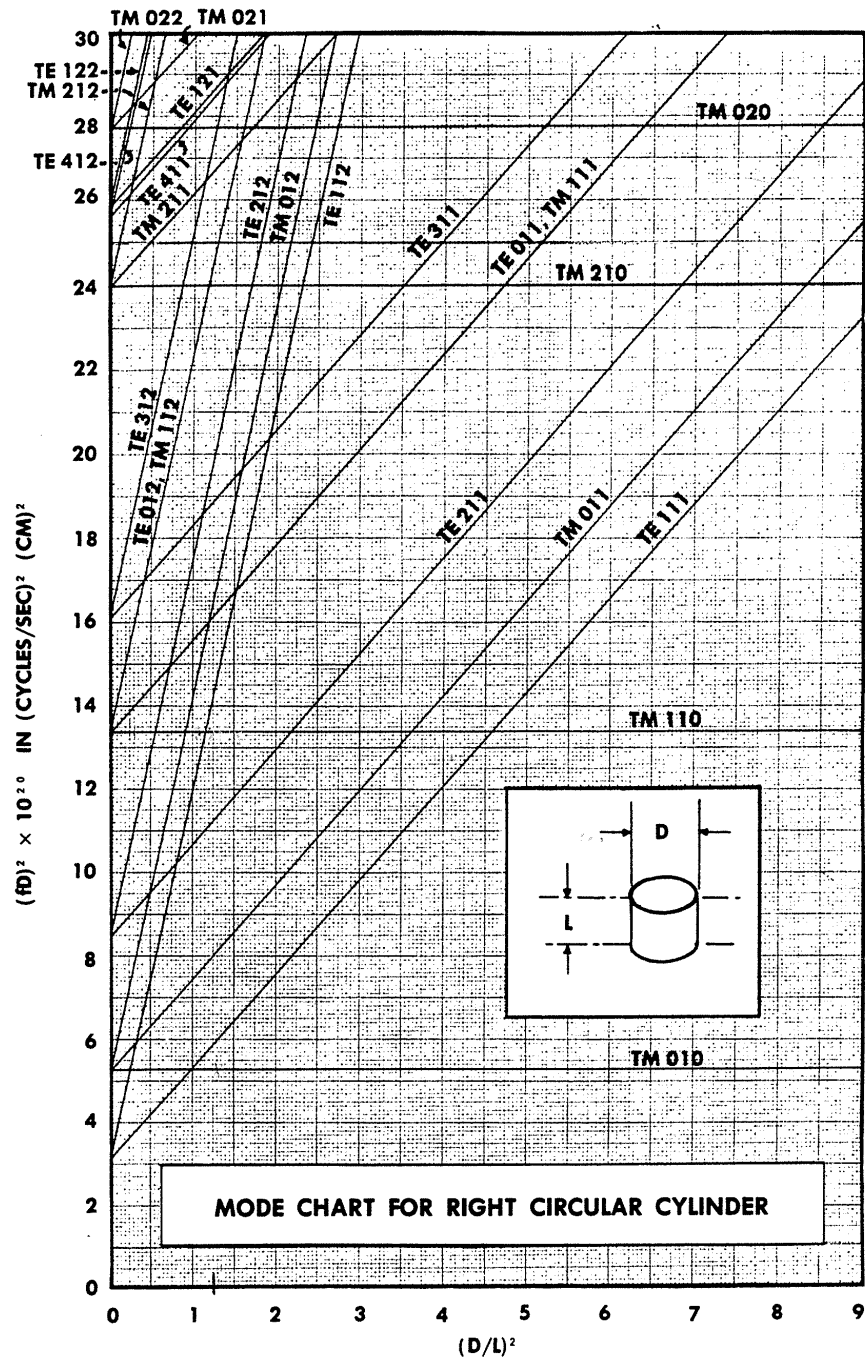


Figure 5.11: A mode chart is used to determine which modes may be present – here in a cylindrical – resonator of defined dimensions [59].

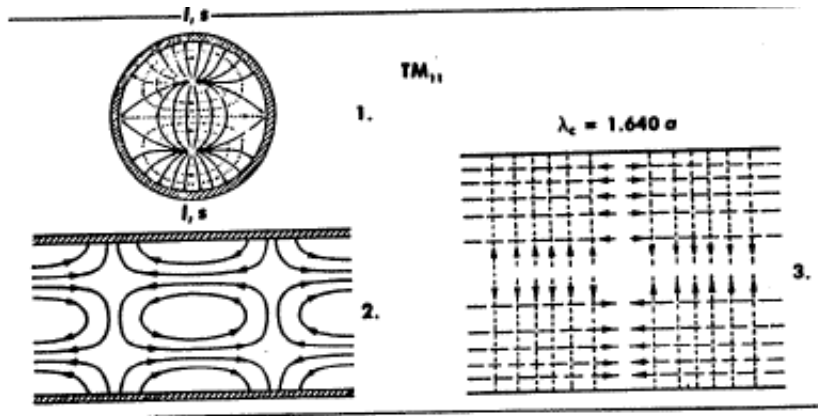


Figure 5.12: This represents the theoretical field distribution in a cylindrical cavity for the TM_{110} field mode – the cross-sectional view (1), the longitudinal view through plane l-l (2) and the surface view from s-s (3). The continuous lines denote the electric field lines, the dotted lines indicate the magnetic field lines and the dashed lines refer to the current [59].

Here λ_0 denotes the central wavelength. The principle is to select on the chart the line corresponding to the desired mode, chose a point on this line which is sufficiently far from all other mode (lines) and read out the x and y value for that point. If the resonator dimensions are already obtained through a simulation this process can be simply reversed. Thus, the mode chart provides a cross-check if the correct field mode is propagating for the defined parameters and if any other modes are lying too close. The according calculated results for the 11 GHz target are presented in Table 5.3. These considerations assume an uncoupled cavity. Therefore the information can be only compared to simulations of the eigenmode solution and finally the dimensions of the actual resonator need to be optimized for a coupled cavity.

Perturbation tests are a complex process and require an expert knowledge of all the tricks to consider for the measurements and to interpret the results correctly. The resonance of modes inside the cavity is very sensitive to the size and thickness of the iris through which the signal enters. The coupling can cause reflections which lead to distortion of the field inside. Also the dimensions can be wrong and the mode might not be able to propagate in

Table 5.3: These are the TM and TE field modes for the 11 GHz cavity, their calculated cutoff frequency (Eq. 5.11) and resonance frequency in the – uncoupled – cavity with a radius of 16.19 mm and a length of 26.16 mm. If the desired TM_{110} mode is too close to other field modes it can be affected through cross talk or the microwave power sent in sustains the wrong mode.

Field Mode	P_{nm}	Cutoff Frequency $\nu_{c,nm}$	Resonance Frequency f_{nml}
TM 110	3.832	11.2932	11.2932
TM 011	2.405	7.0877	9.1142
TM 012	2.405	7.0877	13.4746
TM 112	3.832	11.2932	16.0893
TM 010	2.405	7.0877	7.0877
TM 210	5.135	15.1333	15.1333
TM 111	3.832	11.2932	12.6637
TE 111	1.841	5.4555	7.8911
TE 211	3.054	9.0004	10.6695
TE 011	3.832	11.2932	12.6637
TE 112	1.841	5.4555	12.6794
TE 212	3.054	9.0004	14.5718
TE 012	3.832	11.2932	16.0893

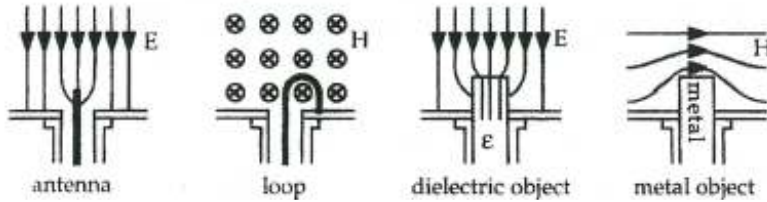


Figure 5.13: These pictures compare the influence of a straight pin antenna, a loop antenna, a dielectric and a piece of metal within when inserted in an electric and magnetic field respectively.

the resonator.

Perturbation via Bead Pull – A Common Method Information about the field distribution and mode orientation can be obtained by observing the coupling of perturbing objects to E and H field components at various places in the cavity. This can in principle be done using E field antennas, H field loops or by introducing perturbing objects of dielectric, ferrite or metal as demonstrated in Fig. 5.13. Introduction of a dielectric object in a region of electric field produces a negative shift in the resonant frequency while introducing a metal object into a region of magnetic field causes a positive frequency shift. If both fields are present when a metal object is inserted, the resulting frequency shift will depend on the relative strengths of the E and H fields. Small objects pulled through the cavity on a string can be used to map the field distributions of the modes. The change in resonant frequency upon introducing an object into the cavity field is proportional to the relative change in stored energy.

The general principle of this technique is to run a thread along the central axis through the resonator and to fix a bead on one end. On a VNA one can observe the shift in frequency as the bead is pulled towards the center of the cavity. We applied a variation of this method since for the required high frequency range the cavity dimensions are too small and make it very difficult to implement this solution and extract useful data from the tests.

Perturbation Measurements – A Straightforward Approach As pointed out above, the basic idea how to investigate the field distribution in the target is via perturbation of the field. A perturbing body has to be inserted into the target which itself is closed towards the outside. One

attempt was to mount a rigid stainless steel plate instead of one of the stainless steel meshes with a small hole in the middle from which a lever (white plastic) reached towards the center of the cylinder (see Fig. 5.14). At the centered end of the lever was fixed a small ceramical or brass sphere (s13N4, Pompel). To change the position of lever and sphere it was connected to a small, computer-controlled (PI micromove) step motor outside the cavity. Step sizes between 22.5° and 45° were used to scan the field in the target. The measurements were performed with levers of different length (\leq radius) and spheres of several diameter between 0.5 mm and 4 mm.

Measurements and discussions (with experts in the field of radio frequency structures) lead to the conclusion that a simpler approach is preferable to extract unambiguous information on the field modes from the measured frequency spectra.

Therefore the dielectric is simply replaced by a nylon thread. A piece of rigid and thin enough fishing line is inserted into the cavity through one of the meshes. At first one should have a look at the frequency spectrum at large range (5-15 GHz, see Fig. 5.17) before looking at the single field modes. The range should for convenience be changed to see only one resonance at a time. It is more useful to look at the transmission spectrum S21. There are several steps one can follow in order to check a perturbation of the field. With the VNA the measurement can be saved and a second one directly overlayed. Thus it is possible to compare the original frequency spectrum to the one after perturbing the field with the thin nylon thread, understand if and where the field is perturbed and note possible frequency shifts. The thread can only induce electric field changes. So if no change is visible at a certain point in the cavity, no electric field is present. This process was repeated at several different, strategically chosen points inside the volume which can give a hint on the present mode. Every mode corresponds to a certain distribution of the electro-magnetic field in the resonator. To distinguish between TE and TM modes in the first place it is sufficient to check thoroughly for any distortion by the inserted fishing line. If no effect is observable at any point, then the field distribution will most likely be a TE mode and thus does not need to be further considered. For any TM mode one can investigate the change of field strength from the center towards the outside of the circular resonator. Combining these results with the information from the theoretical field distributions (refer to Fig. 5.12)

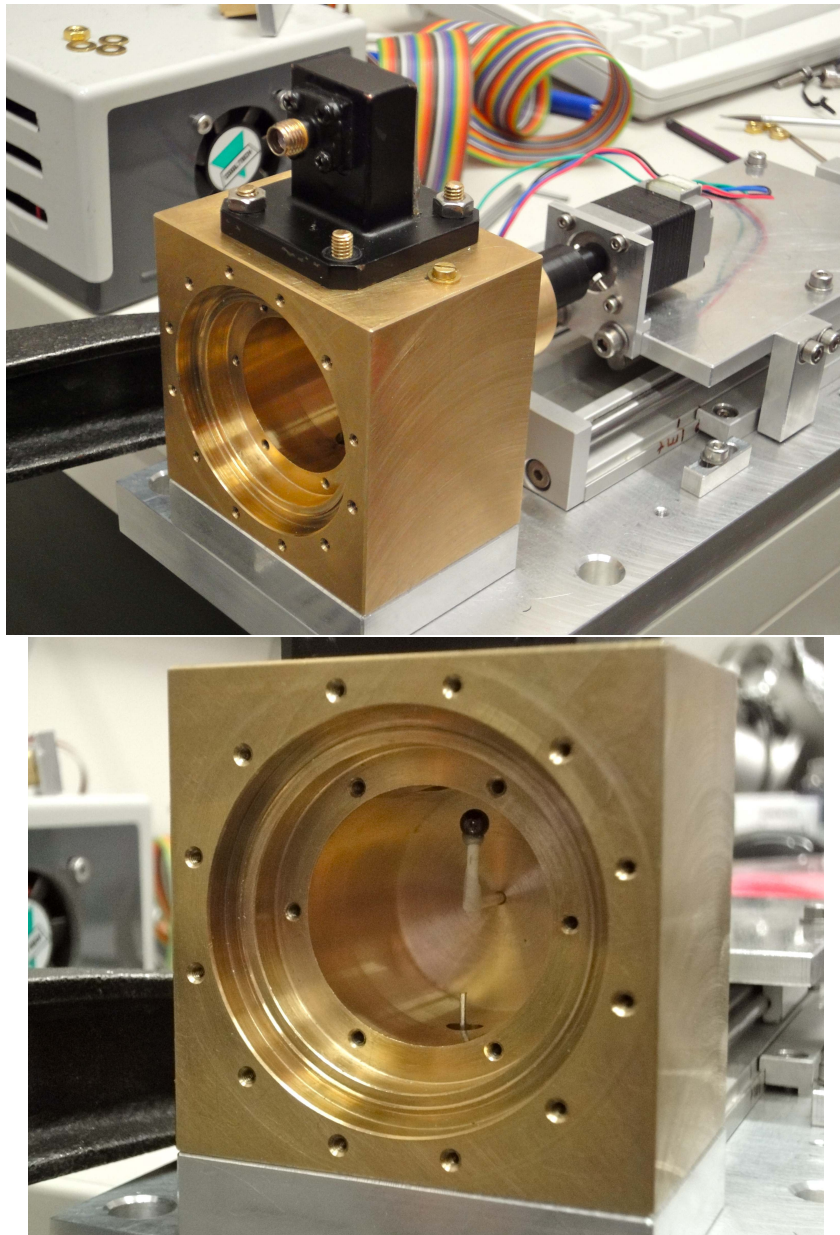


Figure 5.14: These two pictures display the 11 GHz cavity and the setup as used to perform the first perturbation measurements.

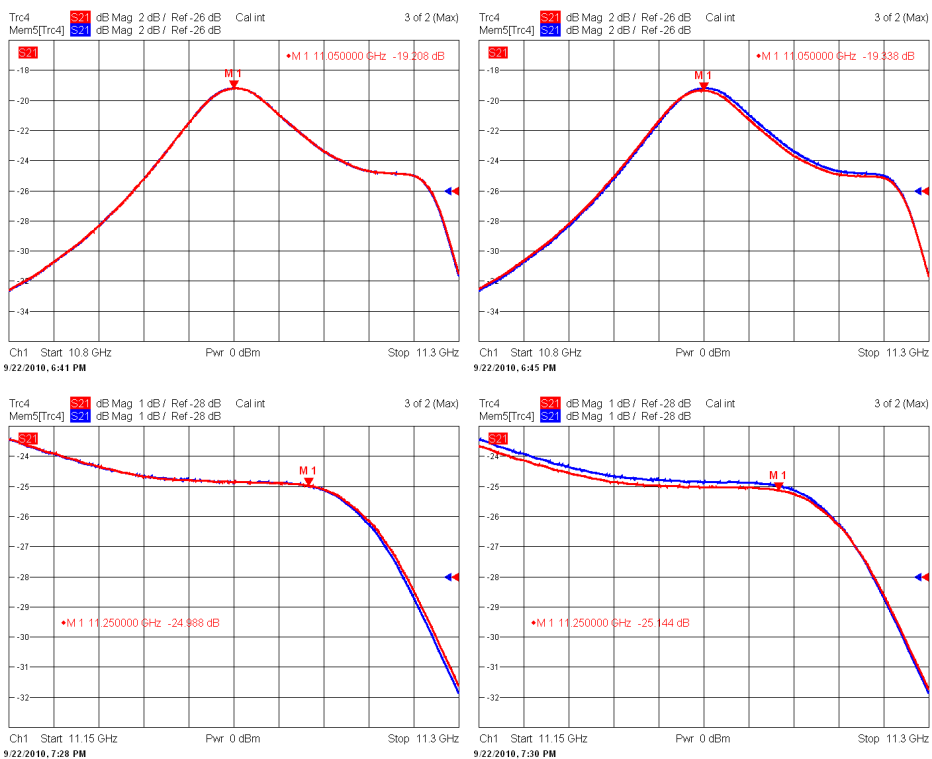


Figure 5.15: The perturbation test results for the first 11 GHz resonator. The resonance of two different modes – on top the graphs for the TM_{110} mode and below for the TM_{012} mode – as could be verified via perturbation. The pictures on the left illustrate the situation where the nylon thread was inserted in the center of the cavity, the ones on the right refer to inserting the thread very close to the cavity wall. The blue lines indicate the original shape of the resonance and the red lines the distorted spectrum.

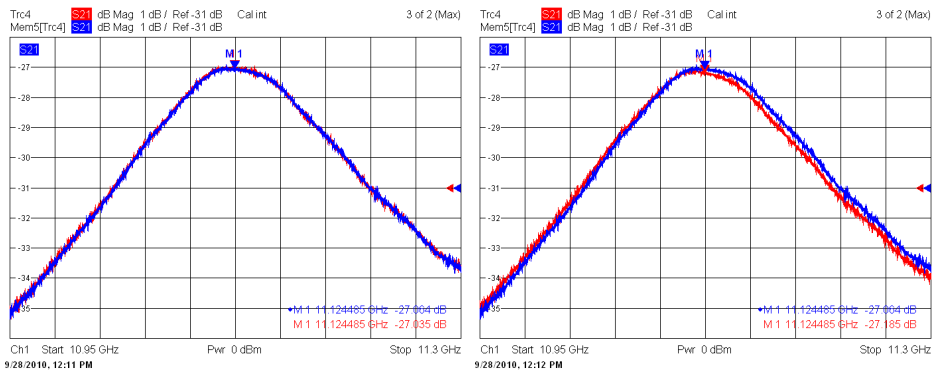


Figure 5.16: The perturbation test results for the new 11 GHz resonator. As can be seen also from Fig. 5.17, the TM_{110} mode is now so far apart from neighboring modes that only the mentioned mode is presented here. The red lines indicate the original shape of the resonance and the blue lines the distorted spectrum.

allows to identify a particular field mode.

Additionally one has to check on a mode chart (see Fig. 5.11) at which frequency the suspected field mode should appear for the given dimensions of the resonator and if in the present case the particular mode would resonate inside the cavity at all. This can be determined through the cutoff frequency – the lowest frequency which will resonate in a cavity of defined dimensions – and is given as

$$\omega_c = c \left(\frac{P_{nm}}{r} \right) \quad (5.11)$$

for a circular system. P_{nm} is the first root of the Bessel function $J_0(r)$ and r the radius of the device. For the final 11 GHz and the 13 GHz cavity the desired field mode and eigenresonance frequency could be confirmed. This was not the case for the first 11 GHz cavity. However, the perturbation measurement could illuminate why no positive results were achieved with this cavity. The TM_{110} mode was lying too close – less than 200 MHz apart – to another mode which probably caused severe interference. Figures 5.15 and 5.16 demonstrate the technique and show results of these tests. As shown in the first figure, in the case of the TM_{110} mode the field is only distorted near the wall, i.e. a shift of the spectrum visible, which means that there is electric field present while in the center there is not. The other mode shows effect due to the nylon thread in both positions, i.e. at both

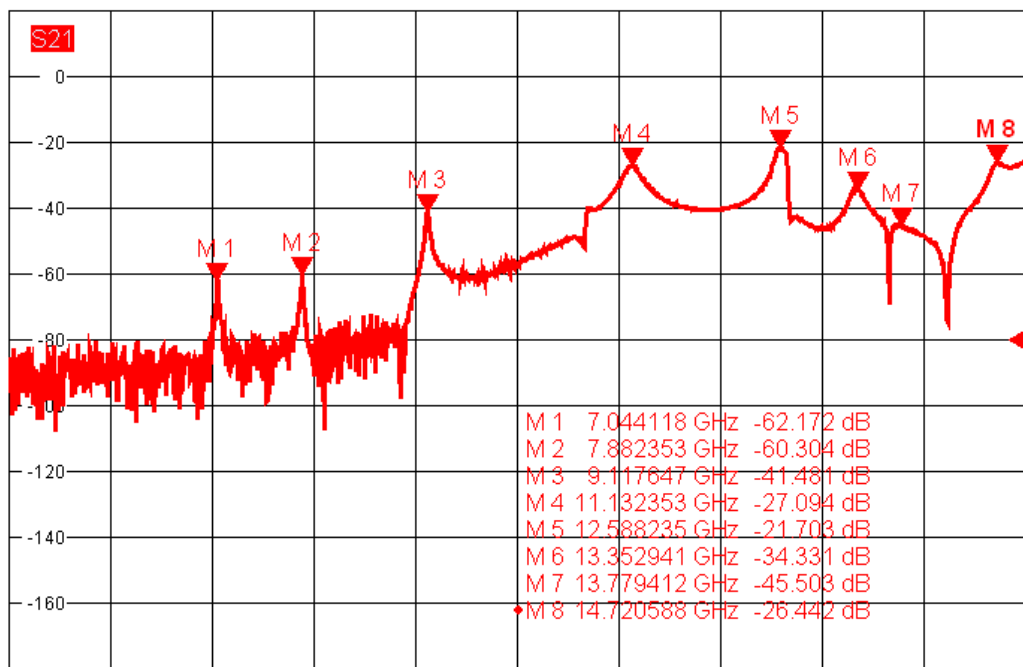


Figure 5.17: The transmission signal for the 11 GHz cavity – a measurement over a wide frequency range to display the different resonating field modes. The TM₁₁₀ mode is at about 11.14 GHz (indicated by marker M4 in the spectrum). The theoretical frequencies of the transitions to be measured are 11.125 GHz and 11.157 GHz.

points an an electric field exists. Repeating the measurement also at more points and combining the information from theoretical field distribution for the modes, a mode chart and these observations one can verify that both these modes are present. Only the TM_{110} is desired. As can be seen from the frequencies given for the marker positions in the plots, the TM_{012} is only 200 MHz away. It was thus interfering with the other mode and distorting the measurement. For the new 11 GHz cavity the TM_{110} mode is now far apart from neighboring modes, as is shown in the second figure.

All perturbation measurements were carried out at room temperature (and air pressure) due to practical reasons. However, the field patterns will not change due to temperature. The resonance frequencies will shift due to the cavity material contraction – as explained earlier – but not their relative distance to each other.

5.5 Starting Point - The Old Measurement Setup

The course of one measurement as applied for the first studies with antiprotonic ${}^3\text{He}$ looked the following. In preparation for the actual measurement it was necessary to assess the frequency points for the frequency scan manually. This meant to define the desired frequency points over a sufficiently broad range around the expected resonance line and adjust the positions of the TST such that a very narrow resonance built up at each frequency. The stub positions with the corresponding frequencies were recorded. The TST settings and other relevant parameters were entered in a text file to be read during the experiment and hence reproduce the same resonance in the microwave cavity. At this point two working modes have to be distinguished – diagnostic mode and operational mode. Schematic diagrams of the experimental setup in the two different modes can be found in Fig. 5.18.

5.5.1 Diagnostic Mode

This mode was used to prepare the settings for the desired frequency points and during experiment – between two antiproton pulses – to verify that the sharp resonances are reproducible for the respective settings of the triple-stub-tuner. Changing between this mode and the operation mode requires to implement a waveguide switch, a device that can be remotely controlled

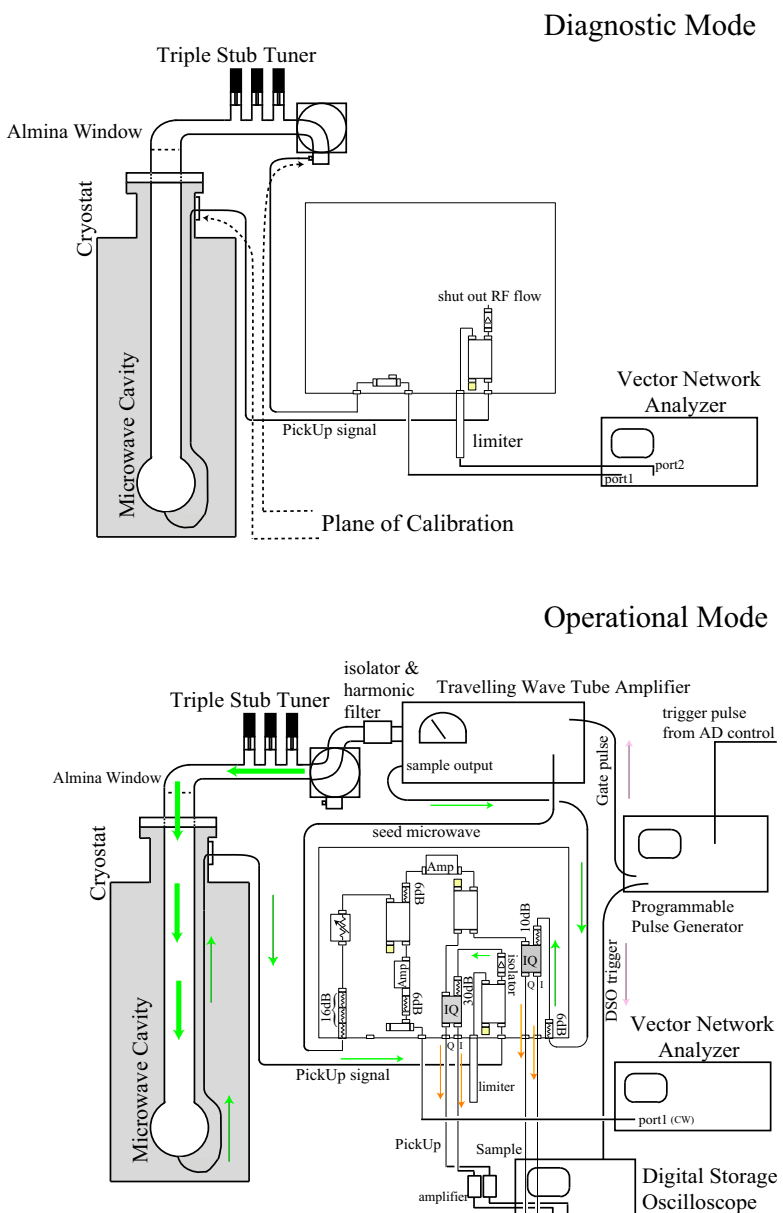


Figure 5.18: A schematic drawing of the two different work modes of the old microwave setup. Above is the diagnostic mode which is used to calculate the correct power in the cavity and the required input. This is followed by the operating mode, displayed below, during which the actual data acquisition takes place.

to change the routing of the input signal [53]. This switch is in closed position for the diagnostics. A set of parameters is read in. The VNA is in frequency sweep mode. The signal (which is not traveling through the TWTA but directly across the waveguide switch to the target) is transmitted through the cavity and sent back to the VNA to confirm the presence of the resonance (see Fig. 5.18 for reference). The total required input power can be calculated from the return loss which itself is obtained through the reflected signal and the transmitted signal going back to the VNA. Port 1 of the network analyzer produces a 0 dBm output signal for a defined frequency point. Via coaxial cables (Huber & Suhner Sucoflex 104) which have to be appropriately calibrated it is transmitted to a directional coupler (ARRA 6-9194-10) and further through a circulator. The circulator is a device with three waveguide connections (P_1 , P_2 and P_3). In diagnostic mode the signal from the VNA is carried through the P_2 and P_3 of the coupler (using an SMA-to-waveguide adapter – PARZICH LD75CA-F) and a waveguide system leading into and through the vacuum chamber to the cavity. Part of the signal will be reflected back to the VNA (at port 1), another part will go through the cavity and be picked up by a small, slightly bent pin antenna to be forwarded via coaxial cables to port 2 of the VNA. P_1 of the circulator is only used in operational mode – to transmit the amplified signal from the TWTA through to P_3 of the device. This route is blocked in reverse direction, nothing can be reflected back through P_1 . If this is performed for the required frequency range (frequency sweep) one can obtain the spectra for the reflected and the transmitted RF signal of both VNA ports [53].

Calculation and Measurement of the Required Microwave Power

The initial microwave input power is read in from a file. Due to power losses in the system only a small fraction will reach the microwave cavity. To determine the power which needs to be sent to the TWTA in order to transmit the right amount to the cavity a compensation algorithm is applied. Once the diagnosis is done, a waveguide switch – a device that can be remotely controlled to change the routing of the input signal [53] – moves to the correct position (open for the measurement, closed for the diagnosis). The data for S11 which should finally be the same over the defined frequency range and number of points are read in. First the transmission loss is assessed

through the relation

$$L_T = -10 \log_{10}(1 - 10^{\frac{L_R}{10}}) \quad (5.12)$$

with L_R denoting the return loss. The pick-up signal relates to the input as

$$P_{PU} = P_{IN} - L_T - C_A \quad (5.13)$$

where C_A is the antenna coupling and P_{IN} the input power. The transition loss has to be determined for every frequency point. To calculate back to the required TWTA input one has to subtract the gain (in dB). Before the amplifier the signal has to pass a voltage-controlled attenuator (GT Microwave Inc. A6L-78N-7) which can adjust the power as required. This attenuator is a device which applies an amplification or attenuation factor to the sent power. It behaves linearly, thus the correct voltage can be derived from the TWTA input through a simple linear equation and during the operational mode this value will be read in from a text file for every frequency point. The smaller the weighted output from the amplifier the bigger the input voltage needs to be. All important parameters are saved to a file and read in during the actual measurement process.

5.5.2 Operational Mode

In the operational mode the VNA is changed to CW output at a defined frequency (and narrow bandwidth). The correct voltage attenuation is applied. The waveguide switch changes to opened position, i.e. the MW proceeds to the TWTA – after the amplifier is shortly warmed up with at least 10 Hz for several ten seconds. The system is now ready for the antiproton pulse to arrive, signalised by the AD trigger. The microwave pulse is triggered (depending on the measurement), the laser fired and finally the data are written to files in ROOT format⁶. In this mode the input pulse is again first split by a directional coupler, then amplified to about 10 dBm by a low noise microwave amplifier (MITEQ AFS4-08001800-35-LN). A hybrid (ARRA 6-9194-90X) splits the signal once more. One part is led to an IQ mixer (MITEQ IR0618L C2Q) and used as local oscillator (LO). The other part is forwarded to the TWTA – with a fixed gain of 81 dBm in the desired frequency range, the maximum power output being 1.5 kW. The voltage-controlled attenuator applies an amplification factor. The amplified output

⁶An object-oriented data analysis framework developed at CERN [60]

is a $20 \mu\text{s}$ long pulse which is triggered by a delay generator (Stanford Research DG535) referenced to the AD trigger. The frequency is determined by the CW signal from the VNA set to a resonant frequency previously selected in the diagnostic mode. To protect the amplifier from potential reflection of the signal, an isolator (Pamtech MHG2011) is mounted directly after the TWTA output. The signal proceeds through a waveguide switch then a circulator which is used only during diagnostic mode and further through a system of rigid and flexible waveguides to the microwave cavity. The pick-up antenna transmits back the signal that arrives in the cavity – again across a signal splitter and an IQ mixer. Thus a DC signal proportional to the in-phase I and the quadrature Q component of the input signal relative to the local oscillator reference is created. For the picked-up signal the reference is the split part of the original input from the VNA. An analog procedure happens for the sample output signal from the TWTA at another IQ mixer. The in-phase voltage (V_I) and the quadrature voltage (V_Q) are calculated from the multiplication of the input voltage (V_{IN}) with the local oscillator input voltage V_{LO} as

$$V_I = \sqrt{V_{LO}V_{IN}} \sin(\phi)$$

$$V_Q = \sqrt{V_{LO}V_{IN}} \cos(\phi). \quad (5.14)$$

The parameter ϕ denotes the phase difference between the inputs.

When the program is ready it starts again with the diagnostic mode for the next frequency step and waits for the next AD trigger.

5.6 The New Measurement Setup

In the first measurement with the new setup and the 11 GHz cavity was still the original method with TST and two modes applied. However, if the power required in the cavity is not too high, one can have a low cavity Q and thus a broad cavity resonance. If it is sufficiently broad, all the frequency points will lie within the bandwidth of the cavity. Therefore no frequency tuning will be needed and the TST can be omitted. The new targets were all produced to obtain a broad enough resonance when coupled to the outside. The overall idea was to use the tuners only to optimize the present resonance and keep them at one fixed position for the entire experiment rather than finding the optimum position of the TST for every single frequency step. To nevertheless

achieve an equal power over the whole frequency range of interest we applied a simple correction. As for the old setup, the input power was adjusted for every measurement point to compensate the signal loss in the system as well as the frequency dependence of the power in the cavity and finally obtain the right, equal-leveled power in the cavity over the entire measured frequency range. Finally the following procedure was implemented. From the power output picked up by the antenna and measured with the DSO the energy in the cavity was calculated. This value was compared to the microwave power expected to be transmitted to the cavity. This difference was simply added to the initial input power. The power fluctuation could be reduced, however not fully eliminated (see Ch. 8). This power correction was done online in between two antiproton shots.

After the first year the microwave setup was drastically simplified in order to reduce error sources. The diagnostic mode was adopted in the setup for $\bar{p}^3\text{He}^+$ so that waveguide switch, circulator and TST became obsolete. Further the IQ mixer technique was replaced by a simpler version using diodes. Schematic drawings of the new microwave setup are shown in Fig.s 5.19 and 5.20, for cavity diagnostics and calibration and for the measurement. The frequency was synthesized by the VNA and sent to the amplifier. The signal thus amplified by about 81 dB – slightly different depending on the frequency range – proceeds then two different ways. The sample port of the TWTA attenuates the amplified signal again by 51 dB. Via SMA cable the signal is forwarded to a diode and passed on via BNC cable to the digital oscilloscope. The other way leads unattenuated through a waveguide system of about 1.5 m length to the cavity. Finally the signal picked up by the antenna travels via (cryogenic) SMA cable to a diode and further via BNC to the DSO where it is recorded. Ideally, if all attenuation is accounted for correctly, the two signals should be equal. The diodes are coaxial detectors (8474B Agilent GaAs diodes) specifically designed for application in the microwave range. They convert the received power (dBm) to a voltage which is forwarded to the DSO. Two diodes are implemented in the setup – one for the picked up signal from the antenna and one for the sample output of the amplifier (which is used as cross-check for the power output from the TWTA). They need to be power calibrated to assure reliable information on the power in the system (see Sec. 5.7).

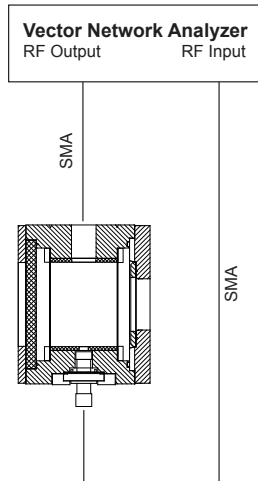


Figure 5.19: A schematic drawing of the new microwave setup as used to test the cavity characteristics.

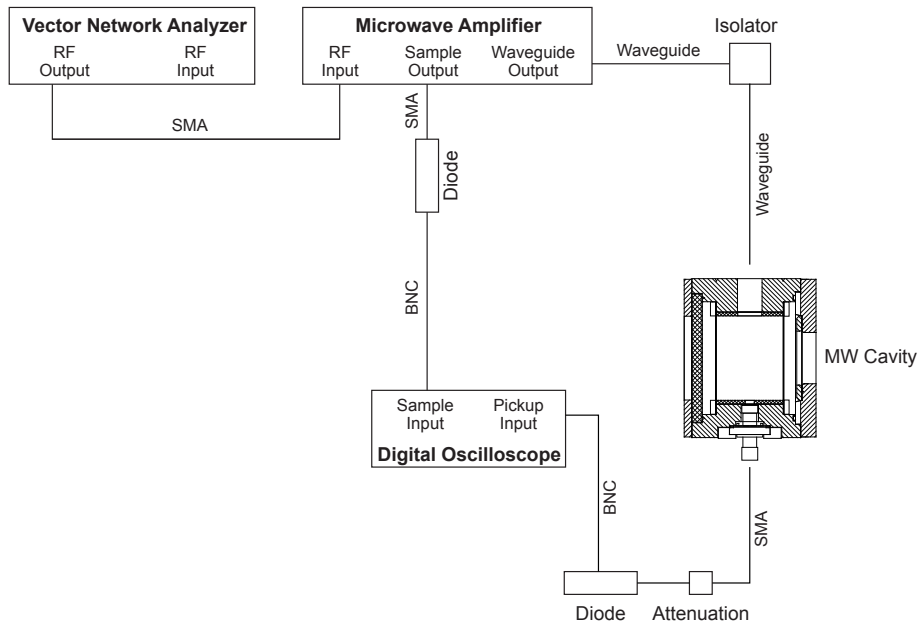


Figure 5.20: A schematic drawing of the new microwave setup as used during the actual data acquisition.

5.7 Calibration

Calibration is another crucial part in preparing the microwave setup for the experiment – to eliminate reflections and other unwanted effects through imperfect electronic components.

Power Calibration of the Diodes The dynamic power range of the diode should be broad enough to enable a measurement without changing the setup in between. Adding appropriate radio frequency attenuation at the input allows to adjust the range as required for the microwave powers sent into the cavity. The dynamic range of the diodes is between -22 dBm and +8 dBm. A sufficient minimum voltage – about 10 mV – is necessary because of the limited DSO resolution to ensure that the diode output transmitted to the DSO is above its noise level. In order to perform a reliable correction for power losses in the system a power calibration for the diodes was essential. For the calibration the diodes were connected to the VNA output port and through a BNC cable the signal was forwarded to the DSO and read out. The calibration curves are displayed in Fig. 5.21.

Power Calibration of the TWTA The amplifier was then calibrated by means of the calibrated diodes. Therefore a signal was sent from the VNA to the amplifier via SMA cable and – as during the experiment – the sample output was recorded. Figure 5.22 shows the calibration curves calculated from the sample port output. The curves were fitted with a fifth order polynomial and a simple linear fit function. These measurements were done at the central frequencies of all three microwave cavities. To cross-check for potential frequency dependencies the calibration was repeated at several other frequency points, but with no significant deviation within the measured range. To further ensure a smooth operation and a stable power output without spikes, the TWTA requires sufficiently long warm-up phases before every beamtime shift and also in between two antiproton pulses and during every measurement break.

5.7.1 Power Calibration of the Cavities

Another tricky part when preparing the experiment is the calibration of the cavity. This is required for a reliable conclusion to the actual energy contained in the cavity. The best way to do that is to combine simulation

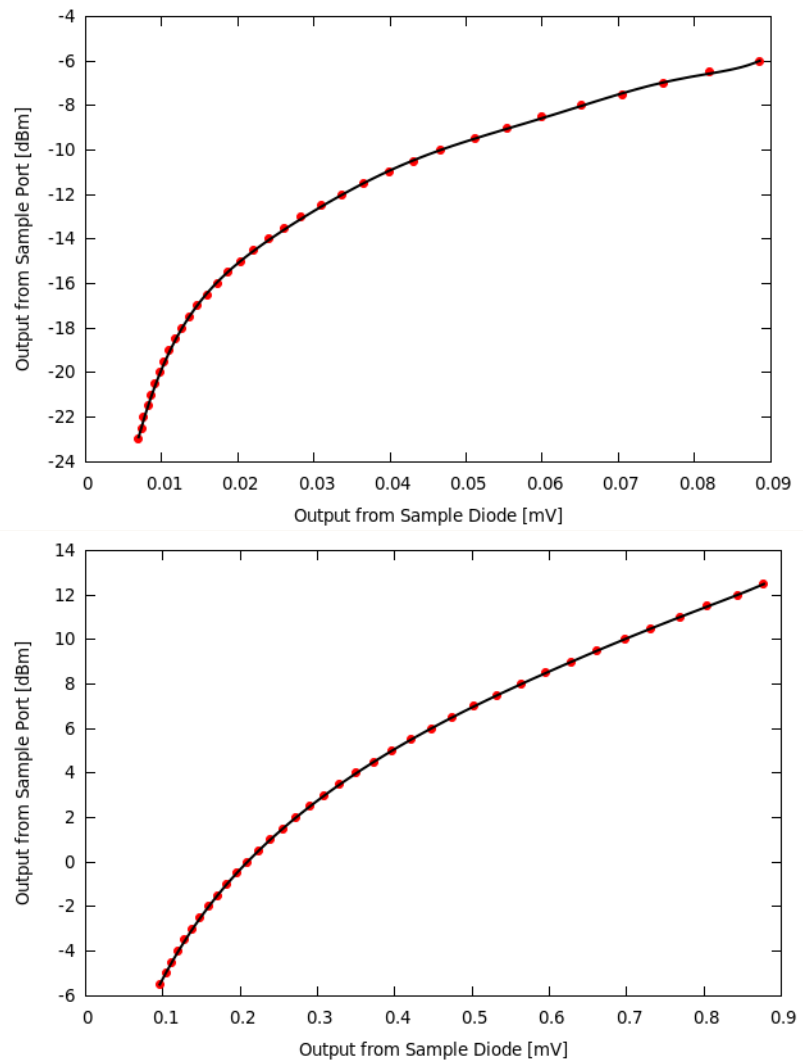


Figure 5.21: These are the calibration data for the diodes – split in two parts for convenience of fitting with higher order polynomials.

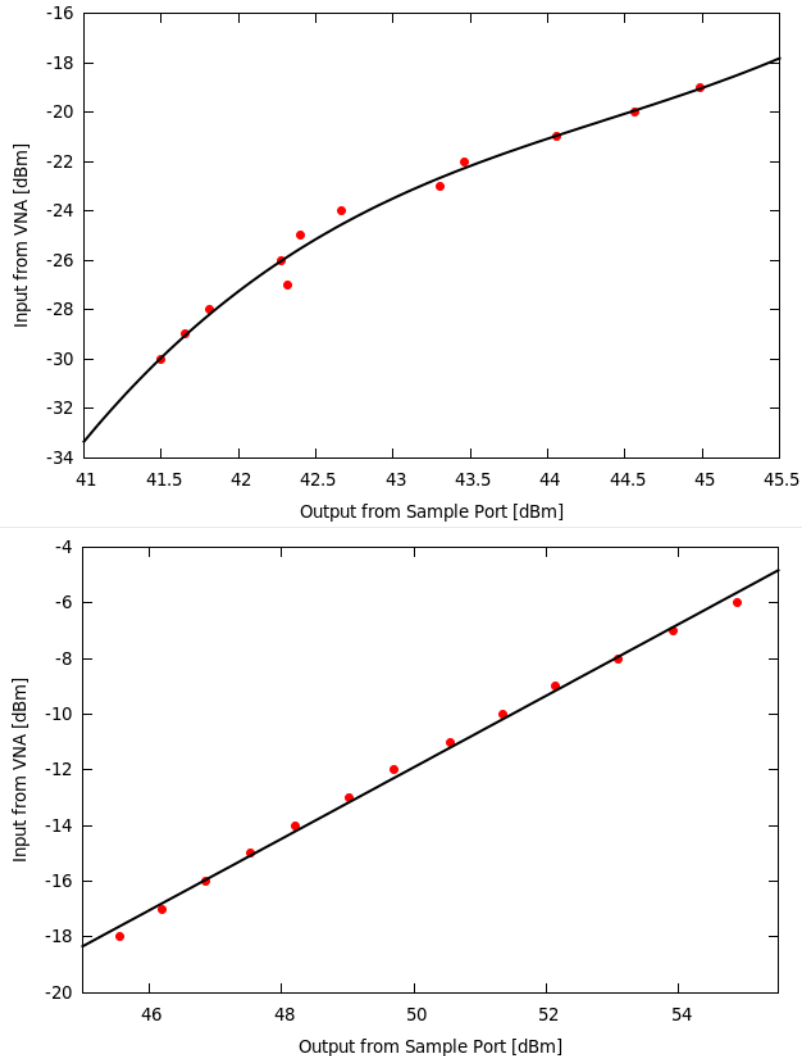


Figure 5.22: These are the power calibration data for the TWTA. From the curves one can determine the input power to the amplifier in order to obtain the desired output power. The output is sent from the attenuated sample port of the TWTA via diode to the DSO. The values given in the x-axis refer to the power directly at the amplifier output, the diode calibration is already applied. The y-axis gives the required output power from the VNA after taking into account the present losses and attenuation. For convenience the fitting is split in two parts.

and measurement. Based on the same simulation model described in Ch. 5.2 the following three quantities can be calculated:

$$\hat{U} = \int I dz. \quad (5.15)$$

is the energy inside the target. The current I is integrated along the resonator axis z . The losses in the cavity are defined through the integral over the resonator walls

$$P \sim \rho \bullet \oint H^2 dF \quad (5.16)$$

where $\rho = \frac{1}{2\sigma\delta_s}$ with the electrical resistivity σ and the skin depth δ_s . The stored energy is

$$E \sim \mu_0 \bullet \oint H^2 dV + \epsilon \int I^2 dV, \quad (5.17)$$

integrating over the cavity volume. For the experimental test one can apply the relations

$$P = \frac{\hat{U}}{2r} \quad (5.18)$$

in case of a circular system with r being the shunt impedance. The Q value depends on the energy as

$$Q = \frac{\omega E}{P} \quad (5.19)$$

and therefore

$$\frac{r}{Q} = \frac{\hat{U}^2}{2\omega E}. \quad (5.20)$$

In practice this means that for a defined power P_{sys} sent into the system one could deduce the power P_{in} actually transmitted inside the resonator from

$$P_{\text{sys}} = P_{\text{in}}(1 - \Gamma^2) \quad (5.21)$$

In this relation $\Gamma = \frac{Z_L - 1}{Z_L + 1}$ denotes the reflection coefficient and Z_L the load impedance. The impedance can be obtained from the Smith chart (appendix A) representation of the frequency spectrum as well as the loaded Q value. With these parameters known, r is calculated from

$$r = \left(\frac{r}{Q_L}\right)Q_L \quad (5.22)$$

The ratio r/Q_L is retrieved through the simulation as represented by Eq. 5.20. Thus U can be calculated:

$$U = \sqrt{2P_{\text{sys}}r}. \quad (5.23)$$

The result is converted to dB and put in relation to the measured power output from the cavity. This gives the value which connects the measured output to the energy actually resonating inside the target – for all three cavities in the order of 50 dBm.

Power in the Cavity To induce exactly an electron spin-flip, a certain microwave power is required (read Ch. 6) – in our case in the range of a few Watt. This may be different for different target densities and laser delays.

The microwave energy E_M resonating in the cavity can be defined as

$$E_M = QP_{\text{loss}} \frac{1}{\omega} \quad (5.24)$$

where P_{loss} is the power loss in the cavity, ω the (angular) microwave frequency. The field along the axis of the resonator is described with $H_z = H_0 \sin(\omega t)$ and H_0 depending on the microwave energy E_M like

$$H_0 = \sqrt{\frac{E_M}{\pi\mu_0 a^2 d J_1'^2(P_{\text{nm}})}} \quad (5.25)$$

The parameter a is the cavity radius and d the length. P_{nm} is a first root of the Bessel function $J_1(x)$. The magnetic field can thus be calculated:

$$B_0 = \sqrt{\frac{\mu_0 Q P_{\text{loss}}}{\pi a^2 d \omega J_1'^2(P_{\text{nm}})}} \quad (5.26)$$

Chapter 6

Numerical Simulations of Transition Processes

Due to the limited measurement time available (4-8 weeks per year) at the Antiproton Decelerator at CERN, it is particularly important to prepare the experiment carefully. Doing accurate simulations of the transition processes before the actual measurement in order to assess and optimize parameters is saving a lot of valuable time. The transition dynamics have been numerically simulated by solving the optical Bloch equations.

6.1 Two-Level Optical Bloch Equations

The two-level optical Bloch equations describe the behavior of a two-state quantum system in the presence of an oscillating magnetic field. These equations can be derived from the time-dependent Schrödinger equation. Using the density matrix representation, this equation can be formulated the following way:

$$\frac{d}{dt} \begin{pmatrix} \rho_p \\ \rho_d \\ \rho_x \\ \rho_y \end{pmatrix} = \begin{pmatrix} -\gamma_{rp} & 0 & 0 & \frac{1}{2}\Omega_m(t) \\ 0 & -\gamma_{rd} & 0 & \frac{1}{2}\Omega_m(t) \\ 0 & 0 & -\gamma_T & -\Delta\omega \\ -\Omega_m(t) & \Omega_m(t) & \Delta\omega & -\gamma_T \end{pmatrix} \begin{pmatrix} \rho_p \\ \rho_d \\ \rho_x \\ \rho_y \end{pmatrix} \quad (6.1)$$

with $m = -34 \rightarrow +34$ for the measured state in antiprotonic ${}^3\text{He}$. ρ_p and ρ_d indicate the probabilities of the quantum system to be in the parent state or in the daughter state, ρ_x and ρ_y give the real and imaginary part of the coherence between the two states. $\Delta\omega$ denotes the difference between the transition frequency $\omega_{ij} = \frac{E_i - E_j}{\hbar}$ and the frequency of the oscillating field.

$\Omega_m(t)$ is the so-called *Rabi frequency*. Depending on the type of field it will be defined as

$$\Omega_m^{el}(t) = \frac{\mu_m^{el} E(t)}{\hbar} \quad (6.2)$$

or

$$\Omega_m^{mag}(t) = \frac{\mu_m^{mag} B(t)}{\hbar} \quad (6.3)$$

Here μ_m^{el} and μ_m^{mag} define the electric and the magnetic transition dipole moment respectively, depending on the quantum number m . The frequency of the Rabi oscillations shows that the transition rate depends on the resonating electric or magnetic field and the according dipole moment. The radiative decay rates of the (36, 34) parent state and the (37, 33) daughter state are taken into account by the parameters $\gamma_{r_p} = 4.81 \times 10^5 \text{ s}^{-1}$ and $\gamma_{r_d} = 4.38 \times 10^5 \text{ s}^{-1}$. The total decay rate γ_T can be defined as

$$\gamma_T = \frac{\gamma_{r_p} + \gamma_{r_d}}{2} + \gamma_e \quad (6.4)$$

where γ_e is the rate for elastic collisions with other helium atoms.

6.2 The Laser Pulse

If the laser beam is assumed to travel along the x axis with linear polarization in z direction then the Gauss function

$$P(x, y, z, t) = P_0(x, y, z) e^{-4\ln(2)(\frac{t-t_0-x/c}{\delta t})^2} \quad (6.5)$$

describes the temporal change of the laser power at a defined target position. Ideally the interaction point should be centrally inside the cavity. The full width at half maximum δt of the laser pulse was always between 9 ns and 12 ns. The intensity is given through the relation

$$I = \sqrt{\frac{\pi}{4\ln(2)}} P_0 \delta t = 1.064 P_0 \delta t. \quad (6.6)$$

P_0 denotes the peak power, given in MW/cm², I in mJ/cm² and δt in ns. In the stopping region of the antiprotons the laser intensity should be uniform and the (laser) electric field E_z in this region of the form $E_z = E_0(t) \cos(\omega t)$ and position independent. The laser energy density is defined as the laser energy divided by the area of the laser beam. The term $\cos(\omega t)$ relies on

the angular frequency $\omega/2\pi$ corresponding to the laser transition frequency. E_0 depends on the laser power profile and is defined as

$$E_0(t) = E_0 e^{-\frac{1}{2} \ln(2) \left(\frac{t-t_0}{\delta t/2} \right)^2} \quad (6.7)$$

with $E_0 = 2.745 \times 10^6 \sqrt{P_0/[MW/cm^2]} [NC^{-1}]$ [53].

6.3 Electric Dipole Moment & Rabi Oscillations

For every quantum number m in the range $-L \leq m \leq +L$ one can define a different electric dipole moment caused by the slightly varying transition rates for each m state in a present electric field (Fig. 6.1). Taking into account all different quantum numbers the Rabi frequencies are written as [61]

$$\begin{aligned} \Omega_m &= \frac{\mu_m E(t)}{\hbar} \times \frac{10^{-22}}{c} \\ &= 2\pi 0.44 \sqrt{\Theta(t)} \langle n', L', F', J', m | \mu | n, L, F, J, m \rangle \end{aligned} \quad (6.8)$$

given in GHz with laser fluence $\Theta(t) = [\text{kW/cm}^2]$ and n, L, F, G, J being the quantum numbers for each transition. The equation was solved for all m states using Wigner's 6-j symbols – a generalization of Wigner's 3-j symbols and the Clebsch-Gordon coefficients. They are defined as

$$\begin{aligned} \langle n', L', F', J', m | \mu_m | n, L, F, J, m \rangle &= (-1)^{J'+m} \left(\begin{array}{ccc} J & 1 & J' \\ m & 0 & -m \end{array} \right)_{3-j} \\ &\times \sqrt{(2J+1)(2J'+1)} \left| \left\{ \begin{array}{ccc} F' & J' & \frac{1}{2} \\ J & F & 1 \end{array} \right\}_{6-j} \right| \\ &\times \sqrt{(2F+1)(2F'+1)} \left| \left\{ \begin{array}{ccc} L' & F' & \frac{1}{2} \\ F & L & 1 \end{array} \right\}_{6-j} \right| \langle n', L' | \mu | n, L \rangle \end{aligned} \quad (6.9)$$

The reduced dipole moment $\langle n', L' | \mu | n, L \rangle$ is retrieved from

$$\langle n', L' | \mu | n, L \rangle = 1.8 \sqrt{2L+1} \sqrt{\frac{\lambda^3}{\tau}} \times 10^6, \quad (6.10)$$

given in Debye units with λ denoting the transition wavelength in meters and τ the radiative decay time in seconds.

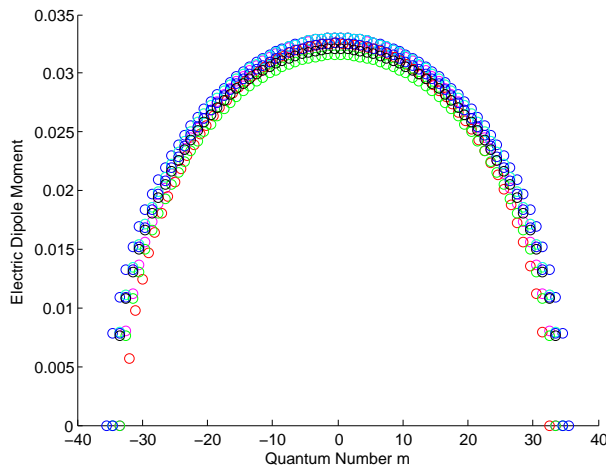


Figure 6.1: Electric dipole moment of $\bar{p}^3\text{He}^+$, calculated for all quantum numbers m . The different colored circles refer to the eight different SSHF substates of the $(n, L) = (36, 34)$ state.

6.4 Laser Transitions

In order to induce a laser transition $(n, L) = (36, 34)$ to $(n', L') = (37, 33)$, Eq. 6.1 can be modified such that $\gamma_{r_p} = \gamma_r$ refers to the radiative transition from the metastable state $(36, 34)$ to the $(35, 33)$ state and $\gamma_{r_d} = \gamma_A$ represents the Auger transition from the unstable state $(37, 33)$. The calculated values for these decay rates are $\gamma_r = 480.7$ MHz and $\gamma_A = 330$ MHz [28]. The elastic (dephasing) collisions rate $\gamma_e = \gamma_c$ can not be calculated exactly. However, it can be estimated by comparison of the numerical simulations with the experimental results. Theoretical calculations define limits for $\frac{\gamma_e}{2\pi} = \frac{\gamma_c}{2\pi}$ as ~ 0.08 GHz and ~ 0.2 GHz [62]. This numerical model does not consider the possibility of simultaneous population exchange between three or more quantum states, but it provides a good approximation.

Due to the considerably shorter lifetime of the Auger decay state, the radiatively decaying state is gradually depopulated over the time of the laser pulse. Figure 6.2 displays the temporal development of the population of the different states in the case of a laser-stimulated transition from parent to daughter state. The evolution of populations was obtained by numerically solving the optical Bloch equations in Eq. 6.1 with the Runge-Kutta formula. Thereby the shape of the laser pulse was assumed to be rectangular as a good approximation while experimentally the shape consisted of several adjacent

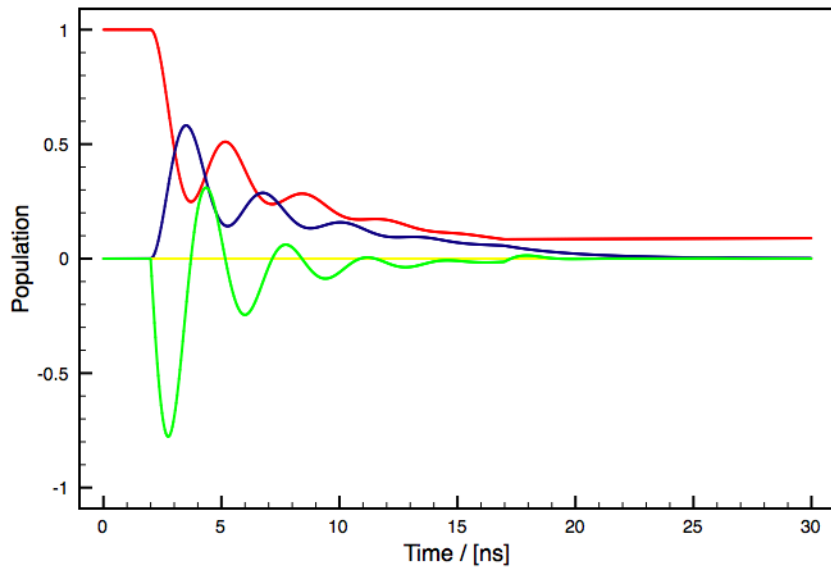


Figure 6.2: Time dependent population evolution of states for the $(36, 34) \rightarrow (37, 33)$ laser transition. ρ_p is represented by the red line, ρ_d blue line, ρ_x green, ρ_y yellow.

Gauss profiles.

6.4.1 Doppler Broadening

Depending on the temperature the antiprotonic helium atoms move randomly inside the target and with respect to the incident laser beam. Their velocities follow a Maxwell-Boltzmann distribution. The laser wavelength is thus shifted for each atom based on the velocity and the direction in which it is moving with respect to the beam. Due to this Doppler effect ν_D the laser beam is broadened. The whole setup has to be cooled to reduce this effect and improve the experimental precision. The full width at half maximum (FWHM) can be written as [63]

$$\Delta\nu^D = 2\nu_0 \sqrt{\frac{2(\ln 2)k_B T}{M_{tot}c^2}}. \quad (6.11)$$

The mass of the system is M_{tot} , the temperature T , k_B denotes the Boltzmann constant and ν_0 the laser frequency. For $\bar{p}^3\text{He}^+$ the laser wavelength is 723.877 nm. The total mass of the atom adds as

$$M_{tot} = 2M_p + M_n + M_{\bar{p}}M_{e^-} \simeq 4M_n. \quad (6.12)$$

Table 6.1: These are the calculated values for Doppler broadening at different temperatures for the transition at 723.877 nm.

	Doppler Width [MHz]
$\Delta\nu_{T=2K}^D$	209
$\Delta\nu_{T=6K}^D$	362
$\Delta\nu_{T=12K}^D$	512
$\Delta\nu_{T=50K}^D$	1044

Table 6.1 gives the calculated Doppler broadening for the given system at several temperatures.

To account for this effect in the numerical simulation the laser transitions are calculated for a 3σ range of frequencies and weighted with the Gaussian distribution

$$f(x) = \frac{1}{\sigma\sqrt{2\pi}} \exp\left(-\frac{1}{2}\left(\frac{x}{\sigma}\right)^2\right) \quad (6.13)$$

with σ being the standard deviation

$$\sigma = \frac{\Delta\nu}{2\sqrt{2(\ln 2)}}. \quad (6.14)$$

The Rabi oscillations are calculated for several frequency steps over this 3σ range around the transition frequency. The results for different temperatures are displayed in Fig. 6.3. Broadening due to the laser linewidth of 100 MHz is therefore negligible compared to the Doppler broadening at the measurement temperature of 6 K.

6.4.2 Refilling from Higher Lying States

There is also refilling from upper states which has an effect on the population of the measured ones (see Fig. 6.4). Therefore the two higher lying, radiatively decaying states for the parent state (36, 34), i.e. (37, 35) and (38, 36), as well as for the daughter state (37, 33), i.e. (38, 34) and (39, 35), will be taken into consideration. Including these four refilling terms into the density matrix for this system leads to the following optical Bloch equations to obtain the laser depletion efficiency

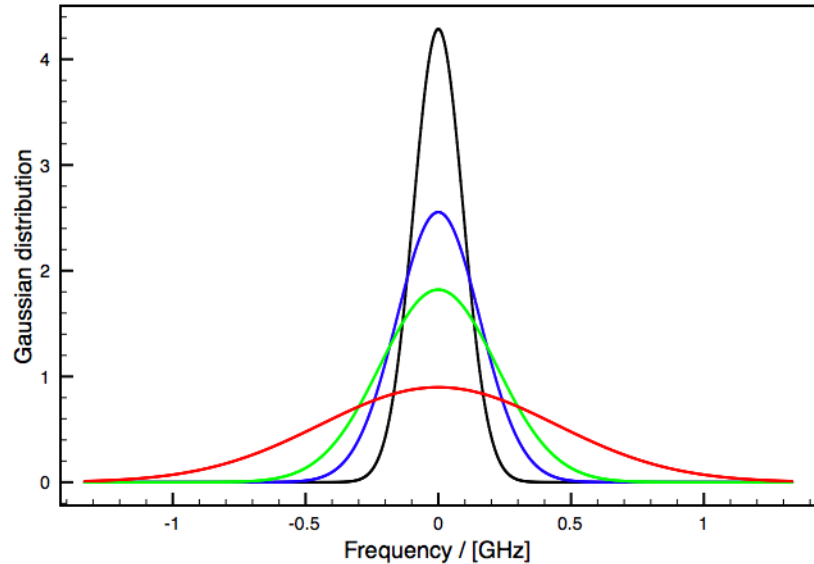


Figure 6.3: The graph represents the calculated Gaussian resonance profile at a target density of 250 mbar for different temperatures – $T = 2$ K (black), $T = 6$ K (blue), $T = 12$ K (green) and $T = 50$ K (red).

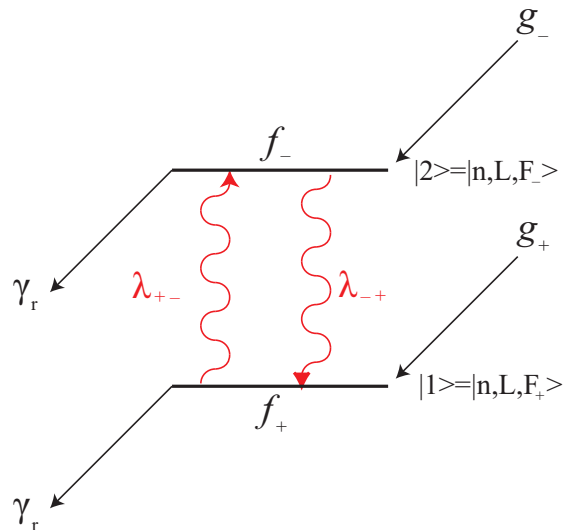


Figure 6.4: Energy level diagram of part of the cascade showing the refilling $g_{\pm}(t)$ from above states, decay to lower states γ_r and the relaxation collision rate $\lambda_{\pm \rightarrow \mp}$ [26].

$$\frac{d}{dt} M = \frac{d}{dt} \begin{pmatrix} \rho_p \\ \rho_d \\ \rho_x \\ \rho_y \\ \rho_{(37,35)} \\ \rho_{(38,34)} \\ \rho_{(38,36)} \\ \rho_{(39,35)} \end{pmatrix},$$

$$M = \begin{pmatrix} -\gamma_r & 0 & 0 & \frac{1}{2}\Omega_m(t) & \gamma_{(37,35)} & 0 & 0 & 0 \\ 0 & -\gamma_A & 0 & -\frac{1}{2}\Omega_m(t) & 0 & \gamma_{(38,34)} & 0 & 0 \\ 0 & 0 & -\gamma_T & -\Delta\omega & 0 & 0 & 0 & 0 \\ -\Omega_m(t) & \Omega_m(t) & \Delta\omega & -\gamma_T & 0 & 0 & 0 & 0 \\ 0 & 0 & 0 & 0 & -\gamma_{(37,35)} & 0 & \gamma_{(38,36)} & 0 \\ 0 & 0 & 0 & 0 & 0 & -\gamma_{(38,34)} & 0 & \gamma_{(39,35)} \\ 0 & 0 & 0 & 0 & 0 & 0 & -\gamma_{(38,36)} & 0 \\ 0 & 0 & 0 & 0 & 0 & 0 & 0 & -\gamma_{(39,35)} \end{pmatrix} \quad (6.15)$$

The rates $\gamma_{(n,L)}$ for the radiative transitions $(n,L) \rightarrow (n-1,L-1)$ are calculated to be [64]:

$$\begin{aligned} \gamma_{(37,35)} &= 0.4538 \text{ MHz} & \gamma_{(38,34)} &= 0.3920 \text{ MHz} \\ \gamma_{(38,36)} &= 0.4161 \text{ MHz} & \gamma_{(39,35)} &= 0.3431 \text{ MHz}. \end{aligned} \quad (6.16)$$

The transition frequency depends on the magnetic quantum number m due to the magnetic dipole moment μ_m in the Rabi frequency. The quantum number is here defined as $m = -37 \rightarrow +37$ resulting in 75 possible cases this equation has to be solved for. ρ denote the population densities of the different affected states. To reduce the calculation time this was done only for the final set of parameters and otherwise the average magnetic moment was applied. By solving the optical Bloch equations for the laser transition the final populations after the laser pulse are calculated. Thus, the laser depopulation efficiency can be extracted (see Ch. 7.2.2 for a definition). It was calculated to be in the order of $\sim 80\%$ – varying with different laser power. Any undesired effect such as Doppler broadening may cause the two laser transition lines to overlap. This means that the population asymmetry and thus the population available for a microwave-stimulated transition will be smaller and consequently reduce the signal. Even though simulations lead to different expectations, the two laser transitions could experimentally be

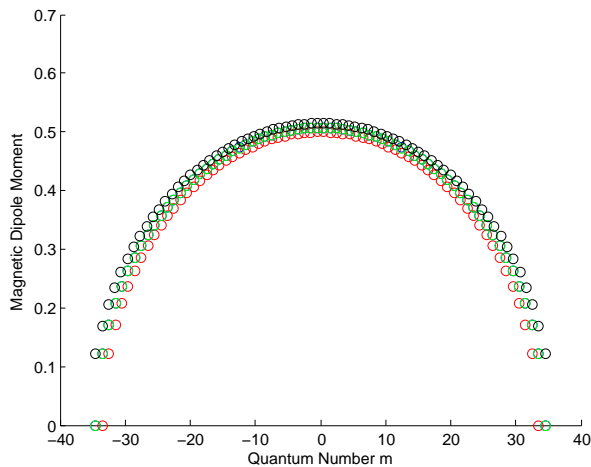


Figure 6.5: Magnetic dipole moment of $\bar{p}^3\text{He}^+$, calculated for all quantum numbers m . The different colored circles refer to the eight different SSHF substates of the $(n, L) = (36, 34)$ state.

well resolved. It can be explained by the so-called *Dicke narrowing* which appears when the collision rate is comparable in size to the Rabi oscillations [65, 66]. If the laser bandwidth is too large, this effect is not visible, however for the current width of 100 MHz it could be observed. Due to its complexity this effect has not yet been implemented in simulations.

6.5 Magnetic Dipole Moment & Rabi Oscillations

As explained in the beginning of the chapter the Rabi frequency in a magnetic field is defined to be [53]

$$\Omega_m(t) = \frac{\mu_m B(t)}{\hbar} \quad (6.17)$$

The microwave-induced magnetic field $B(t)$ – for cylindrical cavities – can be written as

$$B_0 = \sqrt{\frac{\mu_0 Q P}{\pi a^2 \omega d J_1'^2(P_{11})}} \quad (6.18)$$

and $B(t) = B_0 \times \Theta(t - t_{\text{Laser1}}) \times \Theta(t_{\text{Laser2}} - t)$ with a Heaviside step function $\Theta(t)$. P denotes the power in the cavity, a the radius, d the length of the cavity, ω the angular frequency of the microwave, P_{11} the first root of the

Bessel function $J_1(x)$ and $J_1'^2 = -0.403$. The magnetic dipole moment can be given as [53]

$$\mu_m = \langle n, L, F', G', J' | \mu | n, L, F, G, J \rangle. \quad (6.19)$$

This can be solved equivalently to the laser transitions with Wigner's 3-j and 6-j symbols so that

$$\begin{aligned} \langle n, L, F', G', J' | \mu | n, L, F, G, J \rangle &= (-1)^{J'+m} \left(\begin{array}{ccc} J & 1 & J' \\ m & 0 & -m \end{array} \right)_{3-j} \\ &\times \sqrt{(2J+1)(2J'+1)} \left| \left\{ \begin{array}{ccc} G' & J' & \frac{1}{2} \\ J & G & 1 \end{array} \right\} \right|_{6-j} \\ &\times \sqrt{(2G+1)(2G'+1)} \left| \left\{ \begin{array}{ccc} F' & G' & \frac{1}{2} \\ G & F & 1 \end{array} \right\} \right|_{6-j} \\ &\times \sqrt{(2F+1)(2F'+1)} \left| \left\{ \begin{array}{ccc} \frac{1}{2} & F' & L \\ F & \frac{1}{2} & 1 \end{array} \right\} \right|_{6-j} g_e \mu_b \langle \frac{1}{2} | s_e | \frac{1}{2} \rangle \end{aligned} \quad (6.20)$$

with g_e being the gyromagnetic ratio and μ_b the Bohr magneton.

6.6 Microwave Transitions

The optical Bloch equations can also be applied to solve for the microwave-induced population transfer between HF substates. In this situation the daughter and the parent state – as indicated for the laser transitions – are both substates of the (36, 34) state. Thus the radiative decay rate for the transition (36, 34) \rightarrow (35, 33) is $\gamma_{r_p} = \gamma_{r_d} \equiv \gamma_r$ and for the present system $\gamma_r = 0.4807$ MHz. This relates to the total decay rate for the microwave transition as

$$\gamma_T = \frac{\gamma_{r_p} + \gamma_{r_d}}{2} + \gamma_e = \gamma_r + \gamma_e. \quad (6.21)$$

γ_e can be defined as the collisional effect on the coherence between parent and daughter state. As for the laser transitions this parameter can not be identified correctly only by comparison of the simulations with the experimental data.

In the experimental situation there can be inelastic collisions which induce spin flips between the J states. These need to be considered within

the Bloch equations setup for all four allowed transitions of the system. The equations further include the two higher refilling states and the decay rates. Thus the density equation, an 18×18 matrix can be written

$$\frac{d}{dt}\rho = M\rho \quad (6.22)$$

where ρ is the combination of all populations

$$\begin{pmatrix} \rho_{---} \\ \rho_{+--} \\ \rho_{x--} \\ \rho_{y--} \\ \rho_{--+} \\ \rho_{+-+} \\ \rho_{x-+} \\ \rho_{x-+} \\ \rho_{-+-} \\ \rho_{-+-} \\ \rho_{x+-} \\ \rho_{y+-} \\ \rho_{-++} \\ \rho_{++} \\ \rho_{x++} \\ \rho_{y++} \\ \rho_{(37,35)} \\ \rho_{(38,36)} \end{pmatrix} . \quad (6.23)$$

The transition matrix M for the microwave transitions is

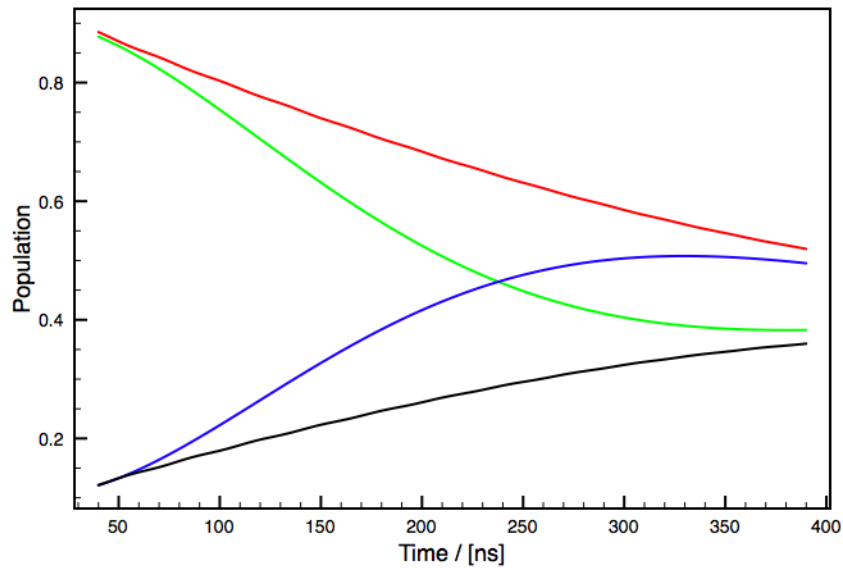


Figure 6.6: The population change in dependence of the time in case of a microwave stimulated transition –the red line refers to the J_{--+} state, the green line to the J_{--- state, the blue line to J_{+-+} and the black one to J_{++-} . See Ch. 2.3 and Fig. 2.3 for reference.

The new collision parameter γ_c can be calculated as $\gamma_c = \gamma_r + 3\gamma_i$ with γ_i relating to the inelastic collisions which cause single spin-flip transitions. Higher spin-flip transitions are not taken into account [62]. This inelastic collision parameter can only be approximated. The dephasing effect on the coherent states does not depend directly on γ_i but is defined through γ_e . The solution to the density equation gives – as for the laser transitions – characteristic Rabi oscillations. For this experiment it is fundamental to have a high population transition rate. Therefore microwave time and power should be optimized. This is achieved after half a Rabi oscillation. Figure 6.6 displays the time evolution of populations during the microwave pulse. In figures 6.7 to 6.10 the Rabi oscillations are displayed for different values of collision rates, laser delay and microwave power.

Signal-to-Noise Ratio

The annihilation products from the decay of the $(n, L) = (37, 33)$ state originating from the microwave-stimulated population transfer in the parent

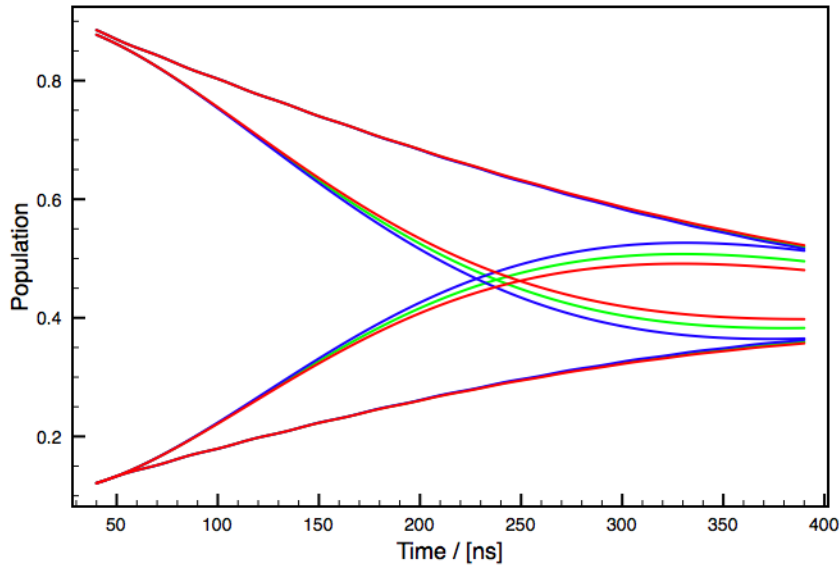


Figure 6.7: Rabi oscillation with elastic collision rate $\gamma_e = 2.5$ MHz (blue), $\gamma_e = 3.5$ MHz (green) and $\gamma_e = 4.5$ MHz (red).

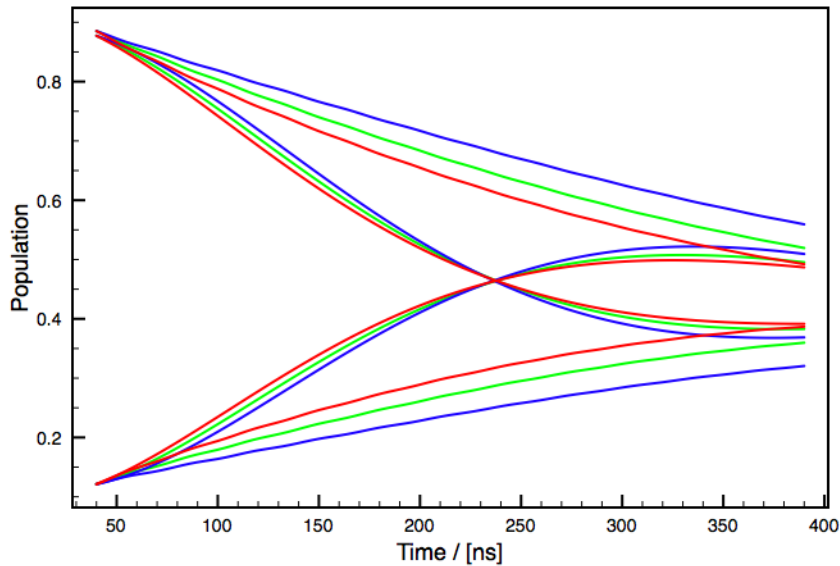


Figure 6.8: Rabi oscillation with inelastic collision rate $\gamma_i = 1.0$ MHz (blue), $\gamma_i = 1.4$ MHz (green) and $\gamma_i = 1.8$ MHz (red).

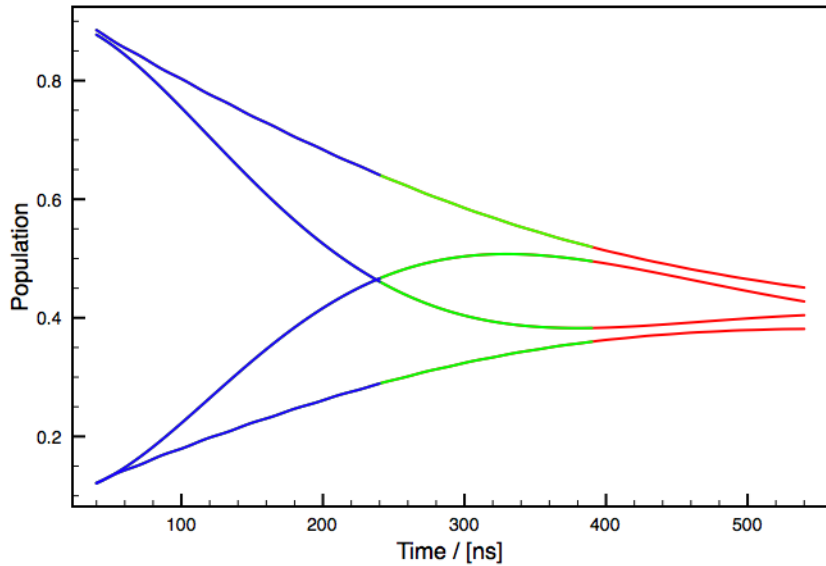


Figure 6.9: Rabi oscillation with laser delay time of $t = 200$ ns (blue), $t = 350$ ns (green) and $t = 500$ ns (red).

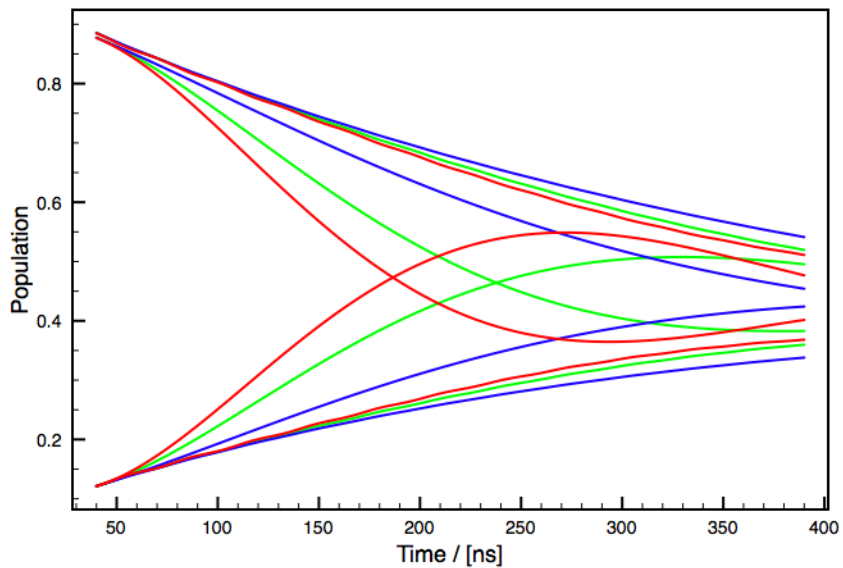


Figure 6.10: Rabi oscillation microwave power $P = 2$ W (blue), $P = 6$ W (green) and $P = 10$ W (red).

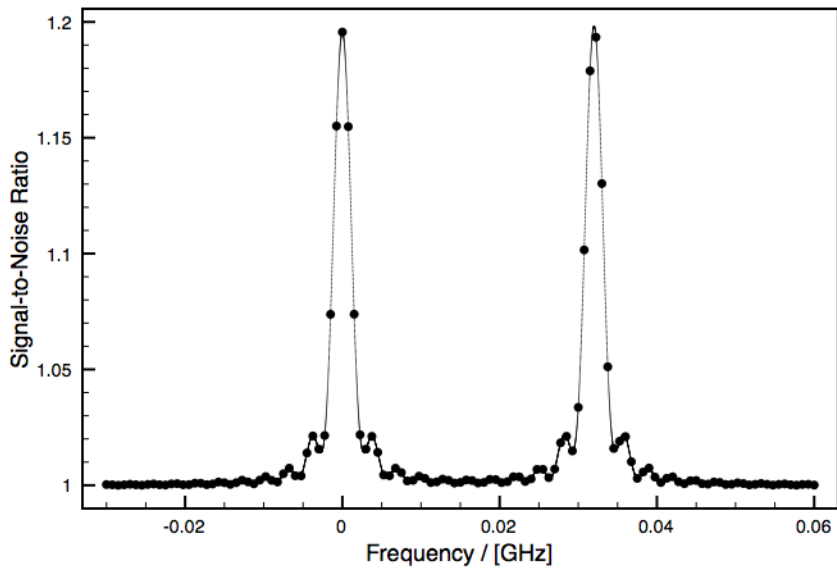


Figure 6.11: Solution to Eq. 6.26 for different microwave frequencies. The origin is the resonance frequency of the first microwave transition. The dots represent calculated frequencies, the solid line has been created by spline interpolation.

state are primarily pions. These can be measured by Cherenkov detectors. The recorded signal S may be expressed as

$$S \propto \sum_{J_1, J_2, J_3 = (+, -)} (\rho J_1 J_2 J_3) |_{\text{after 1st laser}} - \sum_{J_1, J_2, J_3 = (+, -)} (\rho J_1 J_2 J_3) |_{\text{after 2nd laser}}. \quad (6.25)$$

During the time delay between the two lasers, the influence of the microwave on the signal strength depends on the discrepancy of the microwave frequency and the resonance frequency. Therefore a wide enough frequency range around the two resonance transition frequencies needs to be scanned. The signal measured without any microwave pulse or with a microwave frequency far off the resonance region is used to determine the noise level. The relative signal that relates to the population transfer is then defined by the signal-to-noise ratio

$$\text{signal-to-noise ratio} \simeq \frac{\text{signal}|_{\text{with microwave}}}{\text{signal}|_{\text{without microwave}}}. \quad (6.26)$$

The equation was solved for 41 frequency steps in an interval of ± 100 MHz around the transitions resonance frequencies. The used parameters were a temperature of 6 K, $\gamma_{e_{laser}} = 250$ GHz, a laser power of 10 mJ, microwave pulse length of $t = 350$ ns, $\gamma_{e_{MW}} = 3.5$ MHz, $\gamma_i = 1.4$ MHz and a microwave power of 6 W. The electric and magnetic dipole moments were averaged over all quantum numbers. To assure that the averaging does not significantly distort the signal, a cross-check was done using Monte Carlo simulations to obtain results which better reflect physical reality. The Bloch equations were solved for random values of m and in the end the populations were averaged. A 200 step Monte Carlo simulation was done for 11 different microwave frequencies.

The conclusion was that simple averaging the moments over all m is overestimating the signal-to-noise ratio by about 18-20% compared to randomly distributed moment contribution. In appendix D figures D.1 to D.7 show the dependence of the signal-to-noise ratio on various measurement parameters.

6.7 Collisional Effects

The measurement of transitions between the hyperfine structure substates and a comparison to theoretical calculations allows to investigate the collisional processes between the helium atoms of the target medium and the antiprotonic helium atomcules. The elastic and inelastic collision rates γ_e and γ_i can have considerable systematic effects on the signal height, line shape and frequency of the transition line. While inelastic collisions will result in a spin exchange between the hyperfine substates which can lead to a decrease of the measured signal, elastic collisions can cause a broadening and shift of the resonance line. In order to be able to better understand the line shape of the microwave-induced M1-transitions it is crucial to take into consideration also the collisional effects. As already pointed out in this chapter, these rates can not be calculated exactly. However, they can both be estimated by comparison of numerical simulations with the experimental results.

To compare the experimental results to the simulated data, the only free parameters in the simulation were the collisional rates. For other decay rates, microwave power, laser delay and cavity characteristics the same val-

ues as for the actual measurement were applied. Since the rates of collisional effects can not be calculated exactly, they have to be achieved by comparing the measured data to the simulation. By comparison of the measurement to the simulated resonance curve the value for the collisional relaxation rates used in the density matrix when solving the optical Bloch equations can be assessed. These values are similar to those for $\bar{p}^4\text{He}^+$. The elastic collisions rate is about 2 MHz and the rate for the inelastic collisions between antiprotonic helium atomcules and helium atoms – which causes an electron spin exchange – is ~ 1.1 MHz. The theoretical estimate for the inelastic collisional relaxation effects is 1 MHz at a temperature of 6 K [44]. There is no estimation from theory for the elastic collision rate.

If there is no polarization of any of the atomcules or any of its constituents then there is a statistically distributed population of the (super-)hyperfine substates. It is assumed that initially, at a time $t = 0$, hyperfine substates with different J are all statistically populated. The time dependence of these states will be governed by the same processes as between the two laser pulses but without the microwave field. In the case of a simple two-level system the total relaxation rate is the sum of transition rates $\lambda(1 \rightarrow 2) + \lambda(2 \rightarrow 1)$, i.e. approximately twice the rate of the $(2 \rightarrow 1)$ transition. For an eight-level system like $\bar{p}^3\text{He}^+$ this will be more complex. To give an estimation, twice the rate of a dominant transition may be applied. At a temperature $T = 4K$ and choosing a transition with a transition rate of $3 \times 10^6 \text{ s}^{-1}$, the estimated survival probability for the population of this state at $t = 750$ ns is 1%, i.e. very small. Chosing the optimal laser delay will always have to be a compromise – short enough to ensure a good population asymmetry between two HF substates and long enough for the resonance line width to be narrow.

Chapter 7

Data Analysis

The data are first processed with Labview programs (as described in Ch. 3) and finally saved in so-called ROOT data files. ROOT is an object-oriented, C++ based framework used for data analysis and interpretation in particle physics. The data analysis is split up in two parts – an online analysis which is carried out after every antiproton shot based on the produced ADATS and the offline analysis using self-written ROOT programs to process the data. The on-time observation and analysis after every antiproton pulse and recorded measurement point is necessary to check for potential problems with the trigger timing, the lasers, the antiproton beam intensity or the microwave apparatus and consequently repeat a shot and/or eliminate it from the data file. A more thorough offline analysis allows accurate investigation of systematic effects, more distinct averaging of data and precise error calculation. These data – the peak-to-total ratios for all data points together with several other measurement variables – are finally calculated during this online data processing and stored in so-called ntuples¹ as .root files. For all self-contained data sets, such as one microwave scan, separate ntuples were created.

7.1 Pre-Analysis (Online)

Several parameters such as PMT gain, offsets, range, resolutions of DSO need to be adjusted to ensure data recording in highest possible resolution and the timings have to be checked and correctly implemented in the online

¹An ntuple is a sequence of – potentially n – components which can be any kind of mathematical objects

analysis code. The laser timing can be kept track of via a diode. The first thing to control after an antiproton pulse arrival is the prompt peak to see if a high intensity signal was detected. The beam profile gives further feedback. Finally the annihilation peak(s) on the spectra recorded by the two Cherenkov DSOs confirm if the measurement, timing and intensity are correct. These control mechanisms are particularly relevant in the beginning of a shift to tune the beam and optimize the peak-to-total.

The ADATS are time spectra with a voltage representing the number of events at a given time. The PMTs that finally produce the output voltage proportional to the number of \bar{p} induced annihilations are gated such that the immediate prompt peak is excluded. The focus in the online analysis is then lying on the two outstanding laser annihilation peaks and an accurate determination of the exponential background. Referring to Fig. 3.3 the area A_p of the laser-induced peaks is proportional to the population transferred from the metastable to the Auger-decay dominated state which then annihilates within nanoseconds. The area below the decaying background curve is proportional to the created $\bar{p}^3\text{He}^+$ population. This integral is denoted as A_t . From these two quantities we obtain the peak-to-total ratio already described in Ch. 3,

$$r_{ptt} = \frac{A_p}{A_t}. \quad (7.1)$$

This normalization becomes necessary due to the shot-to-shot intensity fluctuations of the antiproton pulse. To calculate the area of the background (total) one has to integrate over all bins of the histogram within the time gate of the photomultipliers. The annihilation peak areas A_p are calculated by integrating the bins within a defined peak area. In accordance with the present laser timing two time windows of several hundred nanoseconds are defined. The program is designed such that the highest value within these ranges can be determined. The time of the laser pulses is found using constant-fraction-discrimination. The exact range for integration is 70-90 ns. In Fig. 7.1 p_1 and p_2 denote the time of the first and second laser pulse. These are the regions to be integrated to define the peak areas A_s . The fitting range for the annihilation background is to be found manually from the produced ADATS and implemented in the analysis code. The background area is then calculated through an exponential fit function

$$f_p = N_0 \exp(-\gamma_p t) + C \quad (7.2)$$

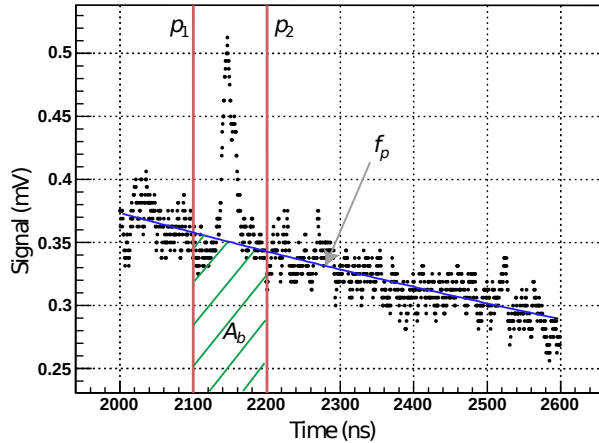


Figure 7.1: This is part of the annihilation spectrum to explain the online analysis procedure. A_s denotes the total area within the fit limits, A_b is the area under the background fit (marked with green lines). These areas relate to the area A_p of the annihilation peak as $A_s - A_b = A_p$ [26].

for the chosen region of the spectrum – here ~ 600 ns, indicated by the blue line in Fig. 7.1. The amplitude N_0 is a normalization factor proportional to the initial antiprotonic helium population and γ_p defines the average antiproton annihilation rate. To avoid distortions of the fitting, the bins within the laser peak regions around p_1 and p_2 are not included. Finally the peak areas A_b are assessed through the fit function f_p by integrating the bins within the defined peak ranges around p_1 and p_2 . The pure annihilation peak area can thus be related to as

$$A_p = A_s - A_b. \quad (7.3)$$

The error calculation online has to take into account three different sources of uncertainty for the peak-to-total ratio. The statistical fluctuations of the $\bar{p}\text{He}^+$ helium atoms are obtained by simply calculating the deviation σ_f from the fit for every bin of the histogram. The same needs to be done for the analog noise of the photomultiplier signal. Then the squared sum of the residual for the entire fit range has to be normalized to the total area A_f under the fit curve within the range b_1 to b_2 which thus gives the error. This can further be converted to the error in the very peak by multiplying it with the sum of A_b and A_s [67]. The third source of uncertainty is the digitization error due to the resolution of the digital oscilloscope. This error σ_d can be calculated from the resolution of the DSO by adding it over

the defined peak range. Therefore the combined error of the single components is given with the standard formula for the quadratic sum of the errors as follows

$$\sigma_{ptt} = \sqrt{\frac{A_b + A_s}{A_f} \sum_{f=1}^n \sigma_f^2 + \sum_{d=1}^n \sigma_d^2}. \quad (7.4)$$

These calculations are carried out separately for both laser annihilation peaks and as well for both Cherenkov detector outputs – which we will in future refer to as channels 1 and 2. The pre-analyzed data are then stored in .root data files.

7.2 Extensive Analysis (Offline)

Once the data acquisition is completed, the data are further processed with custom-made C++ programs. This analysis is more distinct and also allows to be selective on the data and to do more careful averaging. The peak-to-total ratio (and the error) for the second laser peak is normalized to the peak-to-total of the first laser peak in order to average out beam intensity fluctuations. This is particularly important since data from different days – and thus different measurement conditions – will be averaged together. The normalizing is done for both channels individually.

$$\begin{aligned} ptt_{21} &= \frac{ptt_2}{ptt_1} \\ \text{err}_{ptt_{21}} &= \frac{\text{err}_{ptt_2}}{ptt_2} ptt_{21}. \end{aligned} \quad (7.5)$$

Finally the two channels are summed up and the data are averaged for every frequency point. All points y_i within a certain range are averaged together using the weighted mean calculation to weight each data point by its error for each point.

$$\bar{y} = \frac{\sum_{i=1}^n \frac{y_i}{\sigma_i^2}}{\sum_{i=1}^n \frac{1}{\sigma_i^2}} \quad (7.6)$$

and the average error for each averaged point being

$$\sigma_{\bar{y}} = \sqrt{\frac{1}{\sum_{i=1}^n \frac{1}{\sigma_i^2}}}. \quad (7.7)$$

The data were fitted with custom-defined fit functions based on an initial set of parameters. To obtain the optimal fit to the data a minimization algorithm – implemented in the ROOT package TMinuit – was used.

7.2.1 Laser Scans

The laser resonance profiles are plotted as the PTT – of the first laser peak since there is no microwave pulse involved – against the laser frequency. The scan over both laser transition lines is fitted in order to assess the central frequency, the two transition frequencies and resonance line widths. From a physical point of view there are several potentially appropriate fit functions to a laser resonance profile. The natural line shape is a Lorentz function

$$L(\omega) = \frac{1}{\pi} \frac{\frac{1}{2}\Gamma}{(\omega - \mu)^2 + (\frac{1}{2}\Gamma)^2} \quad (7.8)$$

where Γ denotes the width of resonance line and μ defines the mean value. In experimental reality however the line shape does not obey a perfect Lorentz function. It is also effected by Doppler broadening which has a Gaussian distribution as

$$G(\omega) = \frac{1}{\sigma\sqrt{2\pi}} \exp \frac{-(\omega - \mu)^2}{(2\sigma)^2}, \quad (7.9)$$

σ^2 denoting the variance. Both distributions can be combined in the Voigt function, a convolution of a Gaussian and a Lorentzian function

$$V(\omega) = \frac{\Gamma}{2\sigma\sqrt{2\pi^3}} \int_{-\infty}^{\infty} \frac{\exp(-\frac{(\omega - \omega')^2}{2\sigma^2})}{(\omega' - \mu^2) + (\frac{1}{2}\Gamma)^2} d\omega'. \quad (7.10)$$

This is a good approach if the contribution of the Doppler broadening is not exactly known.

To determine the quality of a fit the least squares method is a useful tool. A measure for the average deviation of the points from the fit curve is

$$\chi^2 = \sum_{i=1}^N \frac{(\omega_i - \mu_i)^2}{\sigma_i^2} \quad (7.11)$$

with N being the number of degrees of freedom.

The laser scans – representing two distinct annihilation peaks which can be well resolved – are fit with four Voigt functions and a constant offset to account for the signal background.

7.2.2 Laser Depletion Efficiency & Laser Delay Timing

The next important step in the analysis is a systematic measurement with different laser delay timings in order to gain information on laser depletion efficiency and relaxation rates. The principle and motivation was already described in chapter 3. For these studies the peak-to-total of the second laser – averaged over several shots and again normalized to the peak-to-total of the first annihilation peak – is plotted versus the measured laser delay times.

In the case of both lasers firing with a defined time delay, and without any microwave pulse, the fit function (refer to Fig. 7.1) for the data can be derived from the integral of these two equations [68]:

$$\begin{aligned}\frac{d\rho_+}{dt} &= g_+(t) - (\lambda_{+-} + \gamma_r)\rho_+ + \lambda_{-+}\rho_- \\ \frac{d\rho_-}{dt} &= g_-(t) - (\lambda_{-+} + \gamma_r)\rho_- + \lambda_{+-}\rho_+\end{aligned}\quad (7.12)$$

with ρ_{\pm} denoting the population density of the HF substates in question. g_{\pm} is the refilling from higher states and is expected to be constant below $T = 1000$ ns. The relaxation rates from ρ_+ to ρ_- and vice versa are defined as λ_{+-} and λ_{-+} respectively. It is assumed that before the first laser fires the relative populations are

$$\begin{aligned}\rho_{\pm} &= \frac{1}{2} \\ \lambda_{+-} &= \lambda_{-+} \equiv \lambda_i \\ g_+ &= g_- \equiv g.\end{aligned}\quad (7.13)$$

Then one obtains the relations

$$\begin{aligned}r_1(t) &= I_0 \frac{1}{2} \epsilon_1 \\ r_2(t) &= I_0 \rho_+(t) \epsilon_2.\end{aligned}\quad (7.14)$$

I_0 is a normalization constant, ϵ_1 and ϵ_2 denote the laser depletion efficiencies for the two laser pulses. If these conditions are implemented in Eq. 7.12 it results to

$$\frac{r_2(t)}{r_1(t)} = \frac{\epsilon_2}{\epsilon_1} \left[\exp(-\gamma_r t) \left(1 - \frac{\epsilon_1}{2} - \frac{\epsilon_1}{2} \exp(-\gamma_i t) - \frac{g}{\gamma_r} \right) + \frac{g}{\gamma_r} \right]. \quad (7.15)$$

For the other case that only the second laser is fired, i.e. the metastable state was not depopulated before, the PTT is normalized to the average value for the first laser annihilation signal in the previous situation to provide

a basis for comparison of the data. If there is no initial laser depopulation the system is still in thermal equilibrium when the second laser is fired. Therefore no relaxation processes have to be considered and the fit function yields

$$\frac{r_2(t)}{r_1(t)} = \frac{\epsilon_2}{\epsilon_1} \left[\exp(-\gamma_r t) \left(1 - \frac{g}{\gamma_r} \right) + \frac{g}{\gamma_r} \right]. \quad (7.16)$$

7.2.3 Microwave Scans

For the microwave resonance profile the situation is basically equivalent to the laser scan. The peak-to-total is fitted against the microwave frequency. Also these transitions are affected by broadening effects – Doppler and power broadening. In principle the same type of fit function as for the laser scan can be applied. However, finally the natural line shape for a two-level system which is affected by an oscillating magnetic field for a time T was used. It is given by [69]

$$X(\omega) = A \frac{|2b|^2}{|2b|^2 + (\omega_0 - \omega)^2} \times \sin^2 \left\{ \frac{1}{2} \left[|2b|^2 + (\omega_0 - \omega)^2 \right]^{\frac{1}{2}} T \right\}. \quad (7.17)$$

Here $X(\omega)$ is the probability that an atom is transferred from one HF state to the other, ω is the angular frequency of the magnetic field and ω_0 is the angular frequency of the transition between the two energy levels. A is a scaling term which equals 1 in an ideal two-level system. In the fitting procedure this term takes into account that in reality the two-level system is not ideal. The parameter $b = \Omega/2$ is a time independent part of the transition matrix elements between two energy levels, with the Rabi frequency Ω . In the case of a complete π -pulse, one obtains $|b|T = \pi/2$. This is referred to as the optimum case, since together with $X(\omega) = 1$ at resonance this gives the smallest width for the transition line, $\Gamma = \frac{0.799}{T}$ [69]. The Fourier transform of the rectangular microwave pulse gives a lower limit for the transition line width. The two observed microwave resonance transitions were measured and fitted individually with this function and adding a constant background. To cross-check and determine the most accurate fit for the data other functions were tried in comparison [26]. The Gaussian provides a good approximation for the natural line shape – and also the Lorentzian

function. The most accurate approximation is the $\text{sinc}^2\omega$ -function given as

$$\text{sinc}^2\omega = \frac{\sin^2(\omega - \mu)^2}{(\omega - \mu)^2} \quad (7.18)$$

Two different approaches were used to fit the microwave scan data. The first method was to average the data for every frequency point and fit the averaged scan. This method will be referred to as fitting of averaged scans ASF in this work. Another method to analyze the data is to first fit the scans separately, but with frequency, resonance width and amplitude handled as common parameters, before they are averaged and fitted again (see appendix E for the microwave scans fitted with the different approaches and according fit parameters). In this work the method will be referred to as simultaneous fitting of individual scans ISF. The χ^2 gives a much better result, i.e. much closer to 1, if the second method of simultaneous fitting is used. A much more stable χ^2 was obtained for all applied fit functions in this case compared to averaging all data. Nonetheless, due to the antiproton beam fluctuations from shot to shot – in intensity and also pulse arrival time – the χ^2 always turns out higher than 1. Despite accounting for all fluctuations and systematic effects in the system, the error calculations appear to underestimate the effects. The error was therefore multiplied by the square root of the reduced χ^2 .

Chapter 8

Experimental Results

In preparation for the actual investigation of the hyperfine substructure via microwave resonance several studies need to be carried out systematically to optimize the measurement parameters such as laser power, laser resonance frequency, laser delay time or microwave power. Due to limited measurement time available all data that could be recorded with antiprotonic ${}^3\text{He}$ over the period of three years that was dedicated to this project were done at only one target density of 250 mbar.

At the beginning of every beamtime run – once the setup is working smoothly, the beam is tuned and the timing of the experiment is correct – one has to do a ranging of the beam. This means that attenuation to stop the antiprotons inside the target needs to be fine-tuned such that they reach the required energy in the center of the cavity. Therefore, Upilex foils of different thickness – between $20\ \mu\text{m}$ and $120\ \mu\text{m}$ – can be placed in front of the antiproton entrance window to the cryostat and the peak-to-total ratio is measured with sufficient statistics for all thicknesses. As Fig. 8.1 illustrates, the optimum stable region with the highest annihilation signal can be obtained with an additional attenuation of about $70\ \mu$ – which proved to be very similar over the years.

8.1 Laser Resonance Scans

A scan over the laser frequency range was done to determine the frequency offset and the splitting of the two resonance lines f^+ and f^- (see Fig.s 8.2 and 8.3) to ensure that only one of the two hyperfine levels of the $(n, L) = (36, 34)$ state was depopulated by laser stimulation. Several laser scans were

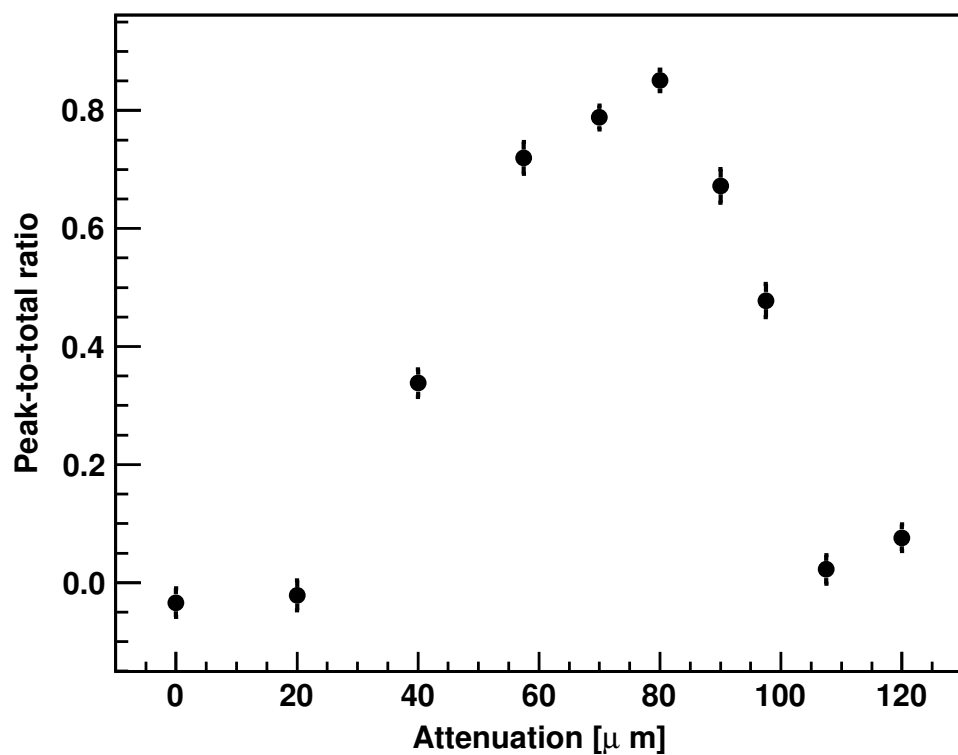


Figure 8.1: The peak-to-total ratio of the first laser annihilation peak as function of the attenuation foil thickness in the course of beam (in μm) to assess the optimal attenuation in order to stop the beam centrally within the target.

recorded at different input power to get an idea of the influence on the resonance linewidth and thus also the splitting of the two lines. The used laser fluences were 10 mJ/cm^2 , 13 mJ/cm^2 , 16 mJ/cm^2 and 20 mJ/cm^2 . These values could be regulated by using thin degrading filter foils which were put in the optical path to reduce the full input power. The idea is to find the appropriate laser fluence where the power is saturated and therefore the laser depletion efficiency is optimized in order to avoid power broadened resonance lines and as a consequence partial depopulation of the other HF transition lines f^- . The pulse length was between 8 ns and 12 ns for all measurements over the three years, which was sufficient in the case of $\bar{p}^3\text{He}^+$. It should be comparable to the Auger lifetime of the daughter state. Generally spoken, the longer the laser pulse the larger the resulting annihilation signal. This also depends on the gain of the photomultipliers which can be slightly varying for each measurement period and makes an overall comparison difficult.

In Fig. 8.3 the laser scan – measured with ^3He for the finally used laser fluence of 13 mJ/cm^2 – is displayed in comparison to the scan with ^4He in Fig. 8.2. The resonance wavelength is $\sim 723.877 \text{ nm}$. During the measurements the laser wavelength was monitored in order to recognize any wavelength drift in time to readjust or to repeat the shot. The splitting is $\Delta f = 1.72 \pm 0.03 \text{ GHz}$, similar to the transition at $\sim 726.090 \text{ nm}$ in $\bar{p}^4\text{He}^+$, with a splitting of $\Delta f = 1.75 \pm 0.01 \text{ GHz}$. Due to the different SSHF energy level spacings one of the laser transition peaks has a lower amplitude and larger width. Each of these peaks consists of another two sub-peaks, corresponding to transitions from one SHF substate of the parent state to the same SHF substate of the daughter state. Two of the four SHF substates respectively are lying close enough to each other to have a frequency difference smaller than the laser linewidth ($\sim 100 \text{ MHz}$) and the Doppler width ($\sim 300 \text{ MHz}$) and can thus not be resolved while the other two lines have a splitting in the range of the broadening and thus result in a smaller and broader peak. This is not the case for $\bar{p}^4\text{He}^+$ which thus shows two equal and high peaks demonstrating a high depopulation efficiency – at the given power of 30 mJ/cm^2 . However, almost all data points lie within a 1σ deviation from the fitting curve and therefore confirm the reliability of the applied fit. For $\bar{p}^4\text{He}^+$ the substates of the two HF resonance lines are lying very close to each other which means that the two peaks are not distinguishable

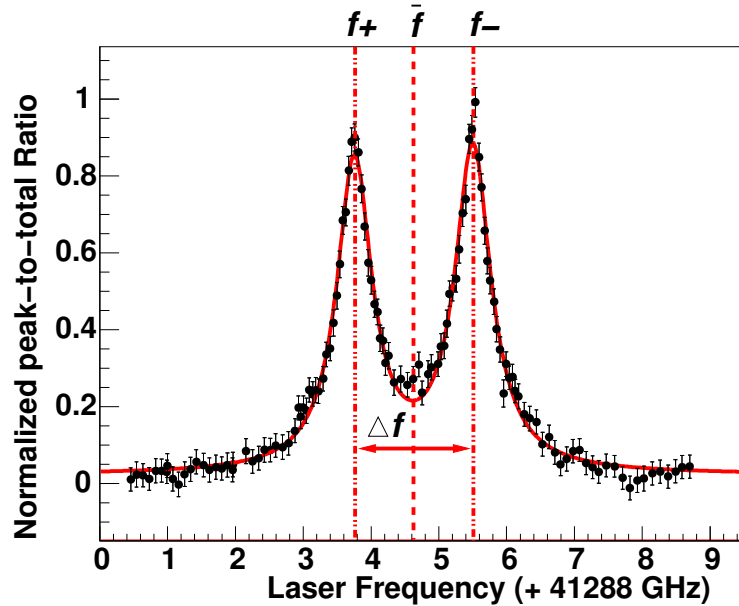


Figure 8.2: A scan over the laser frequency range around the transitions frequencies for the laser transition from the $(n, L) = (37, 35)$ to the $(n, L) = (38, 34)$ state of $\bar{p}^4\text{He}^+$, displaying the two laser transitions f^+ and f^- between the HF states of the parent and the daughter state, at a target pressure of 250 mbar, a temperature of 6 K and a laser fluence of 10 mJ/cm^2 . The peaks are fitted with four Voigt functions referring to the four "allowed" E1 transitions between the SHF states of the parent state (refer to Fig. 3.2). The arrows indicate the corresponding theoretical transition frequencies.

and the HF line will be sharp in contrast to the case of $\bar{p}^3\text{He}^+$. This will result in a much broader – and thus also lower – peak for the f^- transition than for the f^+ transition. The measurements were all performed with a delay time $T = 350 \text{ ns}$ between the two lasers and a target pressure of 250 mbar. These parameters were chosen to provide a basis for comparison to the results in $\bar{p}^4\text{He}^+$. There was no time repeat the measurements at other densities – a study that could have been interesting from a theoretical point of view. Theory suggests that for $\bar{p}^3\text{He}^+$ – as well as for $\bar{p}^4\text{He}^+$ – no dependence of the resonance line shape, width and amplitude on the density is to be expected.

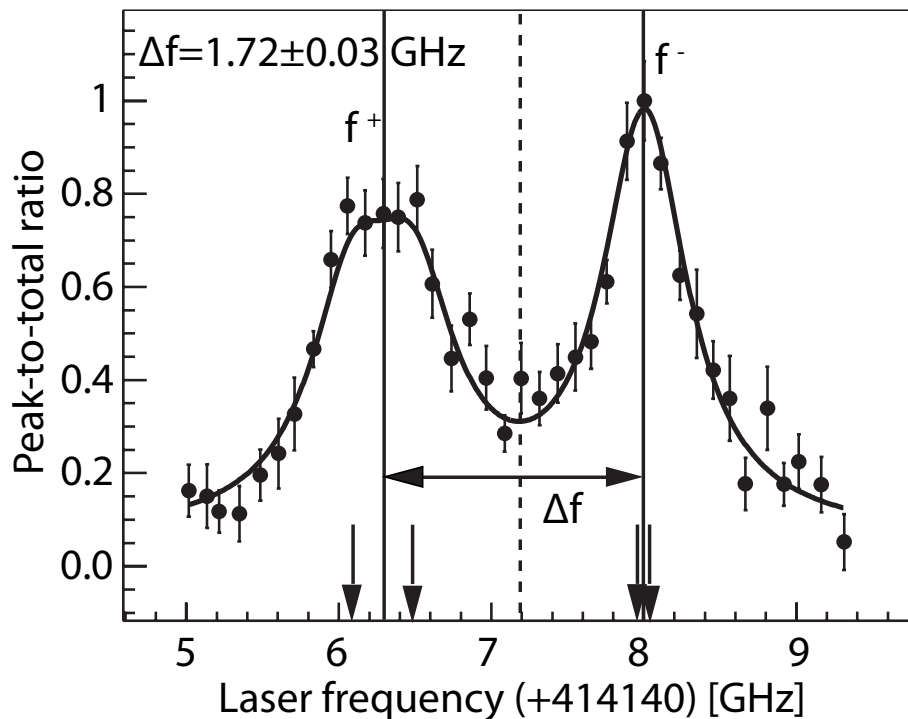


Figure 8.3: A laser frequency scan for the transition from the $(n, L) = (36, 34)$ to the $(n, L) = (37, 33)$ state of $\bar{p}^3\text{He}^+$, displaying the two laser transitions f^+ and f^- between the HF states of the parent and the daughter state, at a target pressure of 250 mbar, a temperature of 6 K and a laser fluence of 10 mJ/cm^2 . The peaks are fitted with four Voigt functions referring to the four "allowed" E1 transitions between the SHF states of the parent state (refer to Fig. 3.2). The arrows indicate the corresponding theoretical transition frequencies.

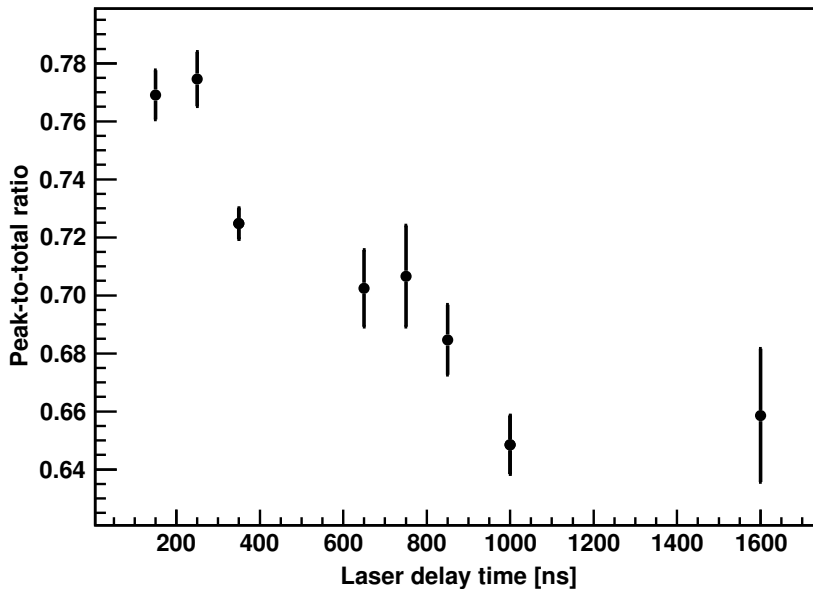


Figure 8.4: Signal-to-noise ratio as function of the laser delay time. The graph displays the relaxation of the system over time for the second laser annihilation peak signal without any previous depopulation.

8.2 Laser Delay Study

Figures 8.4 and 8.5 display the signal-to-noise ratio for several laser delay times. Both pictures are produced by taking the peak-to-total of the second laser annihilation peak. In the first case only the second laser is fired. No asymmetry is created and thus no population transfer and no relaxation process happen. The second case illustrates the situation when both lasers are fired. For all parameter settings the same number of data points is recorded. Displaying this ratio as function of the laser delay time shows the relaxation behavior of the system.

It was difficult to optimize the overlap of the two lasers in the center of the target. As already pointed out previously, this had to be done before every measurement shift – by eye and via projection of the central alignment to a camera more than a meter outside the target. This method makes it impossible to determine a precise value for the diameter of the two laser beams and of their overlap – especially comparable over several days.

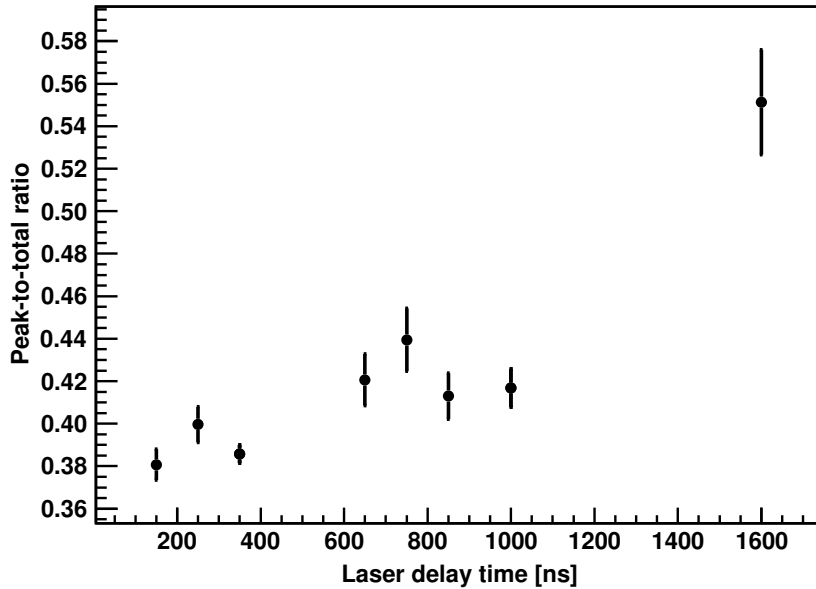


Figure 8.5: Signal-to-noise ratio as function of the laser delay time. The graph displays the relaxation of the system over time for the second laser annihilation peak signal after depopulation by the first laser.

8.3 Microwave Power Study

This microwave measurement was carried out at one frequency point – conveniently the predicted resonance frequency – to assess the optimal microwave power. Several values in the range between 0 W and 20 W were applied, an equal number of data at each power. These microwave powers refer to the amount to be transmitted to the cavity. The correct power to achieve exactly one π -pulse – where the highest population transfer will be induced – has to be determined. The points at 0 W were recorded on resonance. Points were also taken at high power, but well off resonance, i.e. a few hundred MHz away. Off resonance the microwave should have no effect on the atoms. The closer it moves to the resonance transition frequency and the more accurate the microwave power is for a complete spin-flip, the more population transfer is induced and consequently the annihilation signal will rise. Thus off resonance measurements confirm if the observed signal is real and not due to some kind of fluctuations.

The power scans – recorded in 2011 – were completed for both 11 GHz

transitions to cross-check with simulations. Fig. 8.6 shows the scan of the 11.125 GHz resonance. It demonstrates nicely that a π -pulse was completed at the first power maximum of about 7.5 W. For the other transition the same microwave power was applied. In 2010 the used input power was slightly different for both resonances. Due to the lack of time for power scans with sufficient statistics the optimum power appeared not to be the same for the two transitions. The ν_{HF}^{--} transition was measured with a power of about 10 W and the ν_{HF}^{-+} transition at about 7.5 W. It is also possible that this behavior can be explained by the system inherent reflections overlaying the cavity resonance signal. If these are vibration-induced changes during the measurement, they might cause the microwave input signal to be very sensitive to the frequency (see Fig. 5.7 for reference). This would be unpredictable and could thus not be corrected for. The microwave power study was performed only for a laser delay of 350 ns. What would happen at much shorter delay is that the power maximum for the first spin flip is reached only at far higher powers. On the other hand, for a very long interval between the two laser pulses the collisional relaxation of the system would already have eliminated any asymmetry between the two states. The signal would be too low to be observed. Figures 8.7 and 8.8 display the microwave power behavior over the frequency range in the case of the two 11 GHz transitions – with an average fluctuation of 10-13% over the recorded spectrum. Despite thorough calibration of the system, there appears to be a linear tendency of the power over the frequency range. This behavior could potentially lead to a distortion of the line shape and an increase of errors. However, from Fig. 8.6 can be seen that the peak-to-total ratio does not change considerably within the error between a microwave power of 7.5 W and 10 W. Therefore, it is not expected that this linear tendency of the power over the frequency range has a significant effect on the error and the fit of the transitions lines.

8.4 Microwave Resonance Scans

Two of the four allowed SSHF resonance transitions in $\bar{p}^3\text{He}^+$ could be observed. The scans of the two microwave-induced transitions are displayed in Fig.s 8.9 and 8.10. In the final analysis the scans of both data taking periods – in 2010 and 2011 – were taken into account. Each resonance was

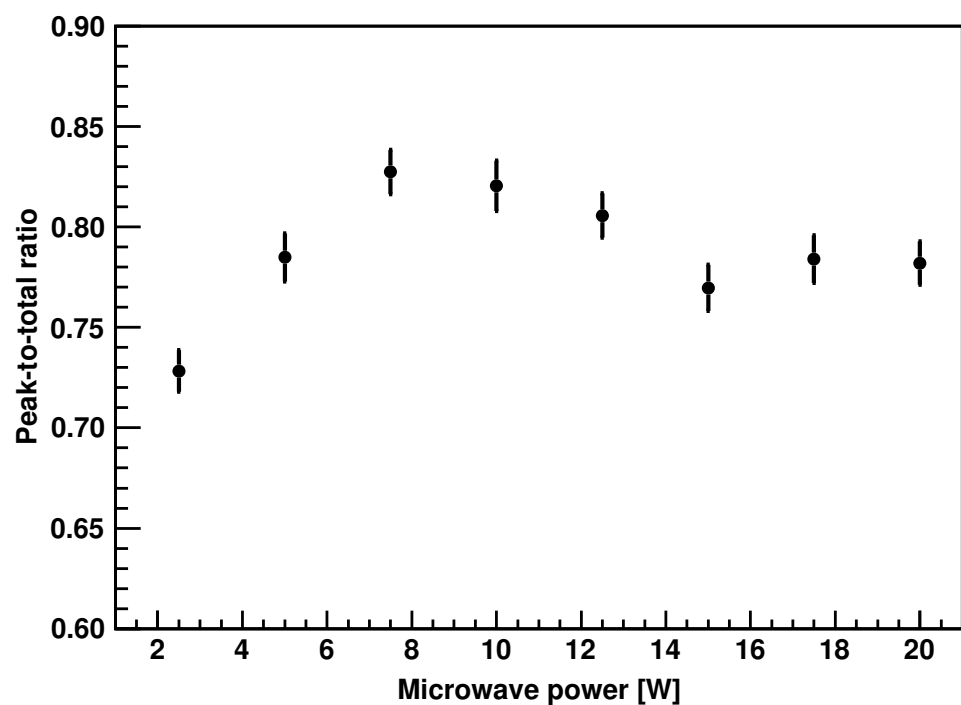


Figure 8.6: This shows the signal-to-noise ratio measured for several microwave powers. The given power value is referring to the pick-up power, i.e. the power that was transmitted to the target. 7.5 W were finally chosen for the microwave spectroscopic measurements.

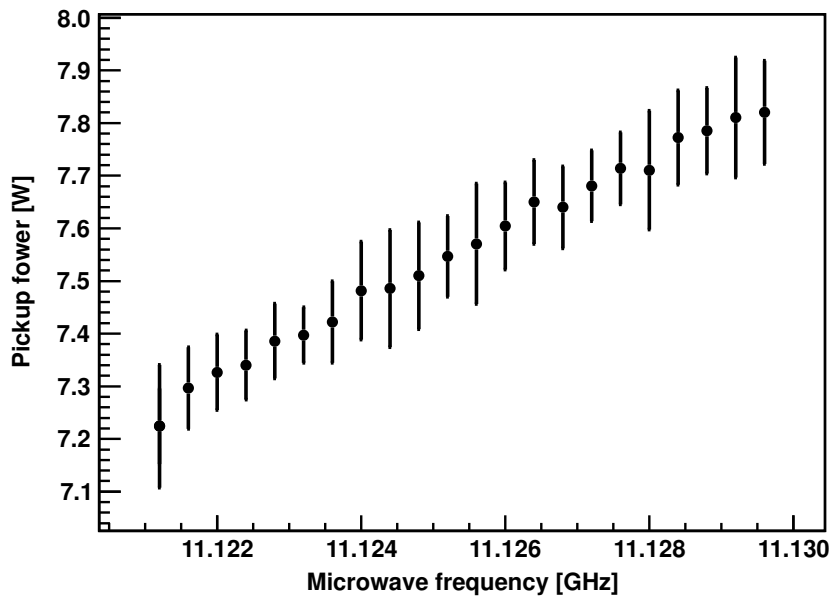


Figure 8.7: The fluctuation of the microwave power over the measured frequency range for the 11.125 GHz transition.

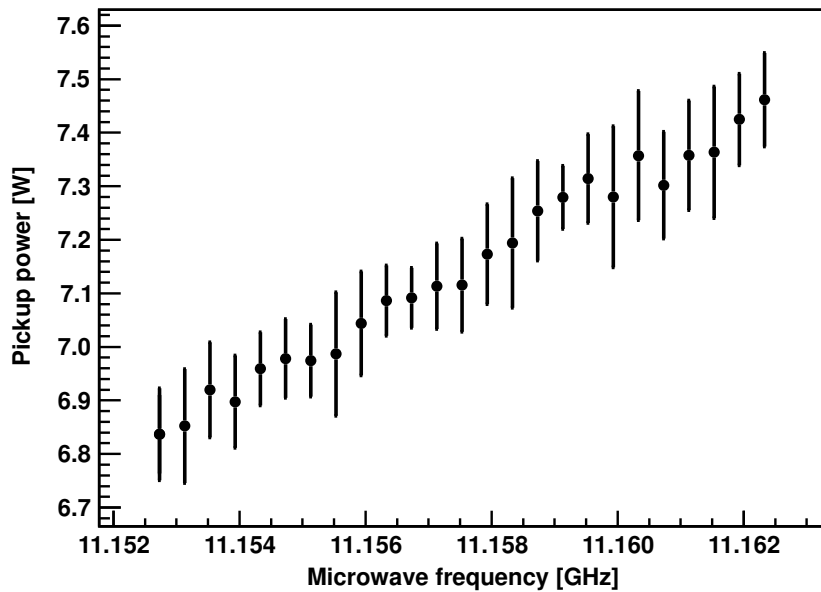


Figure 8.8: The fluctuation of the microwave power over the measured frequency range for the 11.157 GHz transition.

measured and fitted separately. Taking equally spaced frequency points at a reasonable interval over the entire range for both resonance lines would have consumed too much time for one scan. The laser delay for all taken data was 350 ns, the target pressure 250 mbar and the temperature 6 K.

Both transitions were fitted with the function of their natural line shape given in Eq. 7.17. The side peaks in the fit are caused by the Rabi oscillations. From the fit, the frequencies for the measured ν_{HF}^{--} and ν_{HF}^{-+} transitions can be obtained. All relevant results are summarized in Table 8.1. These values were obtained using the simultaneous fitting of individual scans (see Table E.1 in appendix E for the the results of the two different fitting methods). For a pulse length of 350 ns the expected width is $\Gamma = 2.28$ MHz [69], which is roughly in agreement with the measurement. The magnetic field depends on the microwave power as given in Eq. 5.26. This leads to an average oscillating magnetic field amplitude B_0 of $0.24(4) \times 10^{-4}$ T inside the microwave cavity. The Rabi frequency $\Omega = \frac{\mu B_0}{\hbar}$, with μ denoting the calculated averaged magnetic dipole moment, is dependent on the microwave power. Using the calculated values for the magnetic field and the magnetic dipole moment, we obtain a Rabi frequency in the range of 10 MHz.

Note on the Error Calculation There are several systematic effects which had to be considered. The largest influence was due to shot-to-shot fluctuations of the antiproton beam. These effects were reduced by normalizing to the total intensity of the pulse and further normalizing the second annihilation peak to the first one (refer to Section 3). Therefore, mainly shot-to-shot fluctuations of the microwave power and deviations in the laser position and fluence from day to day – although considerably smaller – contributed to the error quoted in Table 8.1. These contributions cannot be assessed individually. They are contained in the error obtained from the fit.

Using the fluctuation of the PTT_1 during the microwave scans as a measure for the errors – that should be constant – gave far too large errors. One has to take into consideration that the scans are averaged over several days with different beam conditions. Therefore, the error correction for an average of all scans might be different from the analysis of a single scan.

For the wavelength measurements the most conservative values for the statistical errors were used – systematic and statistical errors 50:50. How-

ever, that underestimated the error bars for the antiprotonic ${}^3\text{He}$ measurements due to systematic effects. The statistical fluctuation in a PMT signal is mainly given by the efficiency in the photocathode and the multiplication in the first dynode. The size of the stopping distribution is to zeroth approximation irrelevant to the statistical error.

One has to look at the deviation of the background noise from a defined fit function. The digitization error of the digital oscilloscope and different other noise sources – such as from the gating pulse – have to be considered. If the gain or the range for the data acquisition is increased appropriately then the oscilloscope will not record the noise level and thus the error will be reduced.

It was noticed that there are correlated deviations in the ADATS. This was interpreted to be some physical noise which is registered by the measurement apparatus and appears to have a characteristic time constant larger than one bin width. To account for that the background signal is taken at times where there is no peak. In these regions the sum of the ADATS fitted background within a window of the same width as the peak is calculated. This should give zero in the end. To achieve this, the standard deviation of these sums – as this window is continuously shifted up bin by bin over the available peak-free background region – is determined which will provide a better estimate for the error of the peak-to-total even though still underestimating the error by a factor 3. The background fit used a simple graph where all individual errors on the points were implicitly assumed to be 1. Afterwards a rescaling is applied in order to obtain a χ^2 close to 1. Since the values of the background function at subsequent bin centers are not independent – as explained above – they have to be simply added instead of taking the square root of the sum of deviations squared which assumes uncorrelated errors and would thus underestimate them. Autocorrelations in a fitted signal can cause a serious underestimation of the fit errors [71, 72].

Comparison to Simulations The experimental results were finally compared to the simulated data and showed a good agreement. The transition processes were numerically simulated by solving the optical Bloch equations in order to estimate important measurement parameters, in particular the required microwave power and the signal-to-noise ratio. The Bloch equations describe the depopulation of states, in this experiment induced by

Table 8.1: The first experimental results for the ν_{HF}^{-} and ν_{HF}^{-+} in comparison with three-body QED calculations, where ν_{HF} denote the SSHF transition frequencies, δ_{exp} is the relative error of the measured frequencies and Γ the resonance line width. The theoretical precision is $\sim 5 \times 10^{-5}$.

	ν_{exp} (GHz)	δ_{exp} (ppm)	Γ (MHz)	Korobov [37, 70]	$\Delta\nu_{\text{th-exp}}$ (ppm)	Kino [41]	$\Delta\nu_{\text{th-exp}}$ (ppm)
ν_{HF}^{-} (GHz)	11.125 48(08)	7.2	1.69(0.11)	11.125 00(55)		43	11.125 15(55)
ν_{HF}^{-+} (GHz)	11.157 93(13)	11.7	2.20(0.15)	11.157 73(55)		18	11.157 56(55)
$\Delta\nu_{\text{HF}}^{\pm}$ (GHz)	0.03245(15)	523.9		0.0327219(16)	48.9		

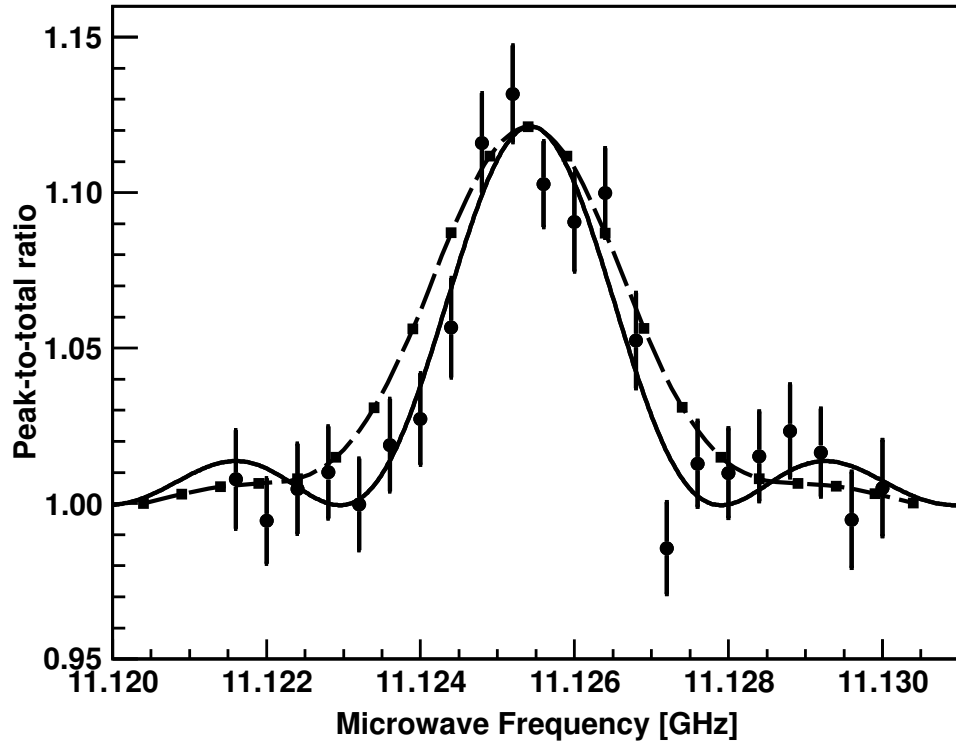


Figure 8.9: Scan over the microwave frequency for the ν_{HF}^{--} transition of the $(n, L) = (36, 34)$ state in $\bar{p}^3\text{He}^+$, at a target pressure of 250 mbar, fitted with Eq. 7.17 (solid line) and the simultaneous fitting of individual scans. The frequency of the measured transition is $\nu_{\text{HF}}^{--} = 11.12548(08)$ GHz. The dashed curve shows a simulation using collision rates obtained from comparison between experiment and simulation.

laser light and microwave radiation and under the influence of collisional effects. For most parameters, such as microwave power, Q value and laser delay, the measured values were taken. The rates of collisional effects – inducing relaxations between the SSHF states – were obtained from adjusting the simulation to the experimental results and they are comparable to the values for $\bar{p}^4\text{He}^+$. The extracted values for the elastic collision rate in $\bar{p}^3\text{He}^+$ is $\gamma_e = 3.5 \times 10^{-3}$ MHz (the same as for $\bar{p}^4\text{He}^+$) and the inelastic collision rate $\gamma_i = 0.52 \times 10^{-3}$ MHz ($\gamma_i = 1.4 \times 10^{-3}$ MHz for $\bar{p}^4\text{He}^+$). Figures 8.9 and 8.10 show the simulations in comparison to the fitted measurement data.

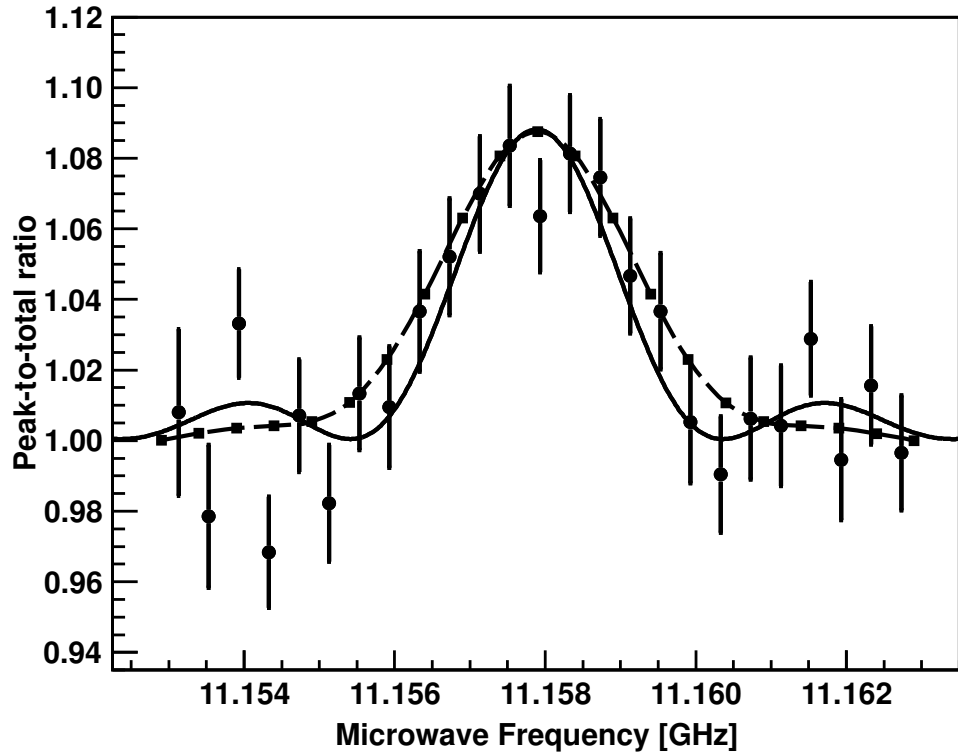


Figure 8.10: Scan over the microwave frequency for the ν_{HF}^{-+} transition of the $(n, L) = (36, 34)$ state in $\bar{p}^3\text{He}^+$, at a target pressure of 250 mbar, fitted with Eq. 7.17 (solid line) and the simultaneous fitting of individual scans. The frequency of the measured transition is $\nu_{\text{HF}}^{-+} = 11.15793(13)$ GHz. The dashed curve shows a simulation using collision rates obtained from comparison between experiment and simulation.

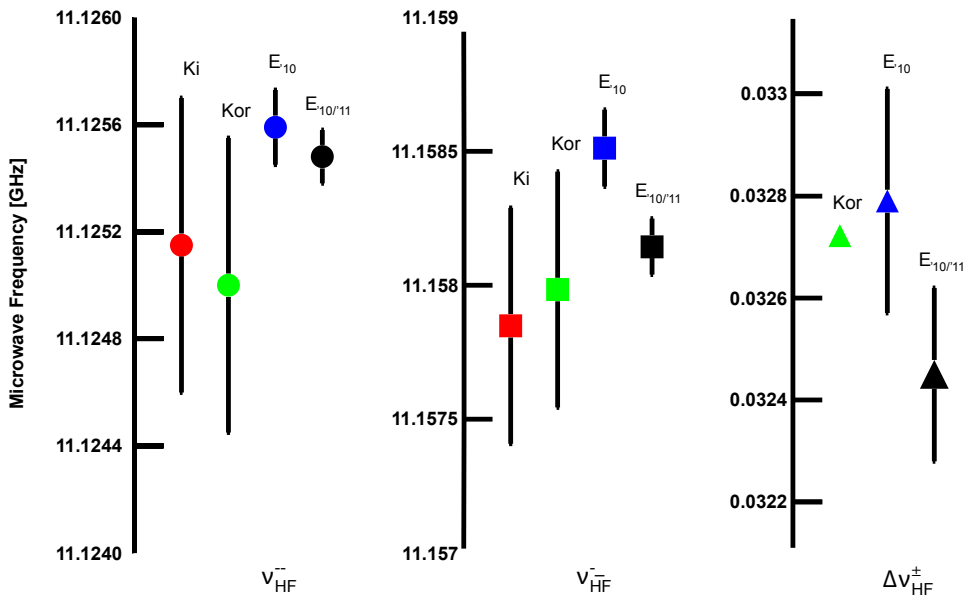


Figure 8.11: This graph summarizes the results for the two measured *SSH* transitions $\nu_{\text{HF}}^{-^-}$ and ν_{HF}^{-+} as well as the frequency difference $\Delta\nu_{\text{HF}}^{\pm}$ (E_{10} [9], $E_{10/11}$) and provides a comparison of these values with the respective theoretical calculations (Kor [37, 70], Ki [41]).

Chapter 9

Conclusion

The goal of this project was to measure the hyperfine structure of $\bar{p}^3\text{He}^+$ using the technique of laser-microwave-laser spectroscopy. Two of the four favored SSHF resonance transitions in $\bar{p}^3\text{He}^+$ were observed and are in agreement with theory [37] within the estimated theoretical error. Also the frequency difference $\Delta\nu_{\text{HF}}^{\pm}$ agrees with theoretical calculations. However, the experimental error for $\Delta\nu_{\text{HF}}^{\pm}$ is still very large compared to theory.

The measured hyperfine transition frequencies agree with theory [37] within less than 1 MHz. The current precision for $\bar{p}^3\text{He}^+$ – about 7 ppm and 12 ppm for the ν_{HF}^{--} and ν_{HF}^{-+} respectively – is still worse than for the most recent results with $\bar{p}^4\text{He}^+$, which gave an error of 3 ppm for the individual transition lines [7]. Due to limitations in antiproton beam quality this precision for $\bar{p}^4\text{He}^+$ is not likely to be improved anymore. However, it is also unlikely to achieve an error with $\bar{p}^3\text{He}^+$ as small as that for $\bar{p}^4\text{He}^+$. There are eight instead of four SSHF energy levels in $\bar{p}^3\text{He}^+$ and thus the measured signal will be only about half of the signal obtained for $\bar{p}^4\text{He}^+$. Therefore much higher statistics would be required.

A comparison of the theoretical values for the two SSHF transitions at 11 GHz with the measurement results shows that there is a small shift in frequency towards higher values for both transitions. The frequency difference $\Delta\nu_{\text{th-exp}}$ between theory and experiment is ~ 0.6 MHz for ν_{HF}^{--} and ~ 0.7 MHz for ν_{HF}^{-+} respectively. According to V. Korobov [70], this discrepancy is most likely due to the theoretical limits of the Breit-Pauli approximation that has been used for the calculations. The relative error of the theoretical frequencies is estimated to be $\alpha^2 = 5 \times 10^{-5}$. The theoretical error for the frequency difference between theory and experiment would then

be ~ 0.6 MHz. Together with the experimental error of ~ 0.2 MHz there is agreement between experiment and theory.

A density dependent shift could also contribute to this deviation. The density dependence is found to be much smaller for the M1 transitions, the electron spin flip transitions induced by the microwave, than for the E1 transitions induced through laser stimulation [73]. For $\bar{p}^4\text{He}^+$ theoretical calculations of G. Korenman [48, 62] confirmed that the density dependence is very small. Also for $\bar{p}^3\text{He}^+$ theory predicts a collisional shift much smaller than the experimental error bars [44].

The deviation between experimental and theoretical values for the frequency difference $\Delta\nu_{\text{HF}}^{\pm} = \nu_{\text{HF}}^{-+} - \nu_{\text{HF}}^{--}$ between the two SSHF lines at 11 GHz is 68 kHz out of 32 MHz. This difference is important due to its proportionality to the magnetic moment of the antiproton. The error of the theoretical value for $\Delta\nu_{\text{HF}}^{\pm}$ is 1.6 kHz, which is considerably smaller than the error of 220 kHz for the value obtained from the measured transitions. The reason is that in theory the splitting between the transition lines can be calculated directly and the errors are the same for all transitions within the hyperfine structure whereas the experimental value of the splitting is received from the difference of the single transition lines. Still, the experimental error is much larger than the theoretical one. There is agreement between theory and experiment within their errors.

The two transitions at 16 GHz could not be measured anymore – even though the microwave target was readily tested and calibrated. However, we came to the conclusion that the observation of these two resonance lines would deliver no additional information on the investigated three-body system and primarily serve to accomplish a complete measurement of the $\bar{p}^3\text{He}^+$ hyperfine structure.

This study with $\bar{p}^3\text{He}^+$ was considered a proof of principle using a more complex system than $\bar{p}^4\text{He}^+$ and a confirmation of the theoretical models. With more statistics and careful investigation and accounting for systematic effects such as frequency dependencies of the single parts of the microwave setup the precision might realistically increase at most by a factor of two. Nonetheless, this would not reach the results achieved with $\bar{p}^4\text{He}^+$ and thus not give a better experimental value for the antiproton magnetic moment, i.e. a better test of CPT invariance.

With this study the spectroscopic measurements of the hyperfine struc-

ture of $\bar{p}^3\text{He}^+$ are concluded. There are no further measurements planned. Based on the current experimental conditions no improvement of precision can be expected. Also the theory reached its limits using the calculation methods available at present.

Acknowledgements

My sincere thanks goes to my supervisor Eberhard Widmann for his support and advice as much as motivation and understanding throughout my work.

Dániel Barna, Masaki Hori, Anna Sótér, Bertalan Juhász, Fritz Caspers, Andreas Dax, Thomas Pask, Desző Horváth, Silke Federmann and Werner Pirkl I would like to thank for their help and fruitful discussions during the experimental beamtimes at CERN. I'm especially grateful to my colleague Oswald Massiczek who was responsible for the cryostat system during the experiment and also had a sympathetic ear in many other matters. I further express my thanks to all the students, including Takumi Kobayashi, Koichi Todoroki, Mario Krenn, Hans-Linus Pfau, Matthias Fink, Johannes Handsteiner and Mariana Rihl who took part in the beamtime during the past few years, spending long hours taking data and helping to make the experiment a success. Leopold Stohwasser, Johann Zmeskal and Doris Stückler I show my great appreciation for their strong support in finding solutions to the trickiest problems with the construction of the microwave cavities. A big thank you goes to the AD operators and everyone involved in providing and improving the antiproton beam which was essential for this work. I also thank the Austrian Science Fund (FWF) for the funding of this project ([I-198-N20]) as a joint FWF-RFBR (Russian Foundation for Basic Research) project.

Thank you to everyone who contributed to make this time an experience I do not want to miss.

I want to use this opportunity to express my deep gratitude to my parents who supported me in so many ways and who made all this possible. I would not be where I am now without my friends – everyone of them, but especially Sabine, Katharina, Nicola, Bernhard and Rahul – to whom I am infinitely thankful for their wonderful friendship and for giving me the confidence to go my way. A special thanks shall also go to all those who challenged me to grow. In modo particolare voglio ringraziare a Domenico – per tutto.

Appendix A

The Smith Chart

The Smith chart, shown in Fig. A.1, is a graphical representation of the input impedance Z_{in} of a length l of transmission line normalized over the characteristic impedance Z_c and phase constant β ,

$$\bar{Z}_{in} = \frac{Z_{in}}{Z_c} = \frac{Z_L + iZ_c \tan(\beta l)}{Z_c + iZ_L \tan(\beta l)} = \bar{R} + i\bar{X} = \frac{1 + \Gamma}{1 - \Gamma} = \frac{1 + \Gamma e^{-2i\beta l}}{1 - \Gamma e^{-2i\beta l}}, \quad (\text{A.1})$$

where Z_L is the load impedance, \bar{R} is the input resistance, \bar{X} is the input reactance and Γ is the reflection coefficient.

It is impractical to plot all the values of Z_L and Z_{in} on rectangular coordinates with one axis corresponding to the real part \bar{R} and the other axis representing the imaginary part \bar{X} . However the values of the reflection coefficient lie in a circle since $|\Gamma| \leq 1$. Additionally each value of Γ corresponds to a value of \bar{Z}_{in} . The input resistance and input reactance are therefore plotted in polar coordinates with $Z_{in} = 1 \pm i0$ at the center and $Z_{in} = \infty \pm i\infty$ to the right.

The corresponding impedance points move on a constant radius circle since a movement of a distance d along the line corresponds to a change in reflection coefficient by $e^{-2i\beta d}$. Therefore a movement $d = \lambda/2$ results in a full rotation returning to the same point. If an impedance $\bar{R}_1 + i\bar{X}_1$ is moved a distance $l = \lambda/4$ on a constant radius circle, Γ_1 becomes $-\Gamma_1$ the impedance becomes:

$$\bar{R}_1 + i\bar{X}_1 = \frac{1 - \Gamma_1}{1 + \Gamma_1} = \frac{1}{\bar{R}_2 + i\bar{X}_2} = \bar{R}_2 + i\bar{X}_2, \quad (\text{A.2})$$

The Complete Smith Chart

Black Magic Design

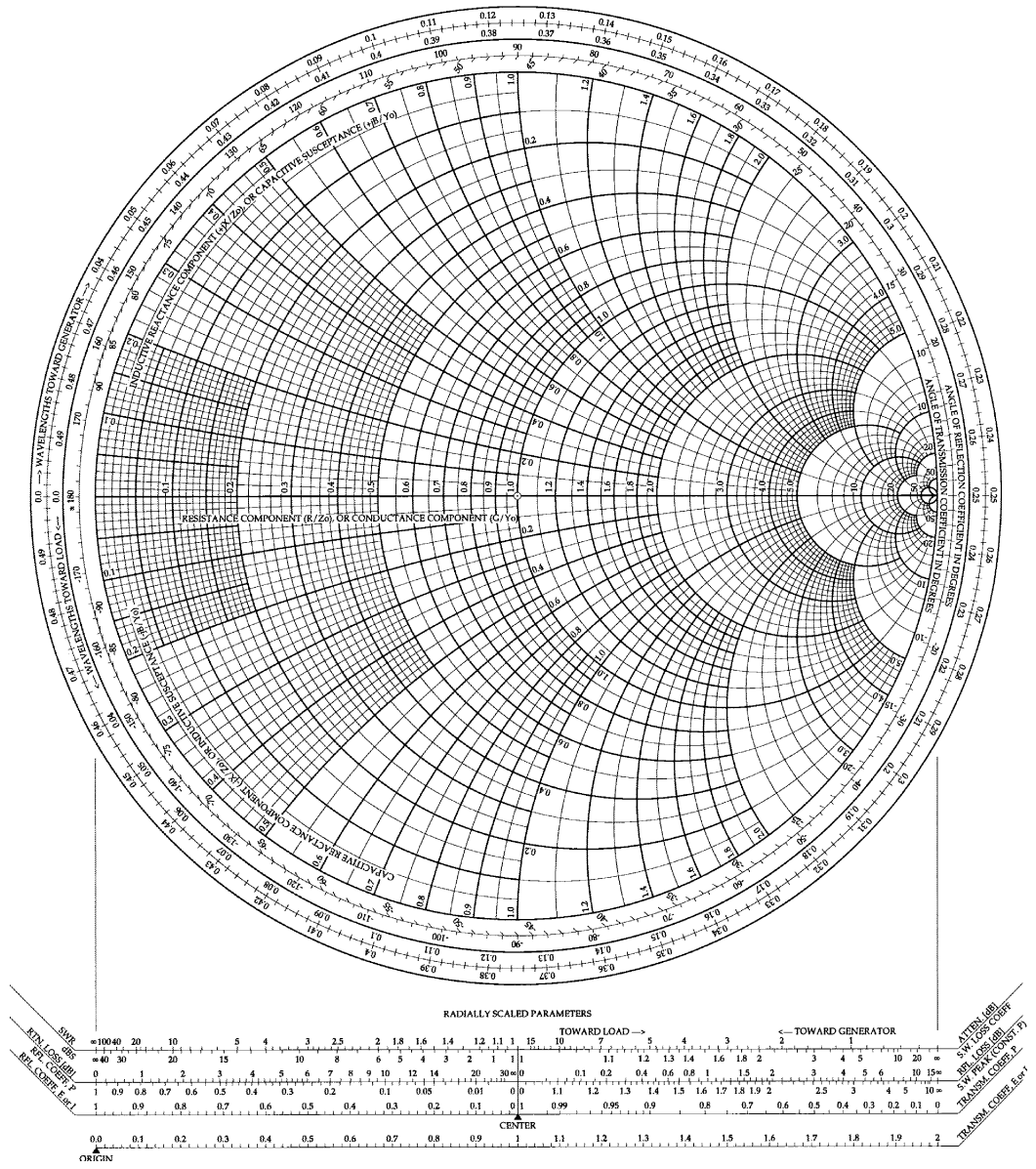


Figure A.1: Smith Chart [26]

where $\bar{Y}_{in} = \bar{G} + i\bar{B}$ is the normalized admittance, \bar{G} is the conductance and \bar{B} is the susceptance. Thus the admittance may be found by taking the point diametrically opposite the impedance point on the Smith chart [26].

An important hint in practise is to use the so-called *electrical delay* on a VNA to adjust the electrical conductor length, thus reduce reflections and improve the readability of the Smith chart – also a not too wide frequency range is of course helpful.

A.0.1 Stub-Tuner

The resonance width in the cavity can be influenced by changing the resistance of the input line. Triple-stub-tuners are a simple way to do this and adjust the coupling to the cavity externally such that the coupling is critical, i.e. perfectly matched and thus the transmission to the target is a maximum.

When a load, a cavity for example, is connected to a transmission line many wavelengths long, it is desirable to match the load to the line. A small change in the operating frequency will change the electrical length $2\beta l = 4\pi l/\lambda$ of the transmission line by a fraction of π radians simultaneously changing the matching.

To match a load to a transmission line, a short-circuited perpendicular stub can be inserted some distance from the load. At this position the normalized input admittance is $\bar{Y}_{in} = 1 + i\bar{B}$. If the stub has a normalized input susceptance $-i\bar{B}$ then they cancel arriving at a matching condition $\bar{Y}_{in} = 1$. The stub length l_0 and position from the load d_0 are given by:

$$d_0 = \frac{\lambda}{4\pi} \tan^{-1} \frac{Y_{in} - 1}{Y_{in} + 1}, \quad (\text{A.3})$$

$$l_0 = \frac{\lambda}{2\pi} \tan^{-1} \frac{\sqrt{Y_{in}}}{Y_{in} - 1}. \quad (\text{A.4})$$

The problem with this system is that it requires a new position d_0 for every load [26].

A.0.2 Multiple-Stub-Tuner

If two stubs are used, their distance from the load becomes arbitrary and only the distance d between each stub is important. The fist stub can add a susceptance $i\bar{B}_1$ which moves a point on the Smith chart along a constant

conductance circle. At the second stub the admittance is $\bar{Y}_b = \bar{G}_b + i\bar{B}_b$, obtained by rotation of $\phi = 4\pi d/\lambda$. If, after the addition of $i\bar{B}_1$ and the rotation, the point lies on the $G = 1$ circle then the second stub can be used to add a susceptance $i\bar{B}_2$ transforming point to the center of the Smith chart (matched condition).

It is clear that not all points on the Smith chart can be matched with this method. Consider the case where $\bar{G} = \bar{G}_0$ such that \bar{G}_0 is the circle of constant conductance made by the tangent of the circle $\bar{G} = 1$ rotated by the angle ϕ . A match cannot be obtained for any values lying within this circle as all values of $\bar{G} < \bar{G}_0$ will not intersect with the rotated $\bar{G} = 1$ circle. Note that as d decreases, the smaller \bar{G}_0 becomes. However loads with $\bar{G}_L > 1$ can always be matched with a double stub-tuner.

This problem is overcome by a third stub. A triple-stub-tuner can match all load admittances since the first stub can be used to transform the point outside the $\bar{G} = \bar{G}_0$ circle. The two remaining stubs act as a conventional double stub tuner [26].

The triple-stub-tuner (TST) is mounted right outside the cryogenic part of the setup. This custom-made device consists of three pieces of rectangular waveguide (about 5 cm length) in a row, perpendicular to the course of the waveguide system, connected to moveable chokes. The chokes can be moved – within a range of 0-25 mm each – with actuators (Sigma Kouki DMY2). With these TSTs the characteristics of the resonance in the cavity can be optimized. The impedance of the transmission line piece between the TSTs and the cavity can be changed such that it matches the impedance of the cavity. Therefore the incoming microwave signal – of which a relevant part would have been reflected at the cavity – now is transmitted and less input power is needed to achieve the desired power inside the target at a defined central frequency, i.e. also the resonance is very sharp. For every frequency point in the desired range appropriate choke positions can be found and thus a narrow resonance in the cavity at the required power.

A.0.3 Quality Factor

When a load has been matched to a transmission line, $Z_{in} = Z_c$. Such a resonant circuit has a quality factor Q , described as the ratio of the decay for an oscillating system amplitude with its period, or

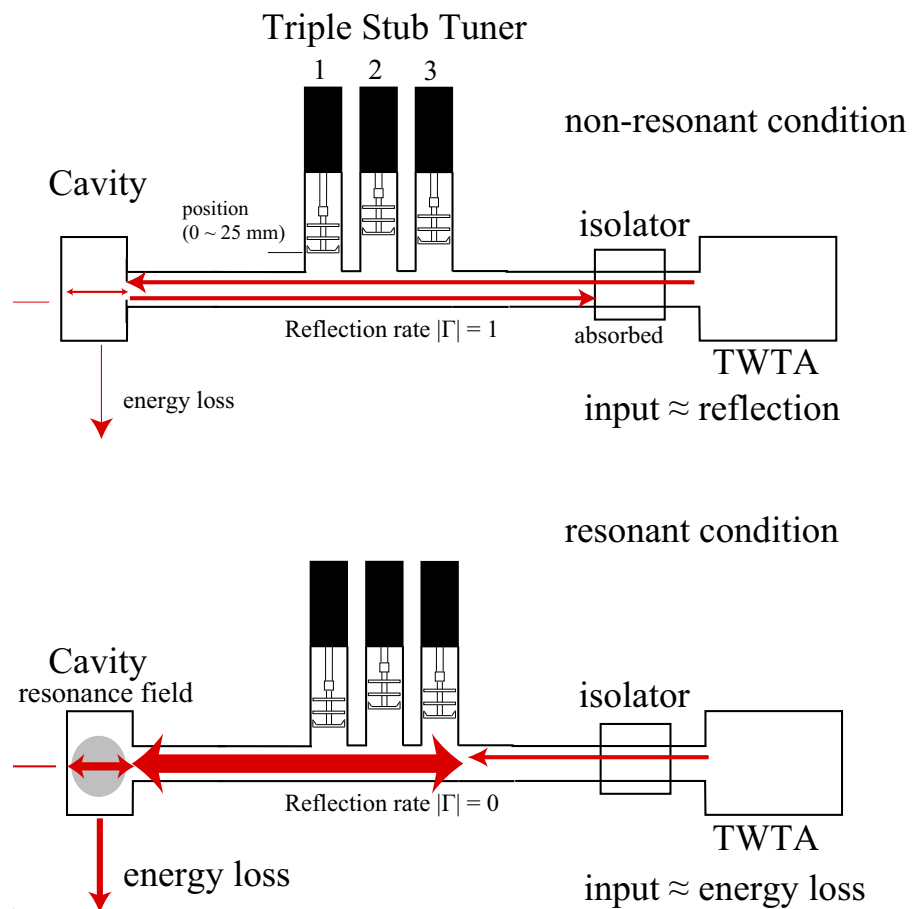


Figure A.2: The triple-stub-tuner setup as it was used with antiprotonic ^4He [53].

$$Q = \omega \times \frac{\text{average stored electric and magnetic energy}}{\text{power loss}}. \quad (\text{A.5})$$

The bandwidth of the circuit is the frequency over which half or more of the maximum power is delivered to the load. This bandwidth is inversely proportional to the loaded Q_L of the circuit.

To calculate the coupling factor β one has to record the impedances as representation on a complex plane – $R + jX = \sqrt{R^2 + (jX)^2}$. The coupling factor is also closely related to the voltage standing wave ratio (VSWR):

$$\begin{array}{lll} 0 < \beta < 1 & \text{under critical/under coupling} & VSWR = \frac{1}{\beta} \\ \beta = 1 & \text{critical/matched} & VSWR = 1 \\ \beta > 1 & \text{over critical/over coupling} & VSWR = \beta \end{array} \quad (\text{A.6})$$

The higher the VSWR the lower is the loaded Q value [26].

Appendix B

Technical Drawings

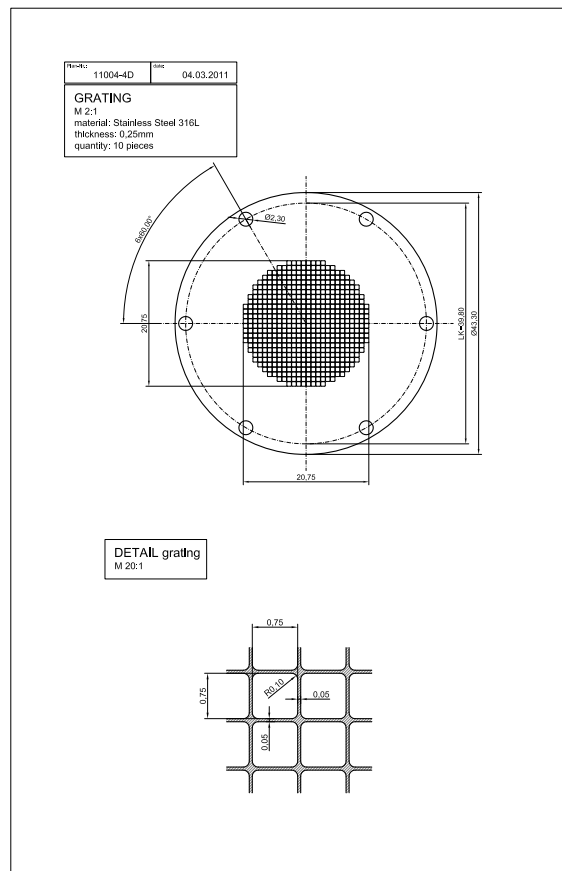


Figure B.1: Technical drawing of the stainless steel gratings for the microwave cavities.

Appendix C

HFSS Simulations

These simulations were carried out primarily to design the two new microwave cavities required for the measurements of $\bar{p}^3\text{He}^+$ with an almost entirely new experimental setup. Only a quick cross-check was done for the newly built cavity at 13 GHz which was used to complete the $\bar{p}^4\text{He}^+$ experiment with the new experimental setup. The following graphs show simulation for the radiofrequency signal that is reflected back before entering the cavity (S11) and the signal which is actually transmitted to the cavity and picked up by the antenna (S21).

Figs. C.1 to C.4 are based on the final dimensions of the built microwave cavities. These values result from careful optimization of all relevant parameters - radius and length of the cavity, iris size and width. Further, also the influence of input power and conductivity of the used material were investigated. The following pictures shall give an overview of these results.

The data tables below give an overview of systematic simulation studies on the various characteristics and dimensions of the microwave targets.

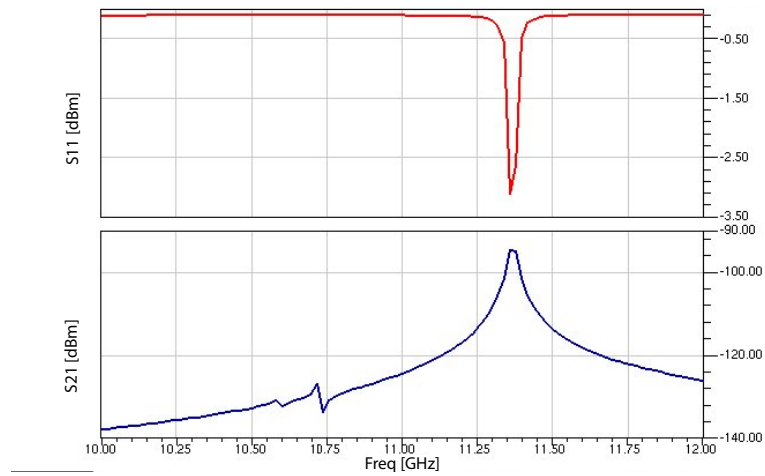


Figure C.1: The reflection (red line) and transmission signal (blue line) for the 11 GHz cavity, with a radius 16.19 mm, a length 26.16 mm and an iris of 7×8 mm.

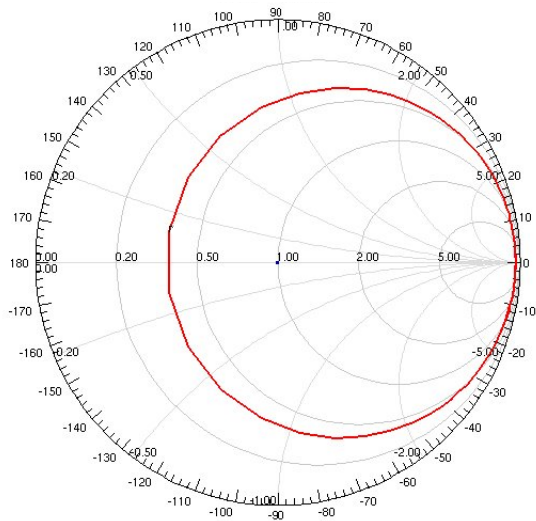


Figure C.2: The reflection (red circle) and transmission signal (blue circle) for the 11 GHz cavity, with a radius 16.19 mm, a length 26.16 mm and an iris of 7×8 mm, displayed on a Smith chart.

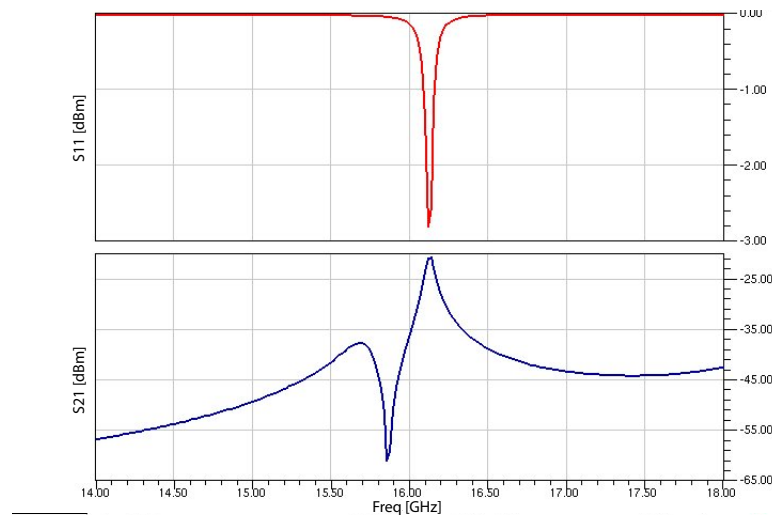


Figure C.3: The reflection (red line) and transmission signal (blue line) for the 16 GHz cavity, with a radius 8.97 mm, a length 22.44 mm and an iris of 6×7 mm.

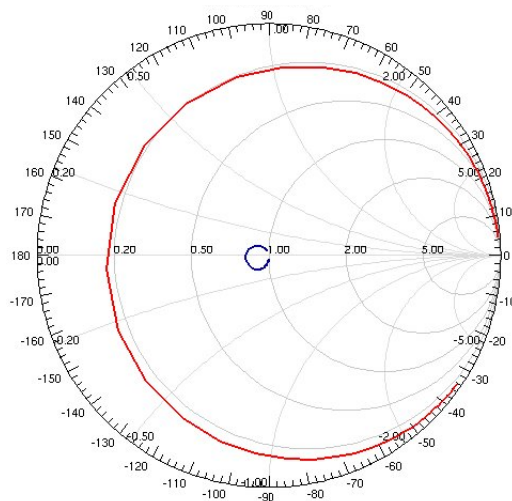


Figure C.4: The reflection (red circle) and transmission signal (blue circle) for the 16 GHz cavity, with a radius 8.97 mm, a length 22.44 mm and an iris of 6×7 mm, displayed on a Smith chart.

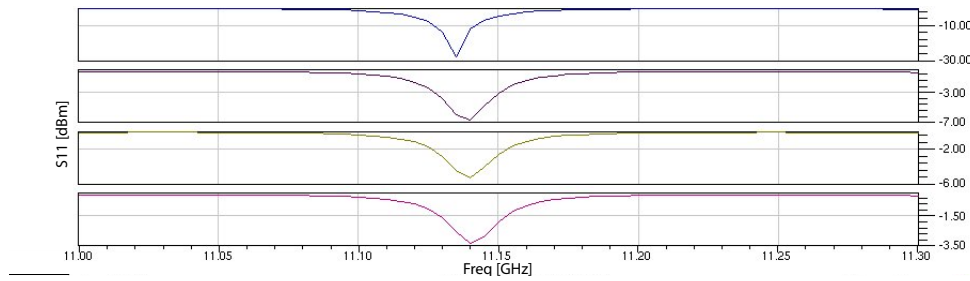


Figure C.5: The reflected signal of the 11 GHz cavity for several different electrical conductivities – 200,000, 1,282,000, 2,000,000, 5,000,000 from top to bottom, given in S/m. 1,282,000 S/m is the actual conductivity for the stainless steel cavity at 4.2 K.

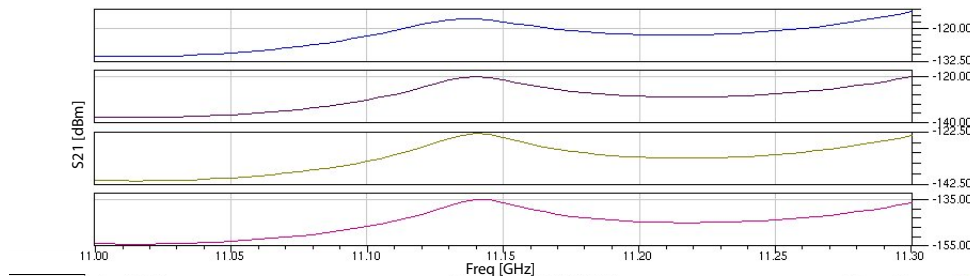


Figure C.6: The transmitted signal of the 11 GHz cavity for several different electrical conductivities – 200,000, 1,282,000, 2,000,000, 5,000,000 from top to bottom, given in S/m. 1,282,000 S/m is the actual conductivity for the stainless steel cavity at 4.2 K.

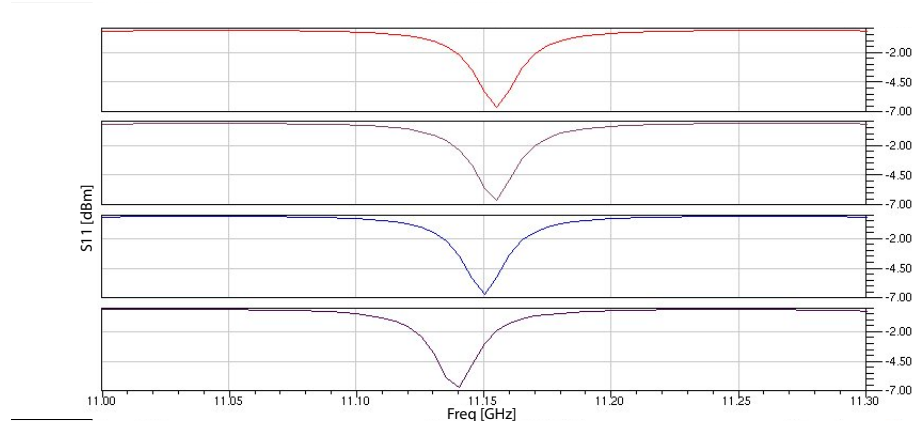


Figure C.7: The reflected signal of the 11 GHz cavity for several different iris dimensions – 2×1 , 4×3 , 6×5 , 8×7 from top to bottom, given in mm. 6×7 mm is the actual iris size for the stainless steel cavity at room temperature.

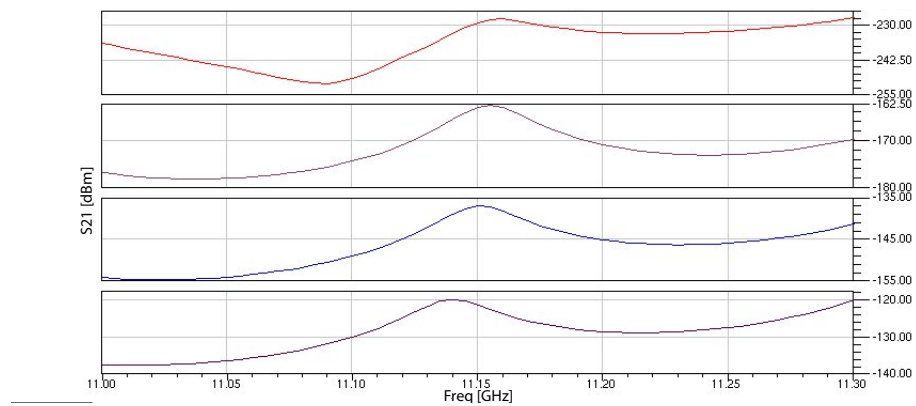


Figure C.8: The transmitted signal of the 11 GHz cavity for several different iris dimensions – 2×1 , 4×3 , 6×5 , 8×7 from top to bottom, given in mm. 6×7 mm is the actual iris size for the stainless steel cavity at room temperature.

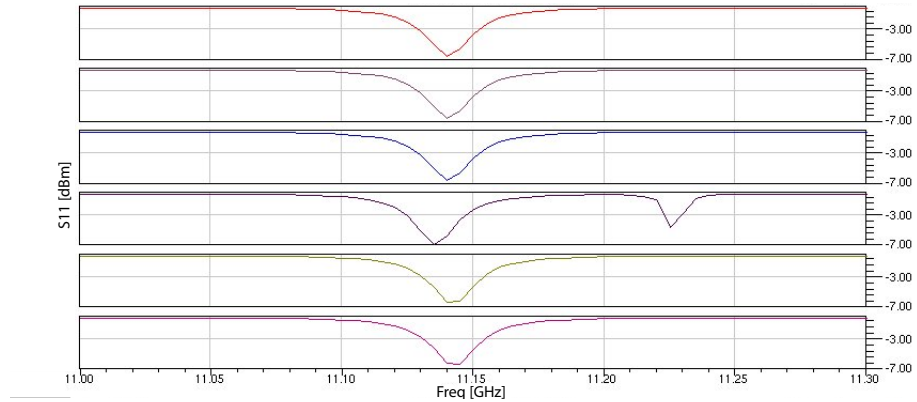


Figure C.9: The reflected signal of the 11 GHz cavity for several different cavity radius – 14.0, 14.8, 15.6, 16.4, 17.2, 18.0 from top to bottom, given in mm. 16.19 mm is the actual radius for the stainless steel cavity at room temperature.

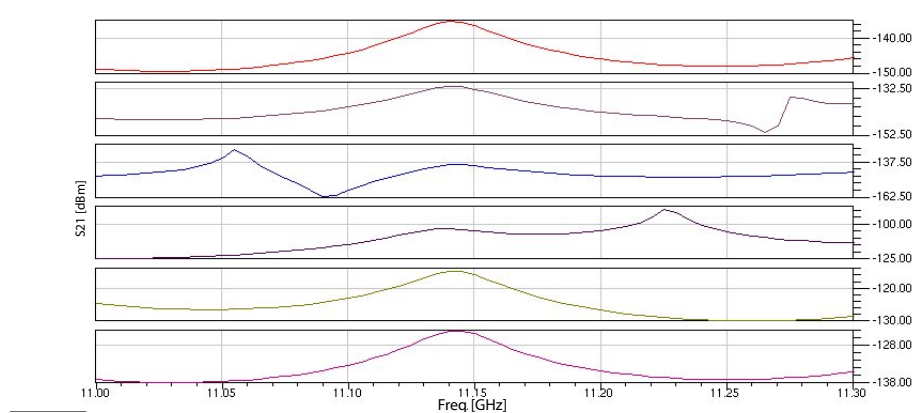


Figure C.10: The transmitted signal of the 11 GHz cavity for several different cavity radius – 14.0, 14.8, 15.6, 16.4, 17.2, 18.0 from top to bottom, given in mm. 16.19 mm is the actual radius for the stainless steel cavity at room temperature.

Table C.1: These data display the results of an eigenmode solution of the microwave setup for several values of electrical conductivity. The cavity length is 28.5 mm, the radius 16.42 mm, the iris 9.5×10 mm and a depth of 1 mm. The unloaded Q strongly depends on the electrical conductivity.

Electrical Conductivity [S/m]	Central Frequency [GHz]	Unloaded Q_0	VSWR	Loaded Q_L
100,000	11.135	690	2.5	198
500,000	11.139	1,544	4.0	308
1,000,000	11.140	2,184	5.3	344
1,887,000	11.141	3,001	7.1	371
10,000,000	11.142	6,907	15.8	411
35,710,000	11.142	13,053	29.2	432
100,000,000	11.143	21,844	48.6	440
5,000,000,000	11.143	154,474	335.2	459

Appendix D

Results of Numerical Calculations

The following plots show a few systematical studies which were also carried out with numerical simulations.

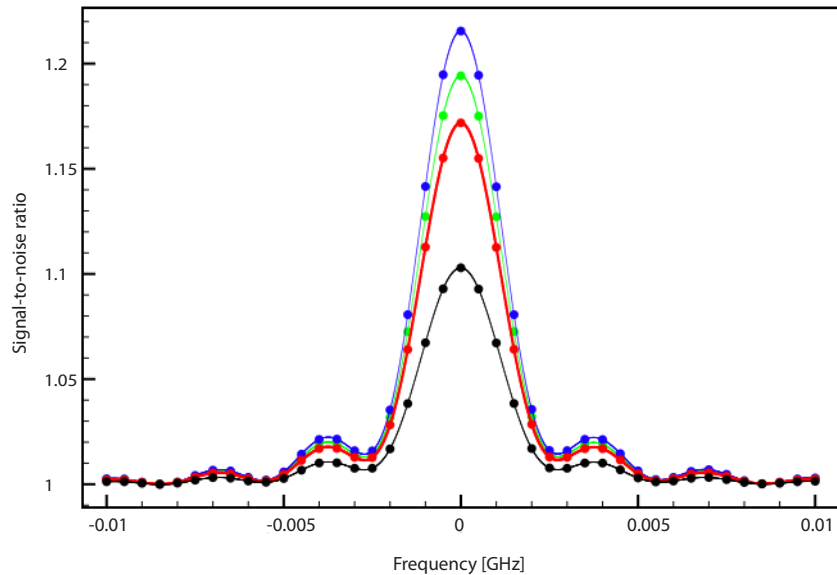


Figure D.1: Signal-to-noise ratio for different temperatures – $T = 2$ K (blue), $T = 6$ K (green), $T = 12$ K (red) and $T = 50$ K (black).

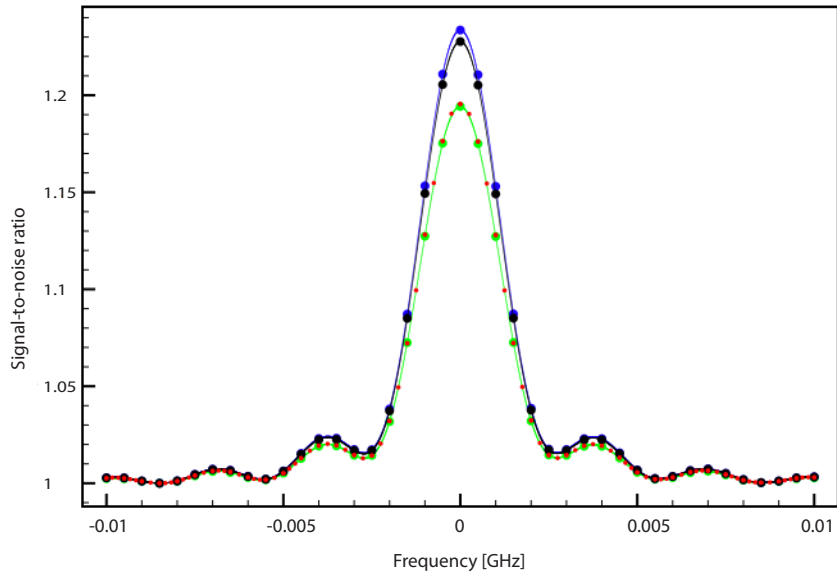


Figure D.2: Signal-to-noise ratio for different Doppler steps – $n = 1$ K (blue, no Doppler broadening considered), $n = 3$ K (black), $n = 5$ K (red) and $n = 10$ K (green).

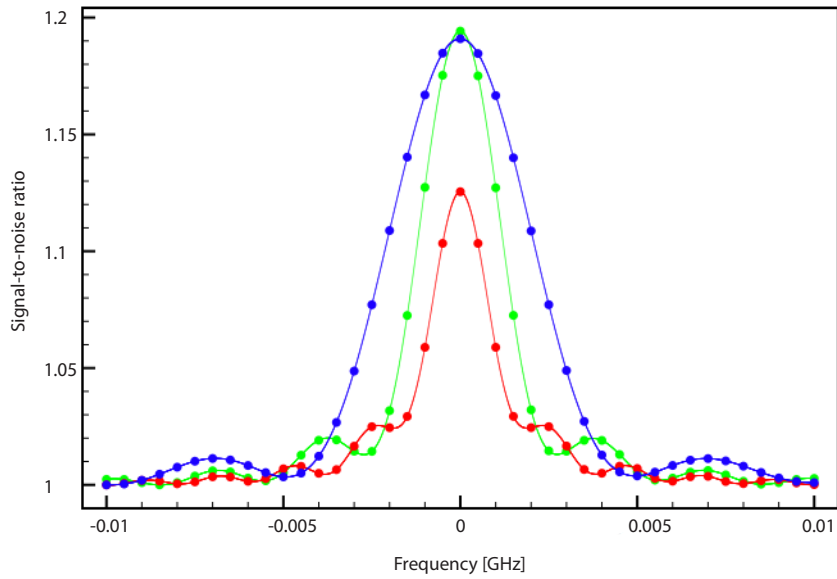


Figure D.3: Signal-to-noise ratio for different microwave times – $t = 200$ ns (blue), $t = 350$ ns (green) and $t = 500$ K (red).

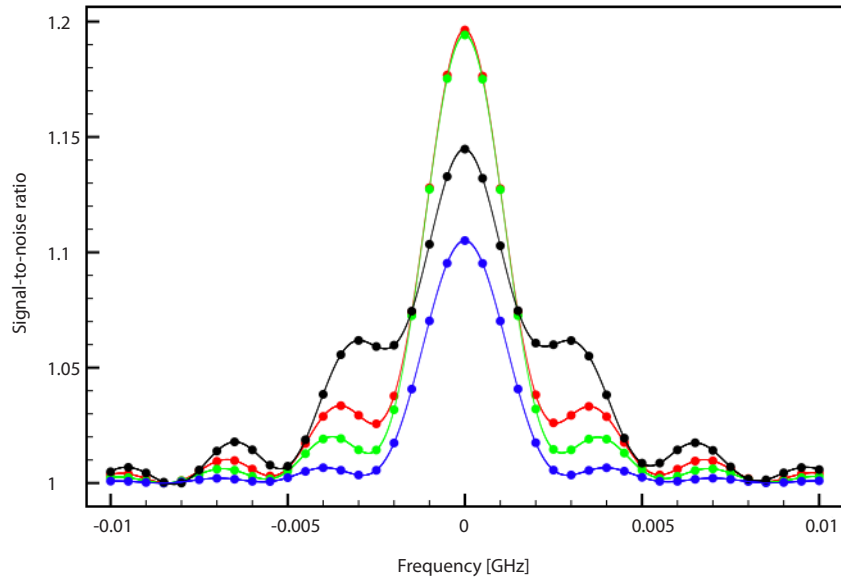


Figure D.4: Signal-to-noise ratio for different microwave power – $P = 2$ W (blue), $P = 6$ W (green), $P = 10$ W (red) and $P = 18$ W (black).

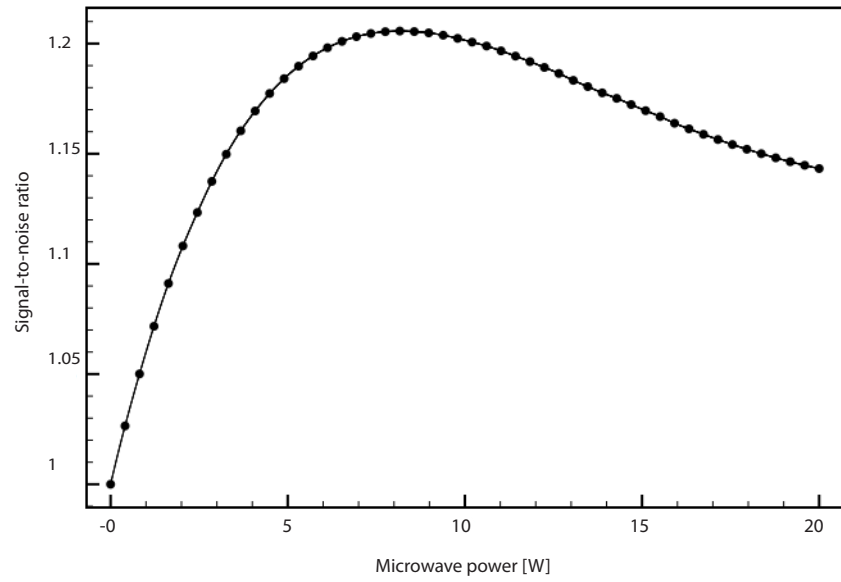


Figure D.5: Signal-to-noise ratio of a microwave power scan for the transition at 11.125 GHz.

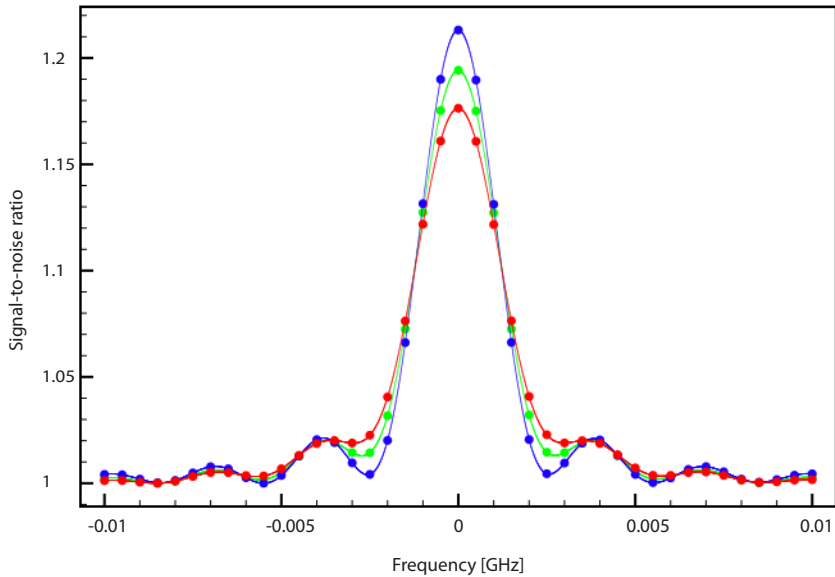


Figure D.6: Signal-to-noise ratio for different elastic collision rates (for microwave)
 $-\gamma_e = 2.5$ MHz (blue), $\gamma_e = 3.5$ MHz (green) and $\gamma_e = 4.5$ MHz (red).

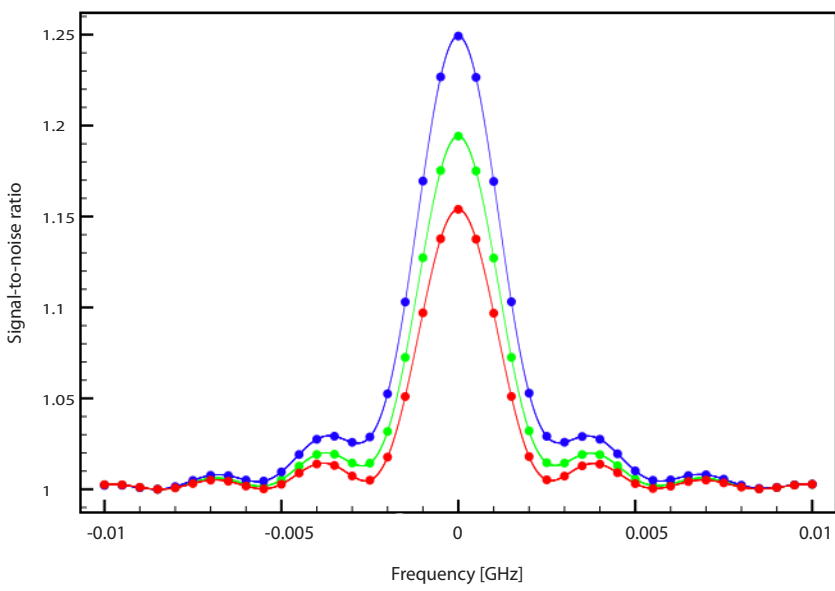


Figure D.7: Signal-to-noise ratio for different inelastic collision rates (for microwave) – $\gamma_i = 1.0$ MHz (blue), $\gamma_i = 1.4$ MHz (green) and $\gamma_i = 1.8$ MHz (red).

Appendix E

Microwave Resonance Profiles

Figure E.1 to E.5 show the two different averaging methods of the microwave transition data for the 11.125 GHz and the 11.157 GHz transition. For the higher resonance the frequency points defined for the measurements in 2011 differed slightly from those used during the beamtime in 2010. Thus these data can only be combined in the averaging over all single scans. The used microwave power for the 11.157 GHz resonance was further lower by about 2.5 W compared to 2011.

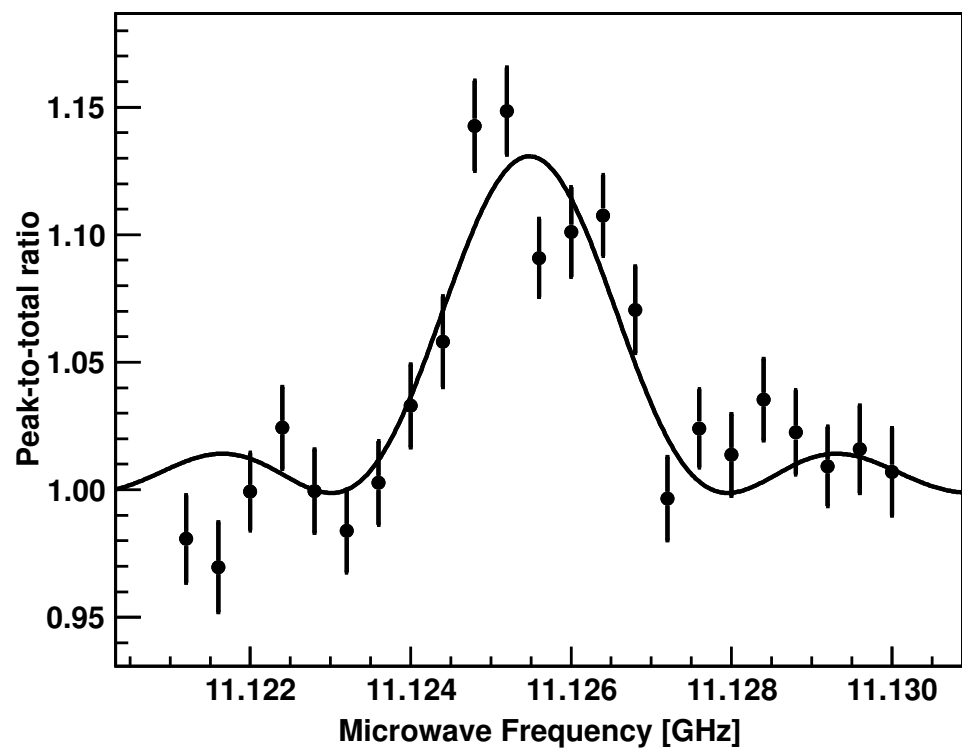


Figure E.1: These plots show the fit of the average of scans (ASF) for the microwave transition at $\nu_{\text{HF}}^{--} = 11.12550$ GHz, including all data recorded in 2010 and 2011.

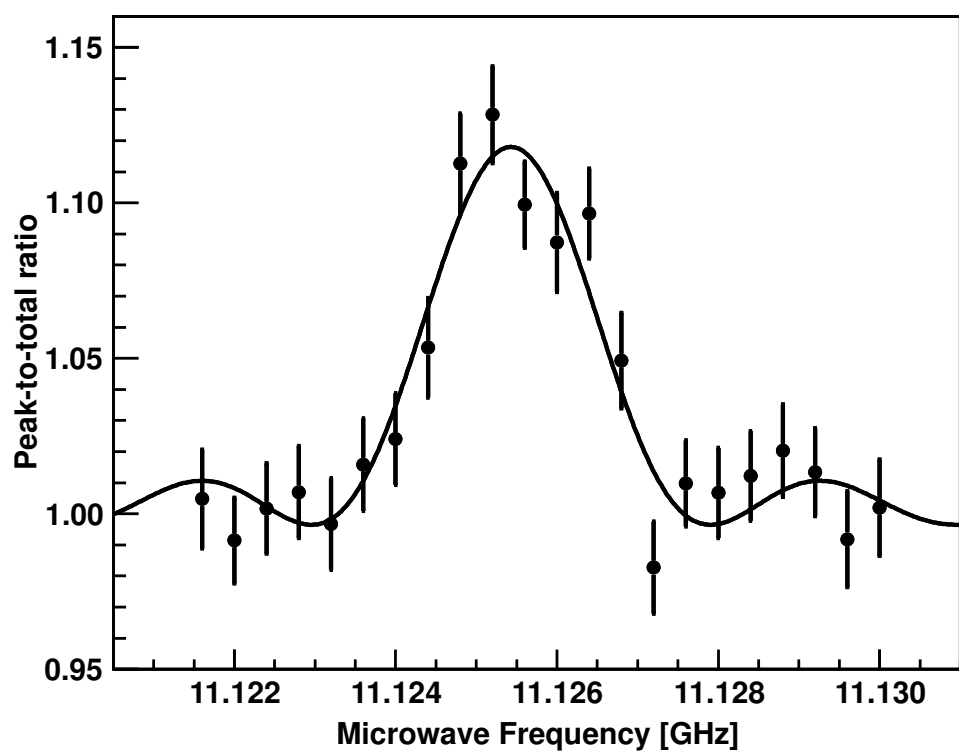


Figure E.2: These plots show the averaging over individually fitted scans (ISF) for the microwave transition at $\nu_{\text{HF}}^{--} = 11.12548$ GHz, including all data recorded in 2010 and 2011.

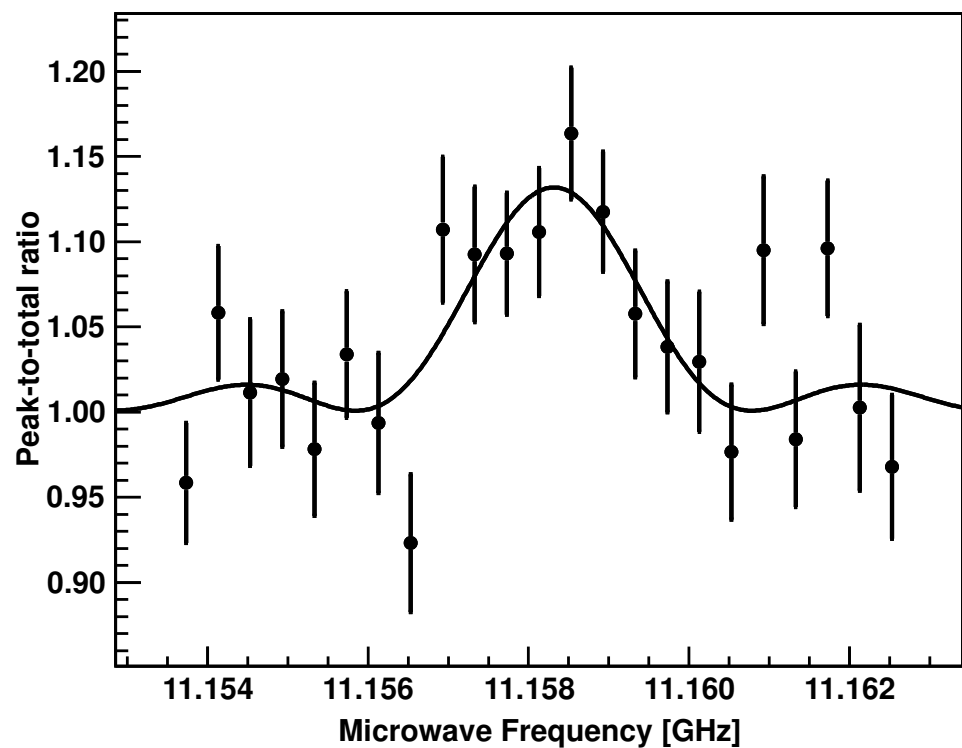


Figure E.3: This plot shows the fit of the average of scans (ASF) for the microwave transition at $\nu_{\text{HF}}^{-+} = 11.15830$ GHz during the measurement period in 2010.

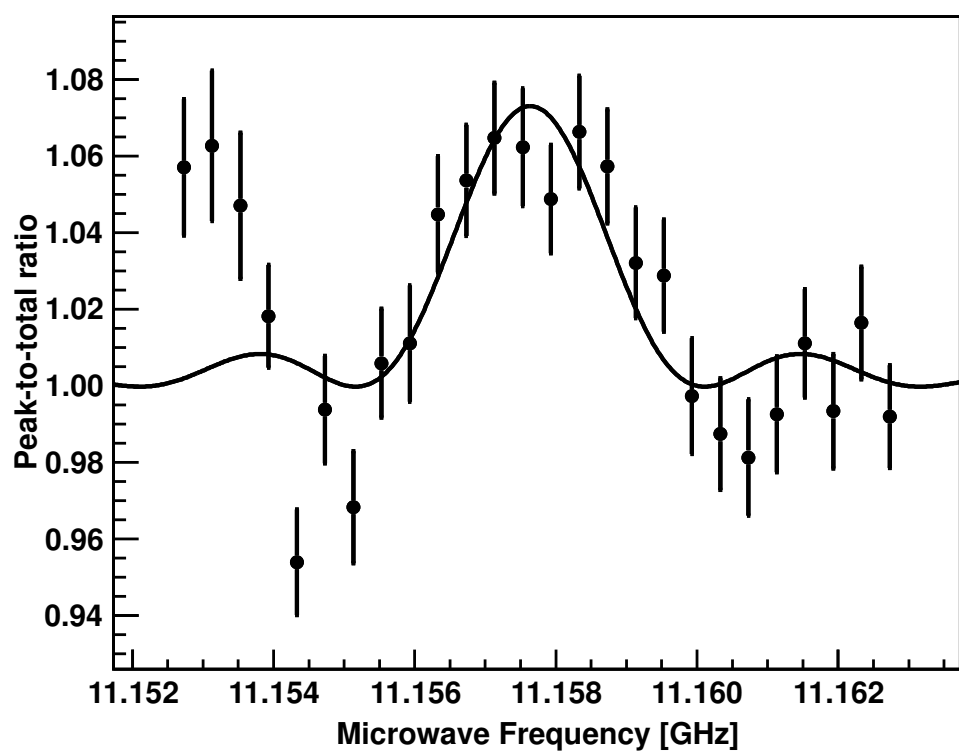


Figure E.4: This plot shows the fit of the average of scans (ASF) for the microwave transition at $\nu_{\text{HF}}^{-+} = 11.15760$ GHz during the measurement period in 2011.

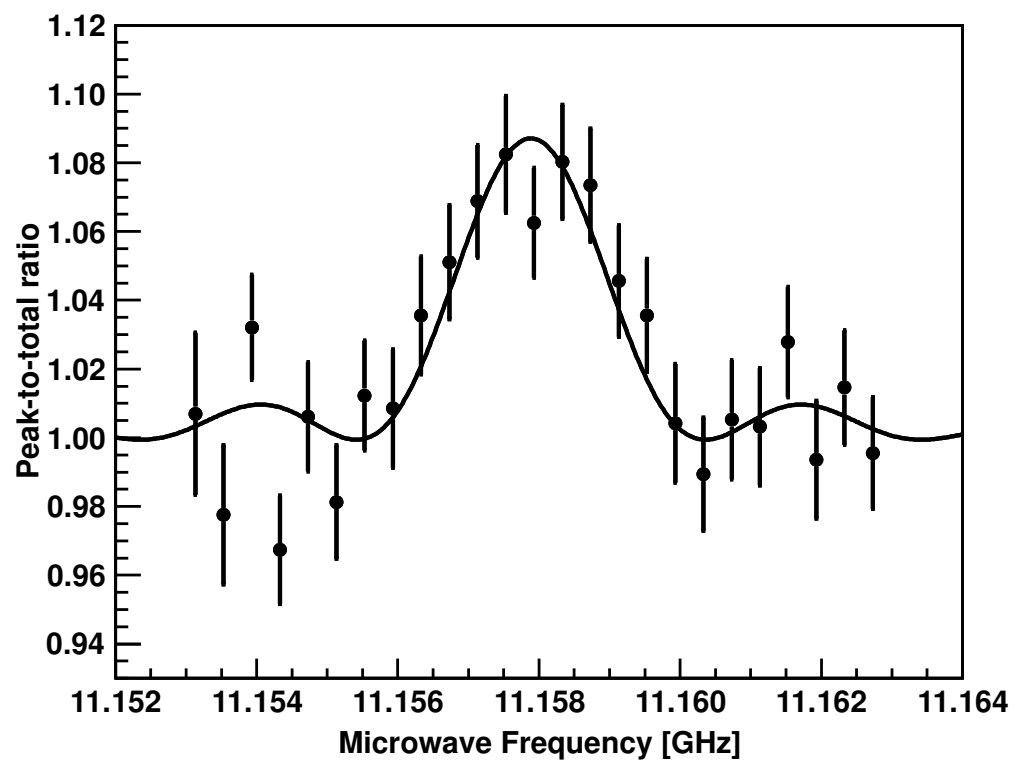


Figure E.5: These plots show the averaging over individually fitted scans (ISF) for the microwave transition at $\nu_{\text{HF}}^{-+} = 11.15793$ GHz, including all data recorded in 2010 and 2011.

Table E.1: The table displays the fit results for the fitting with the reduced χ^2/ndf and with the corrected reduced χ^2/ndf , i.e. after inflating the errors by $\sqrt{\chi^2/ndf}$. The fit transition frequencies are displayed for the two different fitting methods, as explained in Ch. 7 – fit of the averaged scans (ASF) and simultaneous individual fitting (ISF). The results are given for all microwave scans presented above. The data for the 11.157 GHz resonance could only be averaged with the ISF method, due to different microwave powers applied in the beamtimes of 2010 and 2011. Therefore, the values obtained from fitting the single scans before averaging (bold printed values) were used as final results.

Transition	χ^2/ndf		Corrected χ^2/ndf	
	Frequency [GHz]	χ^2/ndf	Frequency [GHz]	χ^2/ndf
ASF				
ν_{HF}^{--}	11.12550(04)	8.71	11.12550(08)	2.03
ISF				
ν_{HF}^{--}	11.12548(03)	7.13	11.12548(08)	0.94
ASF				
ν_{HF}^{-+} (2010)	11.15830(07)	8.26	11.15830(17)	1.27
ν_{HF}^{-+} (2011)	11.15760(07)	8.42	11.15760(14)	2.50
ISF				
ν_{HF}^{-+}	11.15793(04)	7.92	11.15793(13)	1.00

List of Figures

2.1	Antiprotonic Helium	7
2.2	Energy Level Diagram of Antiprotonic Helium	9
2.3	Hyperfine Splitting of $\bar{p}^4\text{He}^+$	12
2.4	Hyperfine Splitting of $\bar{p}^3\text{He}^+$	12
3.1	First Laser Annihilation Signal	16
3.2	Experimental Technique	18
3.3	ADATS Spectrum	19
3.4	Theoretical Relaxation Rates	22
3.5	Laser Depletion Measurement (AA)	23
3.6	Laser Depletion Measurement (OA)	23
4.1	AD Cooling Cycle	26
4.2	Experimental Setup Drawing	28
4.3	Overview of the Setup	30
4.4	Drawing of the Gas System	32
4.5	Setup for the Laser System	32
4.6	Timing and Trigger System	35
5.1	Microwave Target	41
5.2	HFSS Simulation of the Setup	42
5.3	HFSS Simulation of the Magnetic Field Distribution	42
5.4	View on HFSS Graphical Surface	43
5.5	S11 and S21 signal for the 11 GHz Resonance	44
5.6	The Microwave Cavities	48
5.7	Reflections on Resonance Signal for the 16 GHz Target 1 . . .	49
5.8	Reflections on Resonance Signal for the 16 GHz Target 2 . . .	50
5.9	Stainless Steel Meshes	51

5.10 S11 and S21 signal for the 11 GHz Cavity	53
5.11 Mode Chart	54
5.12 Field Distribution of TM ₁₁₀ mode in Cylindrical Cavity	55
5.13 Antenna Coupling Modes	57
5.14 Setup for Perturbation Measurements	59
5.15 Perturbation Measurement Results for the New 11 GHz Cavity	60
5.16 Perturbation Measurement Results for the Old 11 GHz Cavity	61
5.17 Microwave Frequency Spectrum over	62
5.18 Operating Modes – Old MW Setup	64
5.19 Testin Mode – New MW Setup	69
5.20 Operating Mode – New MW Setup	69
5.21 Diode Calibration	71
5.22 TWTA Calibration	72
6.1 Electric Dipole Moment	78
6.2 Rabi Oscillations for the Laser Transitions	79
6.3 Gaussian Resonance Profile at Different Temperatures	81
6.4 Refilling from upper state	81
6.5 Magnetic Dipole Moment	83
6.6 Rabi Oscillations for the Microwave Transitions	87
6.7 Rabi Oscillations for the Microwave – Elastic Collision Rate .	88
6.8 Rabi Oscillations for the Microwave – Inelastic Collision Rate	88
6.9 Rabi Oscillations for the Microwave – Laser Delay	89
6.10 Rabi Oscillations for the Microwave – Microwave Power	89
6.11 Microwave Transitions Signal Simulation	90
7.1 Online Analysis	95
8.1 Beam Ranging	102
8.2 Laser Resonance Profile in ⁴ He	104
8.3 Laser Resonance Profile in ³ He	105
8.4 Relaxation Process	106
8.5 Relaxation Process	107
8.6 Microwave Power Scan	109
8.7 Microwave Power Fluctuation @ 11.125 GHz	110
8.8 Microwave Power Fluctuation @ 11.157 GHz	110
8.9 Microwave Resonance Scan @ 11.125 GHz	114

8.10	Microwave Resonance Scan @ 11.157 GHz	115
8.11	Summary of Principal Results	116
A.1	Smith Chart	124
A.2	Triple-Stub-Tuner Setup	127
B.1	Stainless Steel Gratings	129
C.1	Reflection and Transmission for 11 GHz	132
C.2	Reflection and Transmission for 11 GHz – Smith Chart	132
C.3	Reflection and Transmission for 16 GHz	133
C.4	Reflection and Transmission for 16 GHz – Smith Chart	133
C.5	Reflection as Function of Conductivity for 11 GHz	134
C.6	Transmission as Function of Conductivity for 11 GHz	134
C.7	Reflection as Function of Iris Size for 11 GHz	135
C.8	Transmission as Function of Iris Size for 11 GHz	135
C.9	Reflection as Function of Cavity Radius for 11 GHz	136
C.10	Transmission as Function of Cavity Radius for 11 GHz	136
D.1	Rabi Oscillations for the Microwave Transitions – Simulation	139
D.2	Rabi Oscillations for the Microwave Transitions – Simulation	140
D.3	Rabi Oscillations for the Microwave Transitions – Simulation	140
D.4	Rabi Oscillations for the Microwave Transitions – Simulation	141
D.5	Rabi Oscillations for the Microwave Transitions – Simulation	141
D.6	Rabi Oscillations for the Microwave Transitions – Simulation	142
D.7	Rabi Oscillations for the Microwave Transitions – Simulation	142
E.1	ASF at 11.125 GHz	144
E.2	ISF at 11.125 GHz	145
E.3	AFS at 11.157 GHz	146
E.4	AFS at 11.157 GHz	147
E.5	IFS at 11.157 GHz	148

List of Tables

5.1	Electrical Conductivity	46
5.2	Cavity Dimensions	47
5.3	Field Mode Calculation	56
6.1	Doppler Broadening	80
8.1	Summary of Experimental Results	113
C.1	Eigenmode Solution Results for Conductivity Dependence . .	137
E.1	Fit Data for Simple and Corrected χ^2/ndf	149

Bibliography

- [1] P.A.M. Dirac, *Proc. R. Soc. Lond. A* **117** 620-624 (1928).
- [2] C.D. Anderson, *Science* **76** 238 (1932).
- [3] O. Chamberlain, E. Segr, C. Wiegand, T. Ypsilantis, *Phys. Rev.* **100** 947 (1955).
- [4] B. Cork, G.R. Lambertson, O. Piccioni, W.A. Wenzel, *Phys. Rev.* **104** 1193 (1956).
- [5] C.S. Wu, E. Ambler, R.W. Hayward, D.D. Hoppes, R.P. Hudson, *Phys. Rev.* **105** 1413 (1957).
- [6] J.H. Christenson, J.W. Cronin, V.L. Fitch, R. Turlay, *Phys. Rev. Lett.* **13** 138 (1967).
- [7] T. Pask, D. Barna, A. Dax, R.S. Hayano, M. Hori, D. Horváth, S. Friedreich, B. Juhász, O. Massiczek, N. Ono, A. Sótér, E. Widmann, *Phys. Lett. B* **678** 55-59 (2009).
- [8] S. Friedreich, D. Barna, A. Dax, R.S. Hayano, D. Horváth, M. Hori, B. Juhász, O. Massiczek, A. Sótér, T. Pask, E. Widmann, *Hyperfine Interactions* **199(1–3)** 337–346 (2011).
- [9] S. Friedreich, D. Barna, F. Caspers, A. Dax, R.S. Hayano, M. Hori, D. Horváth, B. Juhász, T. Kobayashi, O. Massiczek, A. Sótér, K. Todoroki, E. Widmann, J. Zmeskal, *Phys. Lett. B* **700(1)** 1 (2011).
- [10] O. Massiczek, S. Friedreich, B. Juhász, E. Widmann, J. Zmeskal, *Nucl. Inst. Meth. A* **659** 55 (2011).
- [11] E. Fermi, E. Teller, *Phys. Rev.* **77** 399 (1947).

- [12] A.S Wightman, *Phys. Rev.* **77** 521 (1950).
- [13] J.G. Fetkovich, E.G. Pewitt, *Phys. Rev. Lett.* **11** 290 (1963).
- [14] M.M. Block, T. Kikuchi, D. Koetke, J. Kopelman, C.R. Sun, R. Walker, G. Culligan, V.L. Telegdi, R. Winston, *Phys. Rev. Lett.* **11** 301 (1963).
- [15] M.M. Block, J. Kopelman, C.R. Sun, *Phys. Rev. B* **140** 143 (1965).
- [16] J.G. Fetkovich, J. McKenzie, B.R. Riley, I.-T. Wang, *Phys. Rev. D* **2** 1803 (1970).
- [17] T.B. Day, G.A. Snow, J. Sucher, *Phys. Rev. Lett.* **3** 61 (1959).
- [18] M. Leon, H.A Bethe, *Phys. Rev.* **127** 636 (1962).
- [19] T.H. Fields, G.B. Yodh, M. Derrick, J.G. Fetovich, *Phys. Rev. Lett.* **5** 69 (1960).
- [20] J.H. Doede, R.H. Hildebrand, M.H Israel, M.R. Pyka, *Phys. Rev.* **129** 2808 (1963).
- [21] G.T. Condo, *Phys. Lett.* **9** 65 (1964).
- [22] J.E. Russell, *Phys. Rev. Lett.* **23** 63 (1969); *Phys. Rev.* **188** 187 (1969); *Phys. Rev. A* **1** 721 (1970); *Phys. Rev. A* **1** 735 (1970); *Phys. Rev. A* **1** 742 (1970); *J. Math. Phys.* **12** 1906 (1971); *Phys. Rev. A* **6** 2488 (1972).
- [23] T. Yamazaki, M. Aoki, M. Iwasaki, R.S. Hayano, T. Ishikawa, H. Outa, E. Takada, H. Tamura, A. Sakaguchi, *Phys. Rev. Lett.* **63** 1483 (1989).
- [24] M. Iwasaki, S.N. Nakamura, K. Shigaki, Y. Shimizu, H. Tamura, T. Ishikawa, R.S. Hayano, E. Takada, E. Widmann, H. Outa, M. Aoki, P. Kitching, T. Yamazaki, *Phys. Rev. Lett.* **67** 1246 (1991).
- [25] S.N. Nakamura, M. Iwasaki, H. Outa, R.S. Hayano, Y. Watanabe, T. Nagae, T. Yamazaki, H. Tada, T. Numao, Y. Kuno, R. Kadono, *Phys. Rev. A* **45** 6202 (1992).
- [26] T. Pask, *PhD Thesis*, University of Vienna (2009) - unpublished.
- [27] T. Yamazaki, E. Widmann, R.S. Hayano, M. Iwasaki, S.N. Nakamura, K. Shigaki, F.J. Hartmann, H. Daniel, T. von Egidy, P. Hofmann, Y.-S. Kim, J. Eades, *Nature* **361** 238 (1993).

- [28] T. Yamazaki, N. Morita, R.S. Hayano, E. Widmann, J. Eades, *Phys. Rep.* **366** 183 (2002).
- [29] R.S. Hayano, M. Hori, D. Horváth, E. Widmann, *Rep. Prog. Phys.* **70** 1 (2007).
- [30] T. Yamazaki, E. Widmann, R.S. Hayano, M. Iwasaki, S.N. Nakamura, K. Shigaki, F.J. Hartmann, H. Daniel, T. von Egidy, P. Hofmann, Y.-S. Kim, J. Eades, *Nature* **361** 238 (1993).
- [31] N. Morita, M. Kumakura, T. Yamazaki, E. Widmann, H. Masuda, I. Sugai, R.S. Hayano, F.E. Maas, H.A. Torii, F.J. Hartmann, H. Daniel, T. von Egidy, B. Ketzer, W. Müller, W. Schmid, D. Horváth, J. Eades, *Rhys. Rev. Lett.* **72** 1180 (1994).
- [32] H.A. Torii, R.S. Hayano, M. Hori, T. Ishikawa, N. Morita, M. Kumakura, I. Sugai, T. Yamazaki, B. Ketzer, F.J. Hartmann, T. von Egidy, R. Pohl, C. Maierl, D. Horváth, J. Eades, E. Widmann, *Phys. Rev. A* **59** 223 (1999).
- [33] M. Hori, J. Eades, R.S. Hayano, T. Ishikawa, J. Sakaguchi, E. Widmann, H. Yamaguchi, H.A. Torii, B. Juhász, D. Horváth, T. Yamazaki, *Phys. Rev. Lett.* **87** 093401 (2001).
- [34] M. Hori, A. Dax, J. Eades, K. Gomikawa, R.S. Hayano, N. Ono, W. Pirkl, E. Widmann, H.A. Torii, B. Juhász, D. Barna, D. Horváth, M. Hori *Phys. Rev. Lett.* **96** 243401 (2006).
- [35] M. Hori, A. Sótér, D. Barna, A. Dax, R. Hayano, S. Friedreich, B. Juhász, T. Pask, E. Widmann, D. Horváth, L. Venturelli, N. Zurlo, *Nature* **475** 484 (2011).
- [36] V.I. Korobov, D. Bakalov, *J. Phys. B* **34** 519 (2001).
- [37] V. Korobov, *Phys. Rev. A* **73** 022509 (2006).
- [38] V. Korobov, Z.-X. Zhong, *Phys. Rev. A* **80**, 042506 (2009).
- [39] T. Kinoshita, M. Nio, *Phys. Rev. D* **53** 4909 (1996).
- [40] D. Bakalov, V.I. Korobov, *Phys. Rev. A* **57** 1662 (1998).
- [41] Y. Kino et al., *Hyperfine Interactions* **146** 331 (2003).

- [42] E. Widmann, J. Eades, T. Ishikawa, J. Sakaguchi, T. Tasaki, H. Yamaguchi, R.S. Hayano, M. Hori, H.A. Torii, B. Juhász, D. Horváth, T. Yamazaki, *Phys. Rev. Lett.* **89** 243402 (2002).
- [43] M. Hori, J. Eades, R.S. Hayano, T. Ishikawa, W. Pirkl, E. Widmann, H. Yamaguchi, H.A. Torii, B. Juhász, D. Horváth, T. Yamazaki, *Phys. Rev. Lett.* **91** 123401 (2003).
- [44] G.Y. Korenman, *personal communication* (2010).
- [45] M. Hori, J. Eades, R.S. Hayano, T. Ishikawa, J. Sakaguchi, T. Tasaki, E. Widmann, H. Yamaguchi, H.A. Torii, B. Juhász, D. Horváth, T. Yamazaki, *Phys. Rev. Lett.* **89** 093401 (2002).
- [46] S. Baird et al., *Nucl. Phys. B (Proc. Suppl.)* **56(A)** 349 (1997).
- [47] G.Ya. Korenman, S.N. Yudin, *private communication* (2011).
- [48] G.Ya. Korenman, S.N. Yudin, *Hyperfine Interactions* **194(1–3)** 29 (2009).
- [49] S. Maury (on behalf of the AD team), *LEAR Symposium CERN* (1999).
- [50] C. Carli, F. Caspers, <http://cdsweb.cern.ch> (2000).
- [51] M. Hori, *Rev. Sci. Inst.* **76** 113303 (2005).
- [52] ANSYS, <http://www.ansys.com> (2010).
- [53] J. Sakaguchi, *PhD Thesis*, University of Tokyo, Japan (2002) - unpublished.
- [54] J. Sakaguchi, H. Gilg, R.S. Hayano, T. Ishikawa, K. Suyuki, E. Widmann, H. Yamaguchi, F. Caspers, J. Eades, M. Hori, D. Barna, D. Horváth, B. Juhsz, H.A. Torii, T. Yamazaki, *Nucl. Inst. Meth. A* **533** 598 (2004).
- [55] J. Byrd, *Microwave Measurements Laboratory*, USPAS and CCAST Beijing, China (1998).
- [56] R.E. Collin, *Foundations for Microwave Engineering*, McGraw-Hill International Editions, Singapore (1992).
- [57] Ansoft, <http://www.ansoft.com/products/hf/hfss> (2010).

- [58] M. Fouaidy, N. Hammoudi, *Physica C* **441** 137 (2006).
- [59] T.S. Saad, R.C. Hansen, G.J. Wheeler, *Microwave Engineer's Handbook Volume 1*, Artech House, Inc., Massachusetts (1971).
- [60] R. Brun, F. Rademakers, *Nucl. Inst. Meth. A* **389** 81, <http://root.cern.ch> (1997).
- [61] M. Hori, J. Eades, E. Widmann, T. Yamazaki, R.S. Hayano, T. Ishikawa, H.A. Torii, T. von Egidy, F.J. Hartmann, B. Ketzer, C. Maierl, R. Pohl, M. Kumakura, N. Morita, D. Horváth, I. Sugai, *Phys. Rev. A* **70** 012504 (2004).
- [62] G.Ya. Korenman, S.N. Yudin, *J. Phys. B* **39** 1473 (2006).
- [63] W. Demtroeder, *Experimentalphysik Band 3: Atome, Moleküle und Festkörper*, Springer-Verlag, (2010).
- [64] T. Yamazaki, N. Morita, R.S. Hayano, E. Widmann, J. Eades, *Phys. Rep.* **366** 183 (2002).
- [65] R.H. Dicke, *Phys. Rev.* **89(2)** 472 (1953).
- [66] B. Lance, D. Robert, *J. Chem. Phys.* **109(19)** 8283 (1998).
- [67] H. Yamaguchi, *PhD Thesis*, University of Tokyo, Japan (2003) - unpublished.
- [68] C. Malbrunot, *Diploma Thesis*, SMI Vienna, Austria (2007) - unpublished.
- [69] S. Flugge (ed.), *Encyclopedia of Physics*, Springer-Verlag, Berlin - Göttingen - Heidelberg (1959).
- [70] V.I. Korobov, *private communication* (2010).
- [71] M. Hori, *private communication* (2011).
- [72] D. Barna, *private communication* (2011).
- [73] T. Pask et al., *J. Phys. B At. Mol. Opt. Phys.* **41** 081008 (2008).

Curriculum Vitae

Name: Susanne Friedreich, Mag.rer.nat.
Date of Birth 2nd March 1982
Address: Gumpendorferstrasse 83-85/2/46
Vienna
1060
Austria
E-mail: susanne.friedreich@oeaw.ac.at
suzanne.friedreich@cern.ch
Nationality: Austrian

Education	
10/2008-today	Doctoral Thesis, Physics <i>Hyperfine Structure Measurements of Antiprotonic ^3He Using Microwave Spectroscopy</i> University of Vienna, Vienna, Austria
31/01/2008	Diploma Thesis, Physics <i>Investigation of Statistical Characteristics of BOLD fMRI Data and their Consequences on Data Analysis</i> University of Vienna, Vienna, Austria
10/2003-06/2004	Study of Physics University of Milan, Milan, Italy Participation in the ERASMUS Exchange Program
10/2000-01/2008	Study of Physics University of Vienna, Vienna, Austria
10/2001-04/2008	Study of Philosophy University of Vienna, Vienna, Austria
09/1992-06/2000	Bundesgymnasium Stockerau (Linguistic Gymnasium) Stockerau, Lower Austria, Austria

Scientific Employment	
10/2008-today	Scientific Assistant/PhD Student Stefan Meyer Institute for Subatomic Physics Austrian Academy of Sciences, Vienna, Austria
07-07/2008	Project Student <i>Measurement of the Hyperfine Structure of Antiprotonic 4He</i> CERN, Geneva, Switzerland
01-12/2006	Scientific Employee <i>Measurements for Psychiatric Studies Using fMRI at 3 Tesla</i> Center for Biomedical Technique and Physics Medical University of Vienna, Vienna, Austria
10-12/2005	Project Student <i>Correction of Physiological Artifacts in fMRI Measurements</i> Center for Biomedical Technique and Physics Medical University of Vienna, Vienna, Austria
07-09/2005	Internship <i>Imaging Systems</i> Group (PET/CT development) Philips Research Laboratories Aachen, Germany
08/2001-06/2003	Coaching in Mathematics and Physics Institute Dr. Rampitsch Vienna, Austria
Stays Abroad	
10/2003-06/2004	ERASMUS Study, Milan, Italy
07-09/2005	Internship, Aachen, Germany
03/2008-06/2008	Volunteer Work, Karnataka, India
07-07/2008	Project Student, CERN, Switzerland
Summer/2009	Experiment/PhD project, CERN, Switzerland
Summer/2010	Experiment/PhD project, CERN, Switzerland
Summer/2011	Experiment/PhD project, CERN, Switzerland

Conferences

12/2011	ASACUSA Collaboration Meeting <i>Spectroscopy with Antiprotons in ${}^3\text{He}$ – The Final Results</i> Matsue, Japan
09/2011	International Conference on Exotic Atoms and Related Topics (EXA11) <i>Microwave Spectroscopy of the Hyperfine Structure with Antiprotonic ${}^4\text{He}$ and ${}^3\text{He}$</i> Vienna, Austria
04/2011	10th International Conference on Low Energy Antiproton Physics (LEAP 2011) <i>Hyperfine Structure Spectroscopy with Antiprotons in Helium</i> TRIUMF, Vancouver, Canada
12/2010	ASACUSA Collaboration Meeting <i>Spectroscopy with Antiprotons in ${}^3\text{He}$ – The First Successful Measurements</i> Geneva, Switzerland
09/2010	Tagung des Fachausschusses für Kern- und Teilchenphysik der Österreichischen Physikalischen Gesellschaft (FAKT – ÖPG) <i>Spectroscopy with Antiprotons in ${}^3\text{He}$</i> Salzburg, Austria
04/2010	5th Conference on Trapped Charged Particles and Fundamental Physics (TCP 2010) <i>Spectroscopy with Antiprotons in ${}^4\text{He}$ and ${}^3\text{He}$</i> Saariselkä, Finland
12/2009	ASACUSA Collaboration Meeting <i>Spectroscopy with Antiprotons in ${}^3\text{He}$ – The First Experiment Run</i> Geneva, Switzerland
09/2009	Tagung des FAKT – ÖPG <i>Spectroscopy with Antiprotons in ${}^3\text{He}$ – Preparations of the Experiment</i> Innsbruck, Austria
06/2009	Precision Experiments at Lowest Energies for Fundamental Tests and Constants (Seminar der Heraeus Stiftung) <i>Preparations for HFS Spectroscopy of Antiprotonic ${}^3\text{He}$</i> Bad Honnef, Germany

12/2008	ASACUSA Collaboration Meeting Tokio, Japan
06/2007	13th Meeting of the Organization for Human Brain Mapping <i>Investigation of the Fulfillment of Statistical Assumptions made on fMRI BOLD Data</i> Chicago, United States

Languages

German (mother tongue), English (fluent), Italian (fluent),
French (moderate), Spanish (basic)

Publications and Conference Contributions

S. Friedreich, D. Barna, F. Caspers, A. Dax, R. S. Hayano, M. Hori, D. Horváth, B. Juhász, T. Kobayashi, O. Massiczek, A. Sótér, K. Todoroki, E. Widmann, J. Zmeskal. Improved Measurements of the Hyperfine Structure of Antiprotonic ${}^3\text{He}$ Using Microwave Spectroscopy. Submission to *Physics Letters B* in progress (2012).

S. Friedreich, D. Barna, F. Caspers, A. Dax, R. S. Hayano, M. Hori, D. Horváth, B. Juhász, T. Kobayashi, O. Massiczek, A. Sótér, K. Todoroki, E. Widmann, J. Zmeskal. Microwave spectroscopy measurements of the hyperfine structure in antiprotonic ${}^3\text{He}$. Revision submitted to *Hyperfine Interactions* (2012).

M. Hori, A. Sótér, D. Barna, A. Dax, R. Hayano, **S. Friedreich**, B. Juhász, T. Pask, E. Widmann, D. Horváth, L. Venturelli, N. Zurlo. Two-photon laser spectroscopy of antiprotonic helium and the antiproton-to-electron mass ratio. *Nature* **475**, 484-488 (2011).

O. Massiczek, **S. Friedreich**, B. Juhász, E. Widmann, J. Zmeskal. Liquid helium-free cryostat and hermetically sealed cryogenic microwave cavity for hyperfine spectroscopy of antiprotonic helium. *Nucl. Instr. Meth. A* **659**, 55-60 (2011).

S. Friedreich, D. Barna, F. Caspers, A. Dax, R. S. Hayano, M. Hori, D. Horváth, B. Juhász, T. Kobayashi, O. Massiczek, A. Sótér, K. Todoroki, E. Widmann, J. Zmeskal. First observation of two hyperfine transitions in ${}^3\text{He}$. *Physics Letters B* **700**(1), 1-6 (2011).

S. Friedreich, D. Barna, A. Dax, R. S. Hayano, M. Hori, D. Horváth, B. Juhász, O. Massiczek, A. Sótér, T. Pask, E. Widmann. Spectroscopy of the hyperfine structure of antiprotonic ${}^4\text{He}$ and ${}^3\text{He}$. *Hyperfine Interactions* **199**(1-3), 337-346 (2010).

T. Pask, D. Barna, A. Dax, R. S. Hayano, M. Hori, D. Horváth, **S. Friedreich**, B. Juhász, O. Massiczek, N. Ono, A. Sótér, E. Widmann. Antiproton magnetic moment determined from the HFS of antiprotonic helium. *Physics Letters B* **678**(1), 55-59 (2009).

R. Lanzenberger, C. Windischberger, M. Mitterhauser, C. Spindelegger, W. Wadsak, U. Moser, P. Stein, **S. Friedreich** et al. Inverse relationship between neural activation and serotonin 1A receptor expression revealed by multimodal neuroimaging with fMRI and PET. *13th Meeting of the Organization for Human Brain Mapping (HBM)*, Chicago (2007).

S. Friedreich, C. Windischberger, R. Lanzenberger, C. Spindelegger, U. Moser, P. Stein, A. Holik, E. Moser. Investigation of the fulfillment of statistical assumptions made on fMRI BOLD data. *13th Meeting of the Organization for Human Brain Mapping (HBM)*, Chicago (2007).

C. Windischberger, R. Lanzenberger, **S. Friedreich**, C. Spindelegger, A. Holik, P. Stein, U. Moser, E. Moser, S. Kasper. Escitalopram changes amygdala activation during emotional processing as revealed by pharmacological fMRI at 3T. *2nd International Congress on Biological Psychiatry*, Santiago de Chile (2007).

A. Holik, R. Lanzenberger, C. Windischberger, C. Spindelegger, **S. Friedreich**, P. Stein, U. Moser, S. Kasper. Cortisol modulates task performance in emotion discrimination during fMRI scanning. *2nd International Congress on Biological Psychiatry*, Santiago de Chile (2007).

C. Windischberger, R. Lanzenberger, **S. Friedreich**, C. Spindelegger, A. Holik, P. Stein, U. Moser, E. Moser, S. Kasper. Administration of selective serotonin reuptake inhibitors changes amygdala activation during facial emotion processing. *15th Meeting of the International Society for Magnetic Resonance in Medicine (ISMRM)*, Berlin (2007).

C. Windischberger, **S. Friedreich**, B. Hoheisel, E. Moser. The impact of physiological artifact correction on individual and group results in fMRI of the amygdala. *12th Meeting of the Organization for Human Brain Mapping (HBM)*, Florence (2006).

**”One must have a chaos inside oneself
to give birth to a dancing star..” – Friedrich Nietzsche**